UNIVERSITE DE NEUCHATEL
INSTITUT DE MICROTECHNIQUE

GROWTH, MICROSTRUCTURE AND ELECTRICAL PERFORMANCES OF THIN FILM MICROCRYSTALLINE SILICON SOLAR CELLS

THESE

Présentée à la Faculté des Sciences
pour obtenir le grade de docteur ès sciences
par

Julien Bailat

IMPRIMATUR POUR LA THESE

Growth, microstructure and electrical performances of thin film microcrystalline silicon solar cells

M. Julien BAILAT

UNIVERSITE DE NEUCHATEL

FACULTE DES SCIENCES

La Faculté des sciences de l'Université de Neuchâtel, sur le rapport des membres du jury

Mme E. Vallat, MM. A. Shah (directeur de thèse), H. Beck, R.W. Collins (University Park USA), M. Vanecek (Prague CZ), J. Meier (Unaxis, Neuchâtel) et A. Vallat (Oscilloquartz, Neuchâtel)

autorise l'impression de la présente thèse.

Neuchâtel, le 1er juillet 2004

La doyenne:

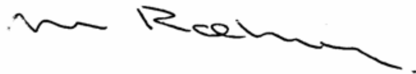

Martine Rahier

TABLE OF SYMBOLS

µc-Si:H	hydrogenated microcrystalline silicon
a-Si:H	hydrogenated amorphous silicon
c-Si	monocrystalline silicon
LPCVD	low pressure chemical vapor deposition
PECVD	plasma-enhanced chemical vapor deposition
MBE	molecular beam epitaxy
VHF	very-high frequency
SiH_4	silane
H_2	hydrogen
SC	silane concentration, i.e. the silane flow over the total gas flow: $SC=[SiH_4]/[SiH_4+H_2]$
ZnO	zinc oxide
TCO	transparent conductive oxide
CPM	constant photocurrent method
PDS	photothermal deflection spectroscopy
FTIR	Fourier transform infra-red spectroscopy
FTPS	Fourier transform photocurrent spectroscopy
XRD	X-ray diffractometer
TEM	transmission electron microscopy
AFM	atomic force microscopy
SEM	scanning electron microscopy
RTSE	real time spectroscopic ellipsometry
I_{sc}	short-circuit current density
V_{oc}	open-circuit voltage
FF	fill-factor
n_d	nuclei density
h	heterophase layer thickness
rms	root-mean square
E_0	Urbach parameter
$\phi_{c\ 514,\ 633nm}$	crystalline fraction evaluated with Raman spectroscopy at 514 or 633nm wavelength
$\phi_{c\ TEM}$	crystalline fraction evaluated with TEM
t	crystalline threshold
n	number of crystallographic orientations
d	etching probability

TABLE OF CONTENTS

1. INTRODUCTION 1

2. DEPOSITION AND CHARACTERIZATION TECHNIQUES 5

2.1. INTRODUCTION 5
2.2. SOLAR CELL STRUCTURE 5
2.3. TRANSPARENT CONDUCTIVE OXIDE (TCO) 5
2.4. SILICON DEPOSITION 5
2.5. CHARACTERIZATION TECHNIQUES 6
2.5.1. Illuminated I(V) measurement 6
2.5.2. External quantum efficiency 6
2.5.3. Measurement of the sub-gap absorption coefficient 7
2.5.4. Microstructure characterization 8
2.5.5. Micro-Raman spectroscopy 9
2.5.6. X-ray diffraction 10

3. DESCRIPTION OF THE MICROSTRUCTURE OF μC-SI:H 11

3.1. INTRODUCTION 11
3.2. EXPERIMENTAL 11
3.3. RESULTS 11
3.4. DISCUSSION 16
3.4.1. Definitions 16
3.4.2. Conical shape of conglomerates 16
3.4.3. Nucleation and thickness transition 17
3.5. CONCLUSIONS 17

4. GROWTH OF μC-SI:H LAYERS: INFLUENCE OF SUBSTRATE SURFACE CHEMISTRY AND TOPOGRAPHY 19

4.1. INTRODUCTION 19
4.2. EXPERIMENTAL 19
4.3. RESULTS 20
4.3.1. Rough substrates 20
4.3.2. Flat substrates 24
4.4. DISCUSSION 24
4.4.1. Nucleation on SiO_2 and on bare glass substrates 24
4.4.2. Distribution of amorphous phase within i-layer 25
4.5. CONCLUSIONS 25

5. INFLUENCE OF THE SILANE CONCENTRATION ON THE MICROSTRUCTURE OF μC-SI:H SOLAR CELLS 27

5.1. INTRODUCTION 27
5.2. EXPERIMENTAL 28
5.2.1. Cell fabrication 28
5.2.2. Characterization of the microstructure of the i-layer 28
5.3. RESULTS 29
5.3.1. Surface topography 29
5.3.2. Initial stages of the µc-Si:H growth 32
5.4. DISCUSSION 35
5.4.1. Microstructure of nip cells 35
5.4.2. V_{oc} of nip cells 38
5.5. CONCLUSIONS 40

6. NUMERICAL SIMULATION OF THE GROWTH OF µC-SI:H 41

6.1. INTRODUCTION 41
6.2. SIMULATION AND EXPERIMENTAL 43
6.2.1. Model description 43
6.2.2. Model Interpretation 45
6.2.3. Growth experiments and Measurements 46
6.3. RESULTS AND DISCUSSION 46
6.3.1. Microstructure 46
6.3.2. Phase diagram of the model 48
6.3.3. Phase transition versus desorption probability 50
6.3.4. Growth dynamics 50
6.3.5. Further work 50
6.4. CONCLUSIONS 52

7. EVALUATION OF I-LAYER QUALITY BY FTPS 53

7.1. INTRODUCTION 53
7.1.1. i-layer quality versus deposition conditions 53
7.1.2. Sub-gap absorption spectroscopy applied to complete cell . 53
7.1.3. Main results 56
7.2. EXPERIMENTAL 56
7.2.1. Principles of FTPS 56
7.2.2. Samples 61
7.3. RESULTS 61
7.3.1. FTPS spectra and proton irradiation 62
7.3.2. FTPS spectra and silane concentration 65
7.3.3. Defect related absorption and SC 68
7.3.4. Urbach tail slope 69
7.3.5. Crystalline volume fraction evaluated by FTPS spectra 71

7.4. DISCUSSION 73
7.4.1. Crystalline volume fraction obtained by Raman and FTPS. 73
7.4.2. Material quality of the i-layer 75
7.5. CONCLUSIONS 75
8. RELATIONSHIP BETWEEN I-LAYER QUALITY AND V_{OC} ... 77
8.1. INTRODUCTION 77
8.2. EXPERIMENTAL 77
8.3. RESULTS 77
8.3.1. V_{oc} versus SC 77
8.3.2. V_{oc} and amorphous volume fraction 80
8.3.3. V_{oc} and sub-gap states 82
8.4. DISCUSSION 83
8.4.1. V_{oc} basics 83
8.4.2. Amorphous fraction, defect density and V_{oc} 86
8.4.3. Nuclei density and V_{oc} 86
8.5. CONCLUSIONS 87
9. CONCLUSIONS 89

The Stone Age came to an end, not because we had a lack of stones, and the oil age will come to an end not because we have a lack of oil.
Sheik Yamani,
Oil Minister of Saudi Arabia in 1973

1. Introduction

Thin film silicon solar cells constitute one of the most promising directions for photovoltaics. As a matter of fact, the name says it all:

- Thin film: potentially cheap deposition process compatible with large area and mass production, large choice of rigid or flexible substrates (glass, metal, plastic, etc)
- Silicon: abundant and non-toxic element

These are the reasons why several companies like Japanese giants Kaneka Corp. and Canon as well as the Swiss companies VHF-technologies and Unaxis Solar are involved in thin film solar cells production.
The thin film silicon solar cells, as deposited by various techniques, are either amorphous, microcrystalline or both. The present thesis is focused on microcrystalline silicon solar cells.
Hydrogenated microcrystalline silicon (μc-Si:H) was introduced in 1968[1] and the first μc-Si:H based solar cells were made by J. Meier et al. in 1994[2]. In the Neuchâtel group, μc-Si:H is deposited by very-high frequency (VHF) plasma enhanced chemical vapor deposition (PECVD), from a gas mixture of silane (SiH_4) and hydrogen (H_2). The microstructure of the resulting μc-Si:H films strongly depends on the silane concentration (SC) defined as the gas flow ratio $SC=[SiH_4]/[SiH_4+H_2]$ used for deposition of the intrinsic layer (i-layer)[3-6].
It was reported that the μc-Si:H solar cells with the highest open-circuit voltage are deposited with SC close to the μc-Si:H/a-Si:H transition[7]. Under these conditions, crystallinity and microstructure of the resulting i-layer are critically substrate-dependent[8].
For deposition conditions close to the amorphous to crystalline transition, the material may gradually change from amorphous to crystalline during the course of the growth. This thickness evolution of the material crystallinity was first observed for a thickness series of cell within the range 0.5μm to 1.5μm[9].
Despite the complexity in material microstructure, microcrystalline solar cells were fabricated in different laboratories, with electrical conversion efficiencies over 9%[10-12]. Comprehensive reviews on μc-Si:H and its

combination with amorphous silicon (the so-called “micromorph” concept) for solar cell applications are presented elsewhere[13, 14].

For further improvements of µc-Si:H based solar cells, a better understanding of its microstructure and, consequently, its growth are necessary. Furthermore, the relationships between the various microstructures of µc-Si:H and the electrical properties of the devices are to be better understood.

For these reasons, the following chapter 2 focuses on a description of the experimental techniques used here; chapter 3 addresses the study of the microstructure of µc-Si:H by transmission electron microscopy (TEM). The terminology used for the description of the microstructure is introduced as well as a qualitative description of the device microstructure. It is also shown that the substrate, i.e. here the transparent conductive oxide (TCO), has a strong influence on the nucleation and the microstructure of the subsequent layers and cells. It is concluded that one should be very careful when one compares layers deposited under the same conditions on different substrates.

Chapter 4 is focused on the influence of the substrate on nucleation and microstructure of the subsequent µc-Si:H layer. Intrinsic layers were deposited under the same conditions on different substrates, which have the same surface morphology but a different surface chemistry. It is shown that the substrate surface chemistry influences the nucleation of the i-layer in a major way. Comparing then the results between layers grown on flat and rough substrate having the same surface chemistry, it was observed that substrate surface morphology has negligible effect on nucleation. However, the substrate surface morphology has a strong effect on the subsequent layer crystalline volume fraction.

Chapter 5 includes a quantitative evaluation of the microstructure changes that occur within µc-Si:H solar cells when SC is varied towards the microcrystalline to amorphous transition. TEM demonstrated that most of the changes occur in the first stages of the growth of the i-layer. Indeed the nuclei density decreases and the thickness of the mixed phase (amorphous/microcrystalline) layer increases when SC is raised. Further measurements by Raman spectroscopy[15, 16] on the same samples revealed that changes also occurs at the final stages of the growth of the i-layer, but they are not visible on the TEM micrographs. It is observed that the higher is SC, the larger is the amorphous fraction within the i-layer. This increase of the amorphous fraction within the i-layer coincides with an increase of the V_{oc}. An attempt to explain this behavior is made in chapter 8.

Chapter 6 presents an innovative 3-dimensional growth model, based on two simple selection rules. It is based on only three parameters that can be intuitively be related to: (i) the critical size of nuclei, (ii) the number of possible crystallographic orientations used to define the material and (iii) the desorption probability. This simple model is able to reproduce the main characteristics of the growth dynamics and microstructure of μc-Si:H:

- Conical shape of the grains
- Thickness transition from amorphous to crystalline material
- Amorphous to crystalline transition with respect to desorption probability
- Surface roughness evolution with respect to layer thickness

This simple model gives some clues to understanding the growth dynamics and microstructure of μc-Si:H layers.

Chapter 7 describes a study of the electronic quality of the i-layer within the active solar cell with a new technique developed by M. Vanecek et al.[17, 18]: the Fourier transform photocurrent spectroscopy (FTPS). This technique allows for the measurement within the working device of the absorption spectrum of the i-layer over several orders of magnitude.

The experimental evidence of a relationship between the low photon energy FTPS signal (FTPS at 0.8eV) and the defect density in the active layer of the solar cell was found by artificially creating electronic defects by proton irradiation. The samples were then successively thermally annealed and measured by FTPS. It is shown that the defect related absorption decreases as the annealing steps are performed.

In order to observe the influence of SC on the defect density two series of cells deposited with increasing SC were characterized. The FTPS measurements show that the defect related absorption decreases as SC is raised. FTPS therefore provides valuable information on the quality of the i-layer within working solar cells.

Chapter 8 compares the i-layer properties, as evaluated by their FTPS spectra, with the electrical performances of the solar cells. More specifically, a relationship is established between the V_{oc}. and the defect related absorption measured by FTPS at 0.8eV.

A short summary and the conclusions follow in chapter 9.

2. Deposition and characterization techniques

2.1. Introduction

The deposition and the characterization techniques used in this thesis for μc-Si:H solar cells are presented.

2.2. Solar cell structure

The thin film silicon solar cells studied here are constituted of a p-doped layer, an intrinsic (i-) layer and an n-doped layer sandwiched between a front transparent conductive oxide (TCO) and a back conductive contact (either TCO layer and/or a metallic contact). The whole structure is supported by a substrate, e.g. glass, metallic or plastic foil. The cell configuration is said to be nip or pin, the first letter (p or n) indicating which of the layers was first deposited on the substrate. As light always enters the p-layer side first, the pin cells must be deposited on transparent substrates whereas the nip cells can be deposited on opaque substrates too.

2.3. Transparent conductive oxide (TCO)

Two kinds of TCOs were used, both based on zinc oxide (ZnO):

- The most commonly used TCO in the Neuchâtel group is ZnO obtained by low-pressure chemical vapor deposition (LPCVD) from a vapor mixture of diethyl zinc, water and diborane (for the control of the doping). As grown LPCVD ZnO is rough: rms-roughness of 60nm for a thickness of 2.4μm. Thus, it constitutes a light diffuser that enhances the light trapping within the solar cell.
- Another kind of TCO consists of Aluminum-doped ZnO, which is deposited by RF magnetron sputtering. As grown sputtered ZnO is flat (rms-roughness of 5nm).

Details about the various deposition regimes of LPCVD ZnO and its role as a light diffuser can be found in refs. [19] [20]. One should mention that ZnO is not the only TCO available: indium tin oxide (ITO), tin oxide (SnO_2), are further examples among other kinds of TCO used in photovoltaics.

2.4. Silicon deposition

Microcrystalline silicon layers and cells presented here were deposited by VHF-PECVD[21]. The main deposition parameters used to obtain amorphous or microcrystalline silicon with this technique are the following:

- Plasma excitation frequency
- Power injected into the plasma

- SC of the gas phase mixture

It should be mentioned that there are many other parameters, such as temperature or pressure but also less versatile parameters such as the chamber and electrode geometries or the substrate itself.
The transition from amorphous to microcrystalline is obtained in the region of deposition parameter space where the plasma frequency or the power are high, or for low SC. In this thesis, the focus is on the latter deposition parameter and on its influence on the microstructure and the electrical properties of the µc-Si:H cells.
A comprehensive review of the VHF-PECVD technique for the deposition of amorphous and µc-Si:H solar cells is presented in ref [22].

2.5. Characterization techniques

2.5.1. Illuminated I(V) measurement

Current-voltage characteristics of the illuminated solar cells are obtained with the help of Wacom sun simulator that reproduces approximately the AM1.5 solar spectrum. The AM1.5 spectrum intensity of $100 mW/cm^2$ corresponds to the average illumination on earth produced by a light incidence of 48º. Open-circuit voltage (V_{oc}), fill-factor (FF), short-circuit current density (I_{sc}), maximum power point (V_{mpp}, I_{mpp}) are measured with I(V) set-up.

2.5.2. External quantum efficiency

The external quantum efficiency (EQE) is the measure of the number of electrons produced in the device per incident photon of a given energy. Experimentally, the solar cell is illuminated with a chopped light beam crossing a monochromator. The cell current density $i(E_{photon})$ is measured and divided by the incident flux of photons $\phi(E_{photon})$ determined with a reference detector, whose quantum efficiency is known.

$$EQE = \frac{i(E_{photon})}{q\phi(E_{photon})} \quad (2.1)$$

EQE can be performed under a voltage bias in order to superimpose an external electric field onto the internal field of the solar cell:
In <u>reverse bias</u>, the collection of the generated carriers increases (losses by recombination decreases). For a sufficiently high reverse bias, recombination losses become negligible and all generated electron-hole pairs are collected. By comparing the EQE curves with and without the reverse bias, one can therefore diagnose collection problems within a cell.

Quantum efficiency is used in forward bias, to evaluate the cell close to its working conditions (i.e. the maximum power point).
Quantum efficiency measurement can also be used to evaluate I_{sc} of the solar cells by integration (over the photon energy) of the product of EQE with the photon flux of AM1.5 spectrum. This method is more precise to determine I_{sc} than I(V) under a sun simulator when the solar cell area cannot be measured precisely.

2.5.3. Measurement of the sub-gap absorption coefficient

The absorption coefficient α is an important parameter, especially for photon energies below the band-gap energies (1.12 and 1.75eV for μc-Si:H and amorphous silicon, respectively). In that region the absorption coefficient is controlled by the gap states that are undesirable for solar cell applications. Indeed, they act as recombination centers, thereby limiting the electrical performances.

Photothermal deflection spectroscopy (PDS)

PDS[23] is a very sensitive technique for the measurement of the absorption coefficient α.

The sample, i.e. a single layer on a glass, is immersed into a transparent cuvette filled with a non-absorbing liquid whose index of refraction varies strongly with the temperature (CCl_4). In the transversal version of PDS, chopped monochromatic light shines perpendicularly on the sample and heats it locally. The local temperature increase of the liquid is measured as a function of the photon energy with the help of a laser that crosses the cuvette close and parallel to the immersed sample. The laser is deflected because of the locally varying index of refraction of the liquid (so-called 'mirage effect'). The laser deflection, read out on a position detector with the help of a lock-in amplifier, is proportional to the absorbance of the sample. The absorption coefficient α is then computed and scaled to the absolute magnitude by using the high energy region of the spectrum, where light is totally absorbed.

The absorption coefficient in the low energy region (around 1.2eV for amorphous silicon and 0.8eV for μc-Si:H) as measured by PDS is related to the defect density[24].

The sensitivity of the PDS technique is limited by the absorption of the glass substrate (down to α= 1cm^{-1} for a few micron thick silicon layer deposited on AF45 glass).

The PDS measurement is an interesting technique for characterizing single layers of thickness above 1μm deposited on glass. However it is not able to give any information on the i-layer as incorporated in the solar cell. In that

case, the free career absorption of the TCO is a few orders of magnitude larger than the absorption by the gap states of the silicon i-layer.

Constant Photocurrent method (CPM)

The CPM was introduced in 1981 by M. Vanecek et al.[25]. It allows for the measurement of very small absorption coefficient ($\alpha<10^{-2}cm^{-1}$). It is based on the following expression that relates the photocurrent I_{photo}, the photon flux ϕ and α:

$$I_{photo} \sim \phi(1-e^{-\alpha d}) \quad (2.2)$$

where d is the layer thickness. As indicated by the name of the method, the photocurrent I_{photo} must be kept constant. This is done practically for any photon energy by changing the incoming photon flux on the sample under measurement. When the condition of homogeneous absorption of light over the layer thickness ($\alpha d<<1$) is fulfilled, the above expression reduces to:

$$I_{photo} \sim \phi\alpha d \quad (2.3)$$

therefore constant photocurrent ensures that:

$$\alpha(E_{photon}) \sim \frac{1}{\phi(E_{photon})} \quad (2.4)$$

The measurement of the flux of photons required to keep the photocurrent constant at each photon energy as directed by a calibrated photo-detector, thus, yields to the relative absorption coefficient. Transmittance/reflectance measurements of the layer can be used to set the relative absorption coefficient on an absolute scale.

Fourier transform photocurrent spectroscopy (FTPS)

FTPS is described in details in chapter 7.

2.5.4. Microstructure characterization

Transmission electron microscopy (TEM)

TEM is the instrument that is able to give a direct picture of the microstructure of each layers constituting the cells: metallic contacts, TCOs, n-, i- and p-layers. This unique feature, however, has its price: it is a time consuming and a destructive technique.

The technique used here for sample preparation was introduced by Benedict et al.[26]. It consists of glueing surface-to-surface two pieces of the sample in order to obtain a « sandwich ». Then, a wedge with an angle between 0.6 and 0.8° is produced by mechanically polishing the sandwich. For this purpose, a polishing machine equipped with diamond papers of different grain sizes is used together with a dedicated tool, the so-called tripod polisher. At the end of the polishing process, the wedge thin side should measure less than the mean free path of the electrons (200nm in silicon for

electrons accelerated at 200kV voltage). The last (and sometimes unnecessary) step of the process is a short ion beam cleaning (typically a few minutes, on both sides of the sample, at a small ion beam angle with respect to the sample surface (8-12°)). The advantage of that technique over the thinning by ion beam only is that no amorphization of the sample can occur. Furthermore, with some practice, it is much faster than regular grinding and ion beam thinning.

TEM observations presented here were made on a Philips CM200 microscope operated at 200 kV. The interaction of electrons and matter assumed here is the elastic scattering, yielding contrast thanks to transmission and diffraction of the electron beam by the sample. One TEM imaging mode was used: the so-called medium resolution imaging mode. The electrons that cross the sample are separated into different beams: the directly transmitted beam and the diffracted beams. An aperture mechanically inserted on the optical axis of the microscope in the back focal plane of the objective lens selects either the transmitted beam or one of the diffracted beams. The images produced by the former electron beam are called bright field (BF) images whereas the images produced by one of the diffracted beams are called dark field (DF) images. In both cases, the contrast is given by the diffracting conditions (crystallographic orientations, lattice spacing) of the crystallites constituting the material under observation. For a complete introduction to the TEM techniques, see for instance ref. [27].

2.5.5. Micro-Raman spectroscopy

Micro-Raman spectroscopy is used to measure the amorphous or crystalline volume fractions of the μc-Si:H samples[28].

A monochromatic excitation beam (a laser beam) is focused through a microscope on the sample surface. Its frequency shift due to energy exchange between photons and phonons is measured. This inelastic scattering yields information on the bonding environment and therefore allows one to measure the relative amount of amorphous and crystalline phase in a layer.

Depending on the wavelength of the excitation beam, the depth of the probed volume can be varied. Here 633 and 514nm excitation lines were used to measure the samples, corresponding to collection depths of 500nm and 40 nm in μc-Si:H, respectively. There are three Raman peaks contributing to the Raman spectrum of μc-Si:H silicon: the crystalline peak at $520cm^{-1}$, the peak associated with the grain boundaries at $510cm^{-1}$ and a broad peak centered at $480cm^{-1}$ for the amorphous silicon. The integrated

areas of the peaks (I) are used to evaluate the Raman crystallinity factor ϕ_c defined below:

$$\phi_c = \frac{(I_{520} + I_{510})}{(I_{480} + I_{510} + I_{520})} \quad (2.5)$$

Note that ϕ_c is a relative measurement of the crystalline fraction that does not take into account the different Raman cross-sections of the amorphous and crystalline phases.

2.5.6. X-ray diffraction

X-ray diffraction (XRD) was used to measure the crystallographic orientations of the layers and cells as well as the grain size of the crystallites. XRD spectrum of a silicon powder is used as a reference to observe preferential crystallographic orientation. The normalized integrated peak intensities of the 111, 220, 311 and 400 directions, I_{111}:I_{220}:I_{311}:I_{400}, for a silicon powder are 100:55:30:6. Any deviations from these ratios are interpreted as preferential crystallographic orientation.

Integrated peak intensities also provide qualitative information on the average crystallinity of the samples. The X-ray spectrometer was a Philips PW3020 diffractometer used in the Bragg-Brentano geometry (ϑ-2ϑ scans). An accelerating voltage of 30kV and a current of 30mA were used to produce Cu K_α radiation at a wavelength of 1.5418 Å.

3. Description of the microstructure of μc-Si:H

3.1. Introduction

The present chapter introduces and defines the terminology used here to describe accurately the microstructure of microcrystalline layers and cells, as observed mainly with TEM.

Here, TEM and XRD were used to observe the variations of the microstructure and crystallographic properties of the samples deposited under the same conditions on different substrates. It is reported in this chapter that the microstructure of layers is highly influenced by the substrate morphology and its chemical nature. However, on the basis of the experiments carried out here, it is impossible to distinguish between these two effects of the substrate. Further experiments were made to separate the influence of the substrate morphology and its chemical nature on the microstructure of the subsequently grown material in chapter 4. The microstructure evolution as a function of SC is studied in chapter 5.

3.2. Experimental

This study is based on the investigation of four samples: two individual i-layers (samples A and B) and two entire nip solar cells (samples C and D), deposited by VHF-PECVD, on various substrates; all i-layers (individual i-layers and those within the nip cells) were deposited with the same deposition parameters: substrate temperature of 250 ºC, chamber pressure of 0.5 mbar, injected power of 30 W, excitation frequency of 130 MHz and SC=7%. These deposition parameters result in a layer close to the microcrystalline to amorphous transition. The thickness of all i-layers is comprised between 2.3 and 2.5μm. The underlying substrate material was in all cases sodium free AF-45 glass substrate. Layer A was deposited directly on glass, layer B on aluminum-doped sputtered ZnO, cell C on sputtered ZnO and cell D on boron-doped LPCVD ZnO. The n-μc-Si:H layers of both cells were deposited under conditions that should result in microcrystalline material. Both i-layers (A and B) were deposited in the same run, as were both nip cells (C and D).

3.3. Results

XRD spectra of layers A and B (an individual i-layer on glass and on sputtered ZnO, respectively) show a clear dependence on the type of substrate (Figure 3.1): the i-layer is amorphous when deposited directly on glass substrate and it is microcrystalline when deposited on sputtered ZnO.

Here, under the same deposition conditions and in the same run, the substrate influence is so critical that it yields layers on both sides of the phase transition. TEM observations of layer A (not shown here), confirming the XRD spectra, exhibits an amorphous microstructure without any microcrystalline phase. The TEM bright-field micrograph of layer B is shown in Figure 3.3. Samples B and C (an individual i-layer on sputtered ZnO and an i-layer, within a nip cell, deposited on sputtered ZnO, respectively) exhibit similar XRD spectra (Figure 3.1) with a (220) preferential growth.

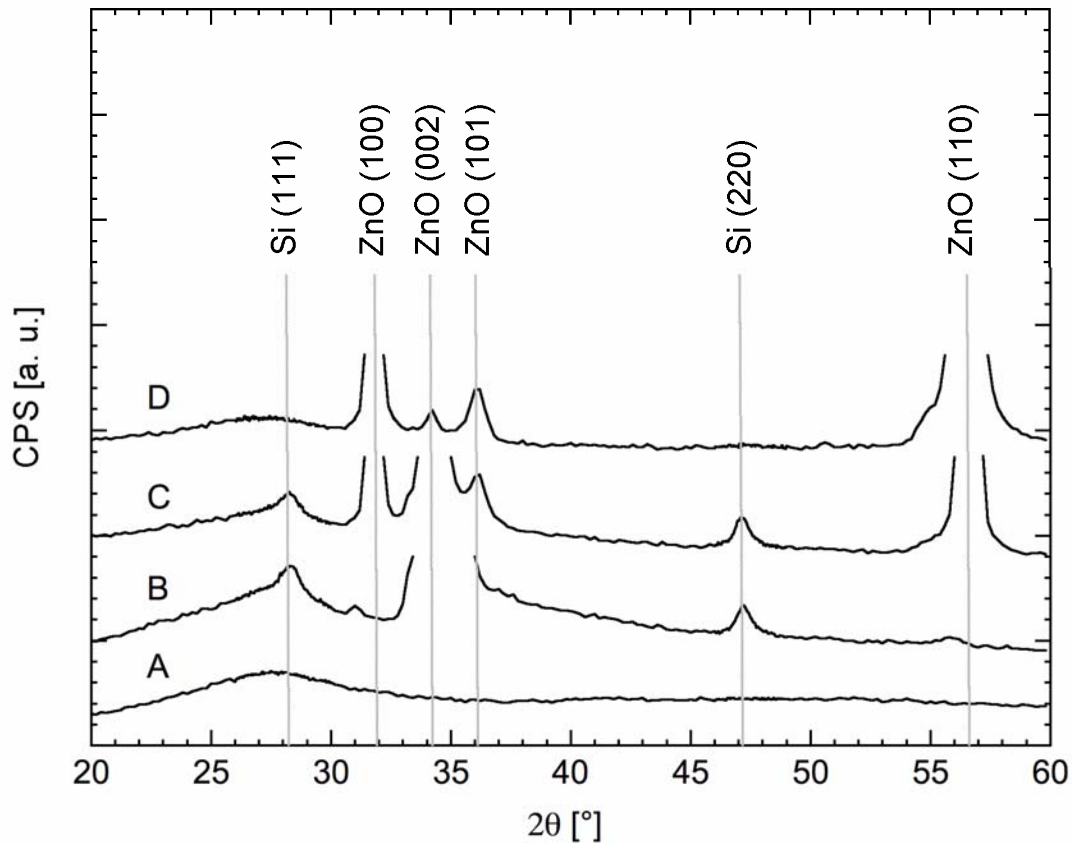

Figure 3.1: XRD spectra of A) amorphous i-layer deposited directly on glass, B) μc-Si:H layer deposited on sputtered ZnO, C) complete μc-Si:H nip cell with sputtered ZnO as back TCO and LPCVD ZnO as front TCO , D) complete nip cell, mostly amorphous, with LPCVD ZnO as back and front TCO. Note that μc-Si:H grows here with a (220) preferential orientation on sputtered ZnO (spectra B and C).

Despite similar XRD spectra, the TEM micrographs of samples B and C differ significantly. In sample B, nucleation of the crystalline phase starts after a few hundreds of nanometers of an amorphous incubation layer, as shown in Figure 3.3, whereas it occurs directly on the the n-μc-Si:H layer in

sample C (Figure 3.4). The i-layer nano-crystals grow epitaxially over the microcrystalline n-doped layer, confirming previous observations[29], and follows a direction normal to the substrate (Figure 3.2).

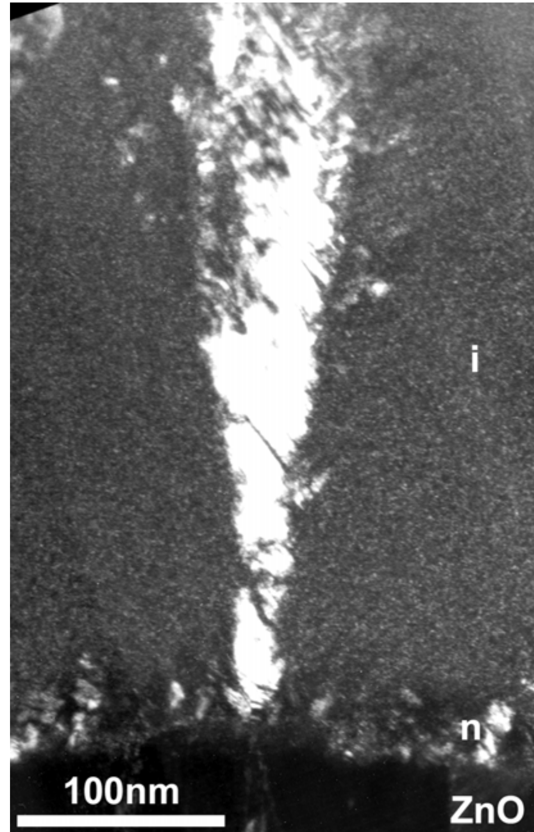

Figure 3.2: TEM dark-field cross-section of a conical shaped microcrystalline nano-crystal (white) embedded in amorphous silicon (grey background) in sample C. The dark region at the bottom of the micrograph is sputtered ZnO. On top of it, one distinguishes the dotty 20nm-thick microcrystalline n-layer. In dark-field imaging mode, white contrast is observed for each single nano-crystal fulfilling diffraction conditions prevailing in the TEM. Here the conical nano-crystal grows epitaxially from the n-layer and extends into the i-layer.

In both cases, the overall microstructure of μc-Si:H is characterized by conical conglomerates of crystallites of a diameter of tens of nanometers (Figure 3.2). These conical conglomerates are characterized by an average opening angle of 23°, with respect to the normal to the substrate, in sample B and an average opening angle of 15° (from normal to cone edge) in sample C.

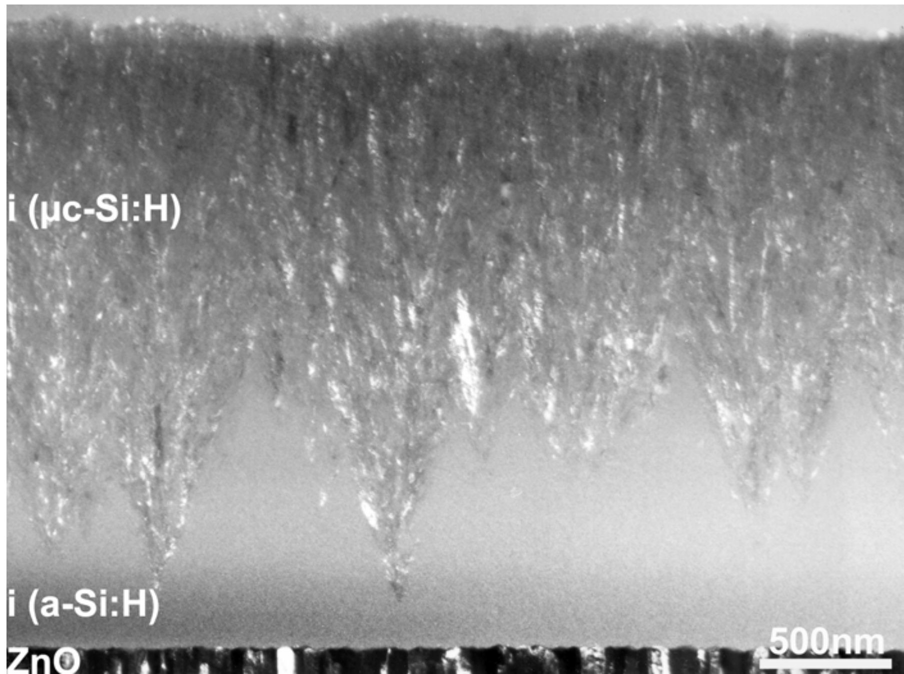

Figure 3.3: TEM dark field micrograph of an i-layer deposited on sputtered ZnO (sample B). Diffracting crystallites appear bright in this imaging mode; sputtered ZnO layer is at the bottom of the picture.

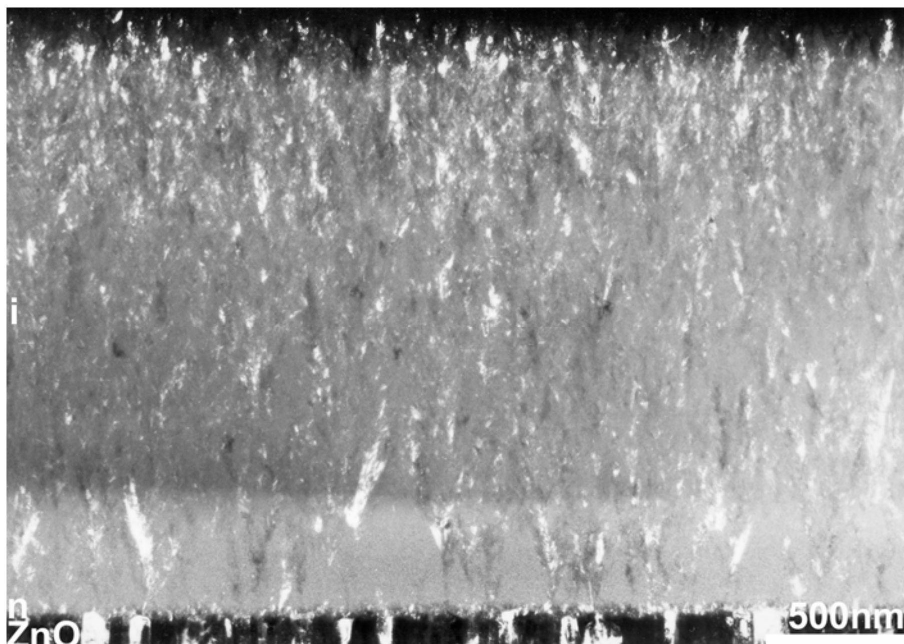

Figure 3.4: TEM dark field micrograph of an nip solar cell deposited on sputtered ZnO (sample C). Sputtered ZnO is the high contrast region at the bottom of the picture, n-μc-Si:H layer appears as a thin dotty layer.

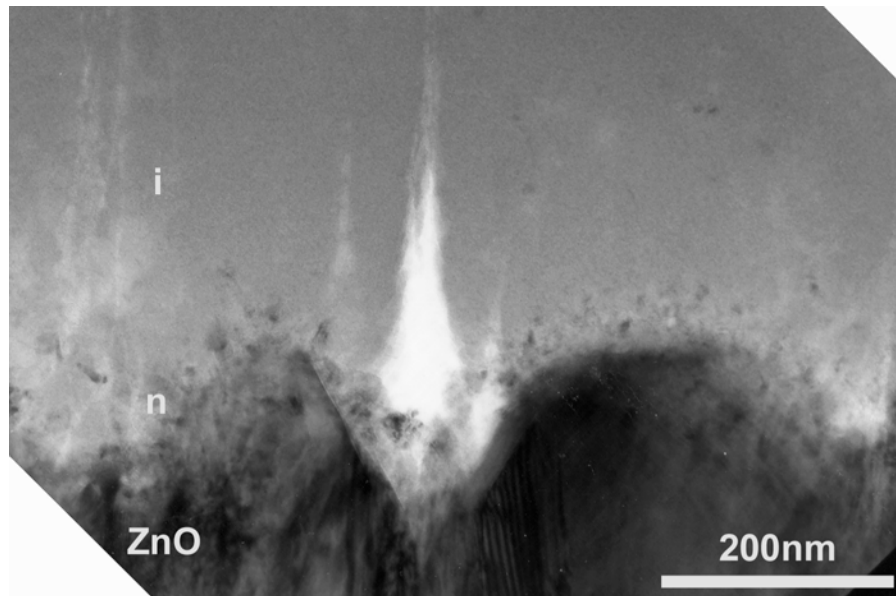

Figure 3.5: TEM bright field micrograph of the ZnO-n-i interface of a solar cell deposited on LPCVD ZnO. Typical cross-sections of ZnO pyramids appear at the bottom of the picture. On top of it, note the disordered grainy contrast of the n–layer. Cracks/voids at the bottom of ZnO valleys appear bright. i-layer is mostly amorphous (homogeneous grey region).

Samples C and D (the nip cell on sputtered ZnO and the nip cell on LPCVD ZnO, respectively) differ dramatically (see Figure 3.4 and Figure 3.5): cell C has a considerable crystalline fraction, whereas cell D is mostly amorphous, as seen on the XRD spectrum of the whole cell in Figure 3.1. Electrical characteristics measured under AM 1.5 of cell C included an open-circuit voltage of 530 mV, a short-circuit current of 15.5 mA/cm2 and a fill factor of 68%. On the other hand most of the cells deposited on LPCVD ZnO substrate were shunted, however we estimate that their Voc is over 500 mV. From the microstructural point of view, the two different types of ZnO used in these two cells differ in their surface roughness (LPCVD ZnO is rougher than sputtered ZnO), in their crystallographic texture ((110) preferential growth of LPCVD, in Figure 3.1) and in the grain size (sputtered ZnO has smaller grains), as shown in Figure 3.4 and Figure 3.5. We also observed that the n-µc-Si:H layer « quality » is not as good on LPCVD ZnO as on sputtered ZnO: on the latter, the grains constituting the n-µc-Si:H layer are closely packed crystallites of a diameter approximately equal to the thickness of the n-µc-Si:H layer ; the thickness of the n-doped layer is homogeneous and the n-i interface is clearly defined. On the other hand, with LPCVD ZnO (sample C), n-i interface is not as well defined and the n-µc-Si:H layer thickness presents fluctuations on the scale of tens of

nanometers. Thus, the n-μc-Si:H layer grown on the rougher LPCVD ZnO looks more disordered than the n-μc-Si:H layer grown with the same conditions on sputtered ZnO. Furthermore, we observed in sample C cracks/voids occuring at the bottom of valleys as already reported[4, 5].

3.4. Discussion

We have shown above that the nature of the layer over which the intrinsic μc-Si:H layer is deposited, is critical for the amorphous/microcrystalline nature of the i-layer itself. This is observed for layers deposited at SC close to the microcrystalline to amorphous phase transition. From the TEM micrographs, we can observe a pronounced depth inhomogeneity of the layers; this fact must be considered when analyzing mixed-phase amorphous/microcrystalline layers[30]. Such a depth inhomogeneity can, in fact, not be inferred from the XRD spectra alone. The latter are only relevant for the evaluation of the « average » crystallinity. Furthermore, the TEM observations clearly demonstrate the critical effect of the substrate and the underlying layer on the growth of the i-layer.

3.4.1. Definitions

In order to describe precisely the microstructure as observed with TEM, the terminology used through this work is defined below:

Crystallite or nano-crystal: single crystal of any shape, the size of which is between a few nanometers up to a few hundreds of nanometers (see for example Figure 3.2).

Conglomerate or grain: assembly of crystallites, generally of a conical or cylindrical shape.

Nucleus (pl. nuclei): first crystallite of a conglomerate.

Incubation layer: fully amorphous silicon layer below the first nucleus in the layer.

Heterophase layer: mixed phase layer (amorphous and microcrystalline phases) that starts from the first nucleus and goes up to the coalescence of the conglomerates.

Coalescence threshold: layer thickness at which the conical conglomerates meet; it equals the sum of the thicknesses of the incubation layer and the heterophase layer.

3.4.2. Conical shape of conglomerates

The observations on samples B and C reveal a conical shape of conglomerates, an opening angle of approximately 23° and 15° respectively, and a crystalline coalescence threshold of a few hundreds of nanometers.

These data are in agreement with the growth model proposed in ref.[31], where an opening angle of 15º was assumed. One may understand the angle discrepancy with simple geometrical considerations. In sample C (15°), where all microcrystalline cones start from the bottom of the layer, the TEM cross-section crosses the 20nm nuclei, and thus the measured angle is the real half-angle of the cone apex. In sample B (23°), the cross-section possibly cuts the conical conglomerates off the starting nucleus, the measured angle is thus larger than the half-angle of the apex. A model reproducing the conical shape and columnar growth of the microcrystalline material is presented in chapter 6.

3.4.3. Nucleation and thickness transition

As the samples were all deposited with the same SC, the only parameters influencing the phase transition are the nature of the substrate and the nature of the n-µc-Si:H layer (if any). These two parameters influence the thickness of the incubation layer. For sample B (i-layer on sputtered ZnO), the thickness of the amorphous incubation layer is in the range of hundreds of nanometers, while for sample C (nip cell on sputtered ZnO) the n-µc-Si:H layer plays the role of a seed layer promoting microcrystalline growth. However, after crossing the crystalline coalescence threshold, the microstructure of both samples B and C is similar, as far as TEM observation is concerned. Consequently, the influence of the n-µc-Si:H layer on the crystalline fraction vanishes when the thickness increases, resulting in similar XRD spectra, for thick enough layers.

In sample C, the n-µc-Si:H layer deposited on a flat sputtered ZnO, is of higher « quality » (with respect to its microstructure as observed from TEM micrographs) than the one deposited on rough LPCVD ZnO (sample D). For sample D, this leads to a thicker amorphous incubation layer. In fact, sample D never reaches the coalescence threshold. The crystalline quality of the n-µc-Si:H layer is, thus, of great importance for the control of the microcrystalline growth of the i-layer.

3.5. Conclusions

In this chapter, comparisons between four samples were made with the help of XRD and TEM in order to study the influence of substrate and the underlying layer on the microstructure of µc-Si:H layers and cells. It was shown that in a typical nip solar cell deposited on a ZnO layer:

- The surface morphology of ZnO (surface roughness, crystallographic orientation and grain size) is of paramount importance to control the direction of the grains and the quality of the n-µc-Si:H layer.

- The n-µc-Si:H layer influences the nucleation and microstructure of the i-layer.

Every underlying layer influences the nucleation and the microstructure of the subsequent layer: TCO influences the n-layer, which, in turn, influences the i-layer. One therefore calls for extreme prudence when comparing i-layers and entire solar cells deposited on different substrates.

For this reason, this thesis is focused on the characterization of the full microcrystalline cells and specifically on the i-layer properties within the active device (see chapter 5, 7 and 8).

Further experiments were carried out in chapter 4 to distinguish the effect of the surface morphology and the chemical nature of the substrate on the nucleation and growth of the subsequent layer.

4. Growth of µc-Si:H layers: influence of substrate surface chemistry and topography

4.1. Introduction

In the previous chapter, in accordance with other studies[32-35], the effect of substrate on the microstructure of µc-Si:H was evidenced, though the distinction between the effect of geometry and chemistry of the substrate surface could not be done on the basis of the set of samples used there. This chapter is devoted to distinguishing between these two effects.

The substrate topography has been shown to be determinant for growth, as µc-Si:H nano-crystals start to grow perpendicular to the substrate facets[5, 29]. The substrate therefore controls the orientation of the nano-crystals growing on it.

On the other hand, a study on a few nm thick silicon layers deposited on silicon nitride and silicon dioxide (both obtained by PECVD) showed that the surface chemistry of the substrate influences the density of nano-crystals[35]. Silicon nitride was shown to inhibit nucleation whereas silicon dioxide promoted it.

The effect of the substrate on microstructure is an important issue in solar cells as the crystalline fraction, as well as its distribution within the i-layer, controls the opto-electrical properties of the device (see chapters 7 and 8).

The aim of this chapter, with the help of samples dedicated to that purpose, is to observe the influence of surface chemistry and surface roughness on the growth of µc-Si:H layers (approximately 500nm thick) deposited on substrates, which have a morphology and a surface roughness representative of the one used in solar cells (rms-roughness of 50-60nm).

It is found here that the surface chemistry of the substrate has a major effect on the nucleation process whereas its surface geometry does not. On the other hand, the substrate geometry influences the distribution of the amorphous and microcrystalline phases within the µc-Si:H layer.

4.2. Experimental

Intrinsic µc-Si:H layers of approximately 500nm were deposited in the same run on substrates with different surface roughness and surface chemistry. The deposition conditions of the µc-Si:H layers included a plasma frequency of 110MHz, a substrate temperature of 180°C, a chamber pressure of 0.3mbar and SC of 5%, yielding µc-Si:H material close to the microcrystalline to amorphous transition.

The μc-Si:H layer was deposited on four rough substrates with the same surface topography: the typical pyramid-like surface of LPCVD ZnO deposited on glass. The LPCVD ZnO layer was covered in a conformal way with thin layers (approximately 20nm) of different materials to change the surface chemistry. Rough sputtered ZnO (R-sZnO), rough PECVD SiO2 (R-SiO_2), rough chromium (R-Cr) and bare LPCVD ZnO (R-ZnO) were obtained.
Two flat substrates were also used for comparison, i.e. thin sputtered ZnO (F-sZnO) and thin PECVD SiO_2 (F-SiO_2) layers deposited on glass.
The layer crystallinity was characterized by Raman spectroscopy in the backscattering configuration with the 633nm excitation line of a HeNe laser, with the light impinging on the top of the microcrystalline layer.
The layer microstructure was investigated with TEM. The average crystallinity of the layers was evaluated directly on the TEM micrographs with the help of transparencies. The amorphous phase was drawn black on the transparency, leaving the microcrystalline phase white. The obtained sketch of the microstructure was then digitalized and the ratio of white to total area was evaluated numerically.

4.3. Results

4.3.1. Rough substrates

Figure 4.1 shows the microstructure of three layers deposited in the same run on different substrates: a) R-sZnO, b) R-ZnO and c) R-SiO_2. The microstructure may look similar at first glance: surface roughness of the substrates are comparable and conical conglomerates of nano-crystals separated by amorphous phase and/or voids can, indeed, be observed on each of the three micrographs. A closer look, however, shows that the crystalline fraction and the nuclei density increases from micrograph a) to c) (see also Figure 4.2, Figure 4.3 and Figure 4.4). The fourth layer microstructure, grown on R-Cr substrate (no TEM micrograph is shown here) is comparable to R-sZnO. On the rough substrates, the amorphous phase is lying mainly at the bottom of the layer, though one may still observe amorphous material at the top of the layer. In Figure 4.4, the crystalline fraction estimated by TEM is shown. It follows the same trend as the crystalline fraction evaluated with Raman spectroscopy. Note that, for the rough substrates, the crystalline fraction increases in the same way as the nucleation density (Figure 4.5).

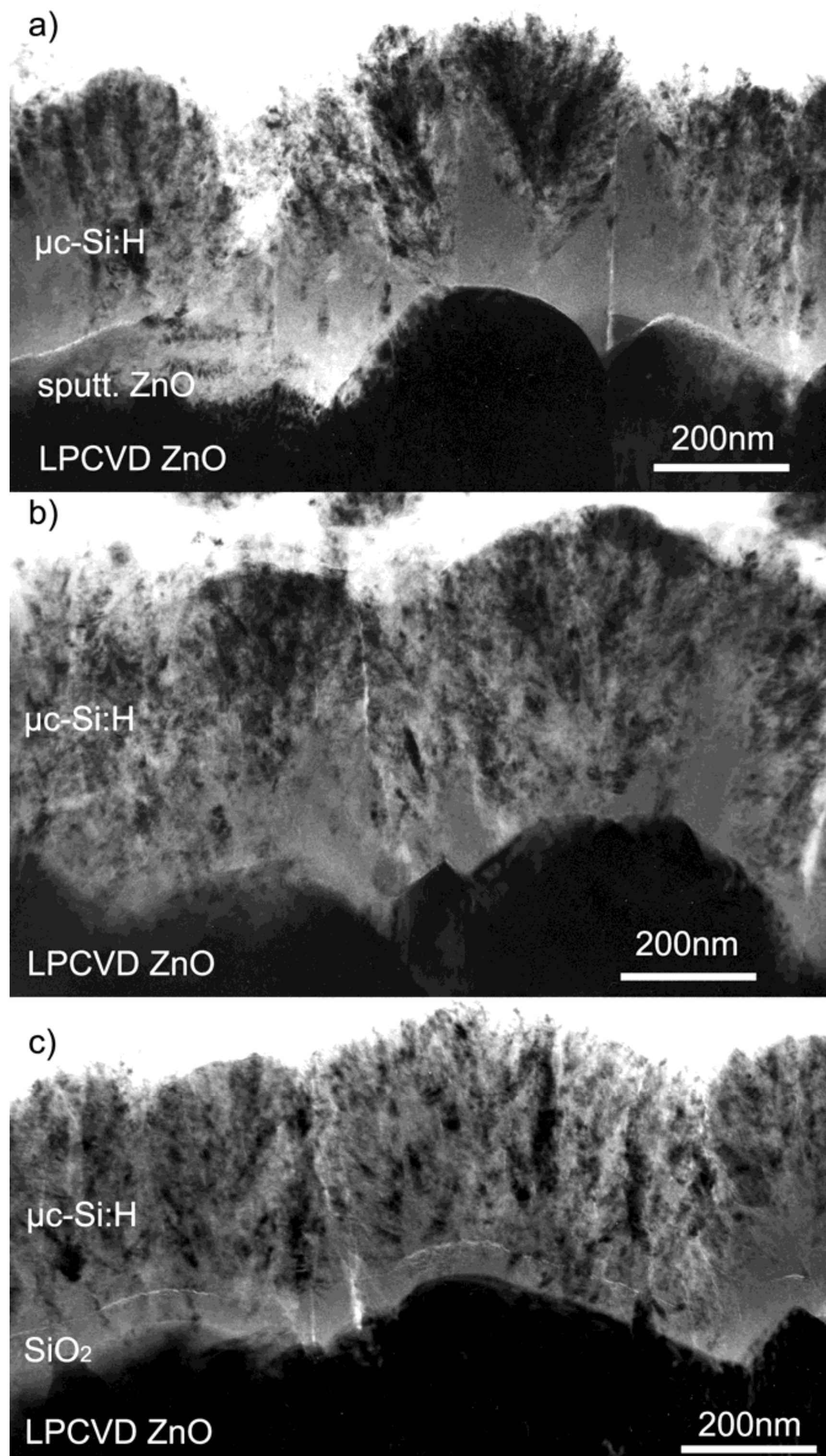

Figure 4.1:BF TEM micrographs of i-layers on rough substrates. a) i-layer on R-sZnO, b) i-layer on R-ZnO, c) i-layer on R-SiO_2. From a) to c) n_d increases as well as ϕ_c. See the comments in the text (section 4.3.1).

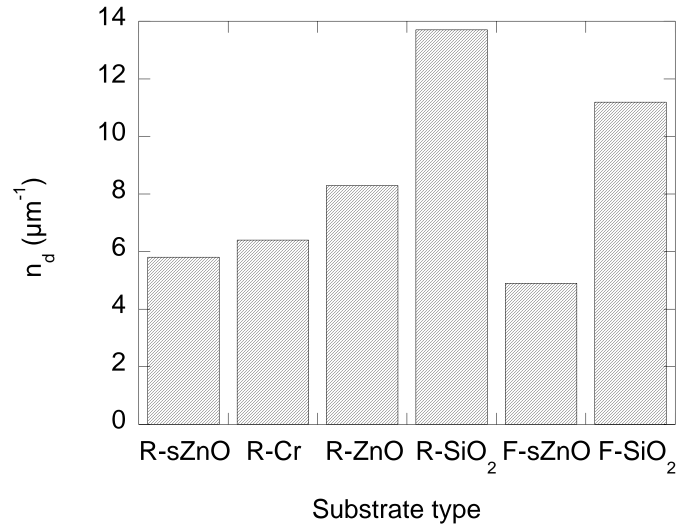

Figure 4.2: Nuclei density n_d evaluated from TEM micrographs as a function of the substrate type (error on n_d is approximately ±10%). For both flat and rough substrates, SiO_2 appears to be the most favorable layer for nucleation with an n_d of 12-14μm^{-1}. On the other hand, sputtered ZnO appears to be unfavorable to nucleation with an n_d of only 5μm^{-1}, for both flat and rough substrates.

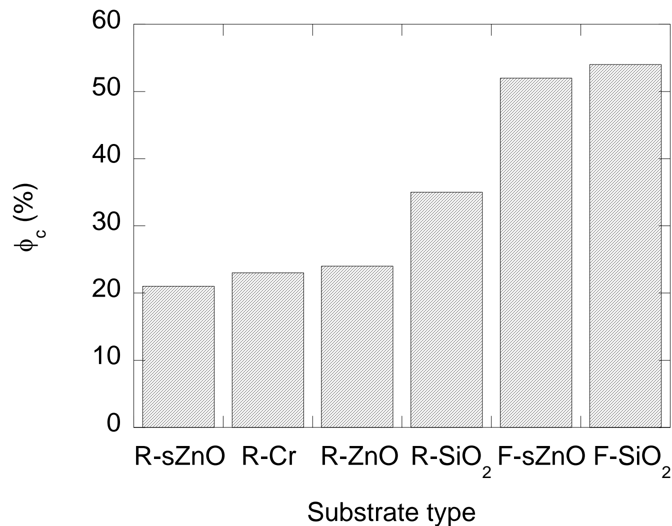

Figure 4.3: Raman crystallinity factor ϕ_c as a function of the substrate type (error on ϕ_c is ±5%). Although the collection depth is approximately equal to the layer depth (500nm), the effect of very different n_d on ϕ_c is not observed for the flat substrates.

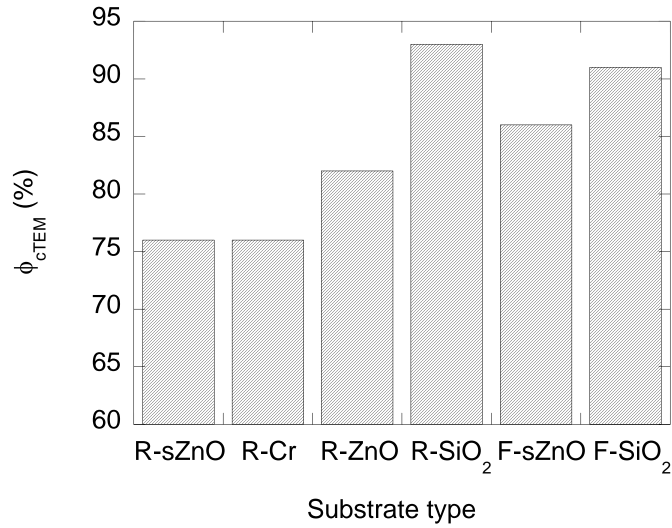

Figure 4.4: Crystalline fraction measured with TEM ϕ_{cTEM} (error on ϕ_{cTEM} is ±10%). On the contrary to Raman crystalline factor ϕ_c, ϕ_{cTEM} is not depth sensitive.

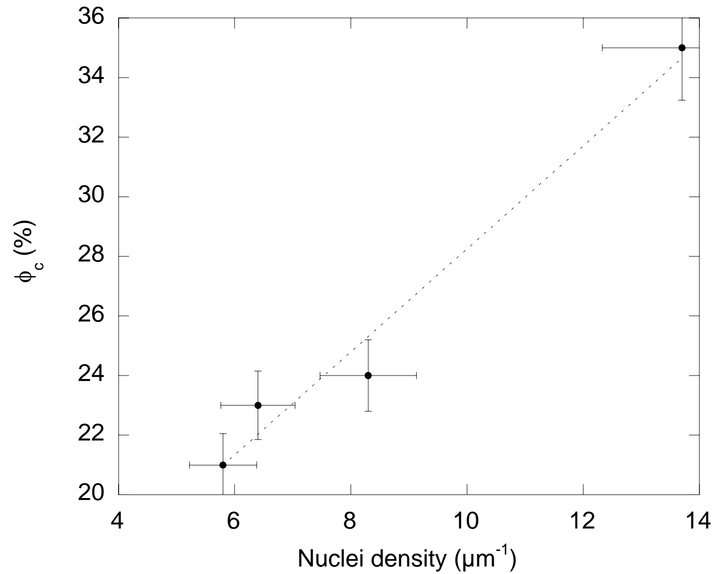

Figure 4.5: Raman crystallinity factor ϕ_c as a function of the linear nuclei density on the rough substrates. The dotted line is the linear least square fit to the data.

4.3.2. Flat substrates

For the two flat substrates (F-sZnO and F-SiO_2), TEM analysis shows that nuclei density is very different: 5 and 13μm^{-1}, respectively (Figure 4.2). Surprisingly, the crystalline fraction estimated by Raman is very similar, approximately 50% for both samples (Figure 4.3). The explanation is given by TEM micrographs (not shown here): the amorphous fraction in both samples is mainly lying at the bottom of the i-layer and no amorphous fraction is seen at the top, on the contrary to what is observed for the layers grown on the rough substrates. As the excitation beam (collection depth of 500nm) of the Raman spectroscope enters the layer (550nm thick) from its strongly microcrystalline top, it does not probe the amorphous phase lying at early stages of the layer.

4.4. Discussion

The preponderant role of the chemical nature of the substrate for the nucleation of µc-SiH is, thus, confirmed here. The fact that nuclei density is barely dependent on the surface roughness of the substrate was already observed[34, 35], though for much smaller substrate roughness (in the range of a few nm). The present study, therefore confirms those observations for substrate roughness typically used in photovoltaic devices (rms-roughness of 50-60nm), for light trapping purpose.

4.4.1. Nucleation on SiO_2 and on bare glass substrates

An unexpected result of this study is the observation of the largest nuclei density on PECVD-SiO_2. Indeed, it was observed in chapter 3 that nucleation of µc-Si:H on glass is harder than on sputtered ZnO; it was, therefore, expected that nucleation would be harder on SiO_2. One should however take into account that chemical nature of glass is not similar to SiO_2. Fortunately, a bare test glass substrate was put together with the other substrates (mentioned above) into the deposition reactor. Further measurements of the crystalline fraction on that sample revealed that layer grown on glass is indeed less crystalline, i.e. ϕ_c(glass)=46% instead of ϕ_c(F-SiO_2)=51%. One concludes that chemical composition of the substrate controls the nucleation density; even small changes of the chemical nature have observable effects on the nucleation of the subsequent layer. Plasma pre-treatment of the substrate are likely to play the same role. Such effects have been observed in a previous study[33], which showed that a polycrystalline layer deposited in the presence of hydrogen does influence the grain size on SiO_2.

It is interesting to notice that for thin film transistors (TFT), the best materials for gate dielectric (i.e. the material with the best passivation properties) for μc-Si:H and a-Si:H TFTs are observed to be silicon dioxide and silicon nitride, respectively. On the other hand, it is observed here that silicon dioxide has the best nucleation properties for μc-Si:H and in ref. [35] that silicon nitride promotes the growth of amorphous material.

4.4.2. Distribution of amorphous phase within i-layer

The layers grown on flat substrates studied here have a high amorphous fraction lying at the substrate interface. The Raman spectroscopy measurements performed on these samples revealed the depth sensitivity limits of that technique: both layers exhibit the same ϕ_c measured with Raman spectroscopy though they have a significantly different nuclei density (Figure 4.2 and Figure 4.3). Indeed, taking into account the exponential attenuation of the excitation light in the backscattering Raman configuration used here, one calculates that a 50nm amorphous layer lying at the bottom of a 550nm thick sample contributes only 6% (instead of 9% if proportional) to the Raman signal. Therefore, the amorphous fraction lying at the substrate interface can not be measured by Raman spectroscopy with the excitation beam entering the layer from the top.
On the other hand, in the layers grown on the rough substrates, the amorphous fraction extends much higher in the layer and contributes, thus, more to the collected Raman signal. This is due to the effect of substrate roughness on μc-Si:H microstructure. Indeed, μc-Si:H starts growing perpendicular to the substrate facets. On rough substrates the geometrical consequences of this growth process are an increased amorphous fraction in the whole layer, for a given nuclei density, as compared to a layer grown on a flat substrate. The crystallinity at the bottom of the sample can be evaluated with Raman measurements performed with excitation light entering the layer from the bottom. Such measurements on flat substrates yield a bottom crystallinity about 20% lower that the top crystallinity. The average crystalline fraction of the layer as measured from the TEM micrographs (Figure 4.4) is a more reliable measurement technique than the Raman crystalline fraction.

4.5. Conclusions

The microcrystalline and amorphous phase spatial distributions within the layer depend on the substrate topography. As previously observed, microcrystalline silicon starts growing perpendicularly to the substrate facets. For both flat and rough substrates, the influence of the chemical

nature of the substrate on the nucleation of the subsequent layer is shown to be preponderant. In particular, this study shows that nucleation density is the highest on PECVD SiO_2, compared with Cr, sputtered ZnO and LPCVD ZnO. Because of the geometrical effect of the local growth (perpendicular to the substrate facets) the amorphous fraction is more present at the top of the layers grown on rough substrates. Raman measurements for this kind of samples are in good agreement with the crystalline fraction as measured with TEM. Raman measurements on flat substrates indicate, however, the sensitivity limits of this measurement technique: the crystallinity measured on these samples is overestimated as the amorphous material is found mostly at the bottom of the layer. In order to interpret Raman crystalline fraction correctly one should, therefore, know qualitatively the microstructure of the layer under investigation.

5. Influence of the silane concentration on the microstructure of μc-Si:H solar cells

5.1. Introduction

μc-Si:H is commonly deposited by PECVD process using SiH_4 diluted with H_2 in the plasma gas phase. It is not a unique, well-defined material but a complex mixture of amorphous and microcrystalline silicon plus grain boundaries[36], as introduced in chapter 3. For a given substrate surface morphology, the respective amorphous/microcrystalline volume fractions depend mostly on SC used for the deposition of the material. Currently the best devices are obtained with i-layers prepared under conditions close to the amorphous /microcrystalline transition by varying SC, which is therefore an important parameter for the cell optimization[7, 11, 37]. Furthermore, in chapters 3 and 4, it was shown that the substrate plays a critical role on μc-Si:H nucleation and growth, particularly at deposition conditions close to the amorphous/microcrystalline transition.

However, an open question that remains is to what extent the material microstructure influences the electrical characteristics of the device. The present chapter is therefore first aimed at a quantitative description of the changes in the cell microstructure, with respect to changes of SC used for the deposition of the i-layer. The observed variations of the microstructure are then related to the electrical performances and, specifically to the open-circuit voltage.

For this study, the material as incorporated into the active device has been characterized with AFM, TEM and XRD whereas the active devices were characterized by I(V) and quantum efficiency measurements. These characterization techniques have been applied directly to two series of nip solar cells deposited at various values of SC. The two series were obtained by depositing the cells in the same run on two different substrates, namely on a glass substrate coated with sputtered Al-doped ZnO layer and on a glass substrate coated with boron-doped ZnO layer fabricated by LPCVD.

In the series of devices studied here, in contrast with samples produced in Juelich[11], the amorphous volume fraction is not homogenously distributed over the whole device thickness. The first stages of the i-layer that may extend through the first hundreds of nanometers, the microstructure consists of a mixture of conical conglomerates of crystallites embedded in an amorphous tissue that will be called thereafter the heterophase layer (see section 3.4).

The density of nuclei and the thickness of the heterophase layer are identified here as the dominant microstructural parameters in the relationship between material microstructure and device electrical performances.

5.2. Experimental

5.2.1. Cell fabrication

Two dilution series of nip μc-Si:H solar cells were deposited on glass substrates coated with TCO layers. A series of cells was deposited on aluminum-doped sputtered ZnO, a flat TCO (root mean square roughness of 4nm), whereas another series was deposited on boron-doped LPCVD ZnO, which is a much rougher TCO (rms=60nm). The nip cells were deposited in the same run on both TCOs at SC for the i-layer of 5, 5.5, 6, 6.5 and 7%. The other deposition parameters of the i-layer were a substrate temperature of 200ºC, a pressure of 0.5 mbar, a plasma excitation frequency of 130 MHz and a power of 30 W, and they were maintained constant in the whole series. Under these conditions, the thickness of the i-layer was approximately 2.2μm for the cells on sputtered ZnO and 2.7μm for the cells on LPCVD ZnO. The deposition parameters of the n and p-layers were the same for the whole series and were optimized in such a way as to produce highly microcrystalline material on glass.

5.2.2. Characterization of the microstructure of the i-layer

XRD was used on all the cells in order to evaluate the average crystallinity of the whole device.

TEM permits one to observe the microstructure of the various (ZnO, n, i and p) layers within the cell. A piece of each cell (except for cells deposited at 6% SC) was prepared as cross-section sample for medium range TEM examination[26].

AFM was performed on the top p-layer of the device in order to evaluate the root mean square roughness and the lateral size of the surface features. These measurements were performed in the non-contact (tapping) mode on a Vista Burleigh Instruments scanning probe microscope.

5.3. Results

5.3.1. Surface topography

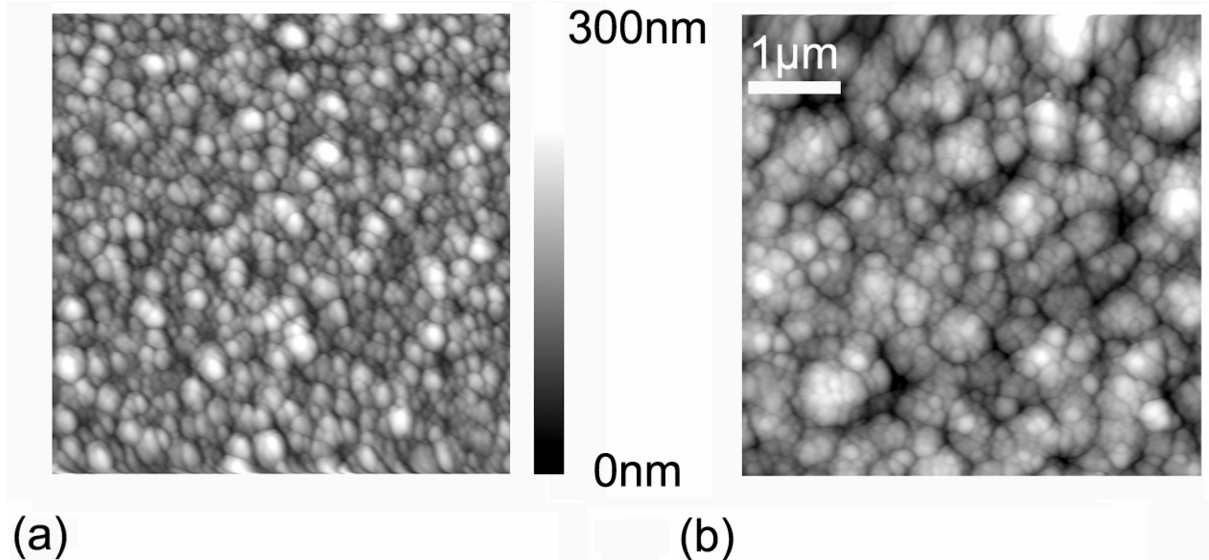

Figure 5.1: AFM scans of the top layer (p-layer) of the solar cell with SC= 5% on sputtered ZnO (a) and on LPCVD ZnO (b). Such topographies are representative of all the cells in the respective series. The lateral size of the surface features, measured from the Fourier transform power spectrum of the AFM scan is 600nm and 1000nm on sputtered ZnO and LPCVD ZnO, respectively.

In Figure 5.1 (a), an AFM scan of the top surface, i.e. the p-layer, representative of all the cells deposited on sputtered ZnO is given. By comparing the AFM and TEM micrographs on the same solar cell (cf. Figure 5.1 (a) and 2 (a)), we can conclude that conglomerates of crystallites with an average diameter of approximately 600nm emerge at the growing surface of the p-layer. In this dilution series, there is no major effect of SC on the surface roughness of the device, the latter being between 20 and 25nm (rms-value) (Figure 5.3). It is larger than the initial roughness of the TCO (rms=4nm) and it is similar to fully microcrystalline layers of comparable thickness directly deposited on glass[3].

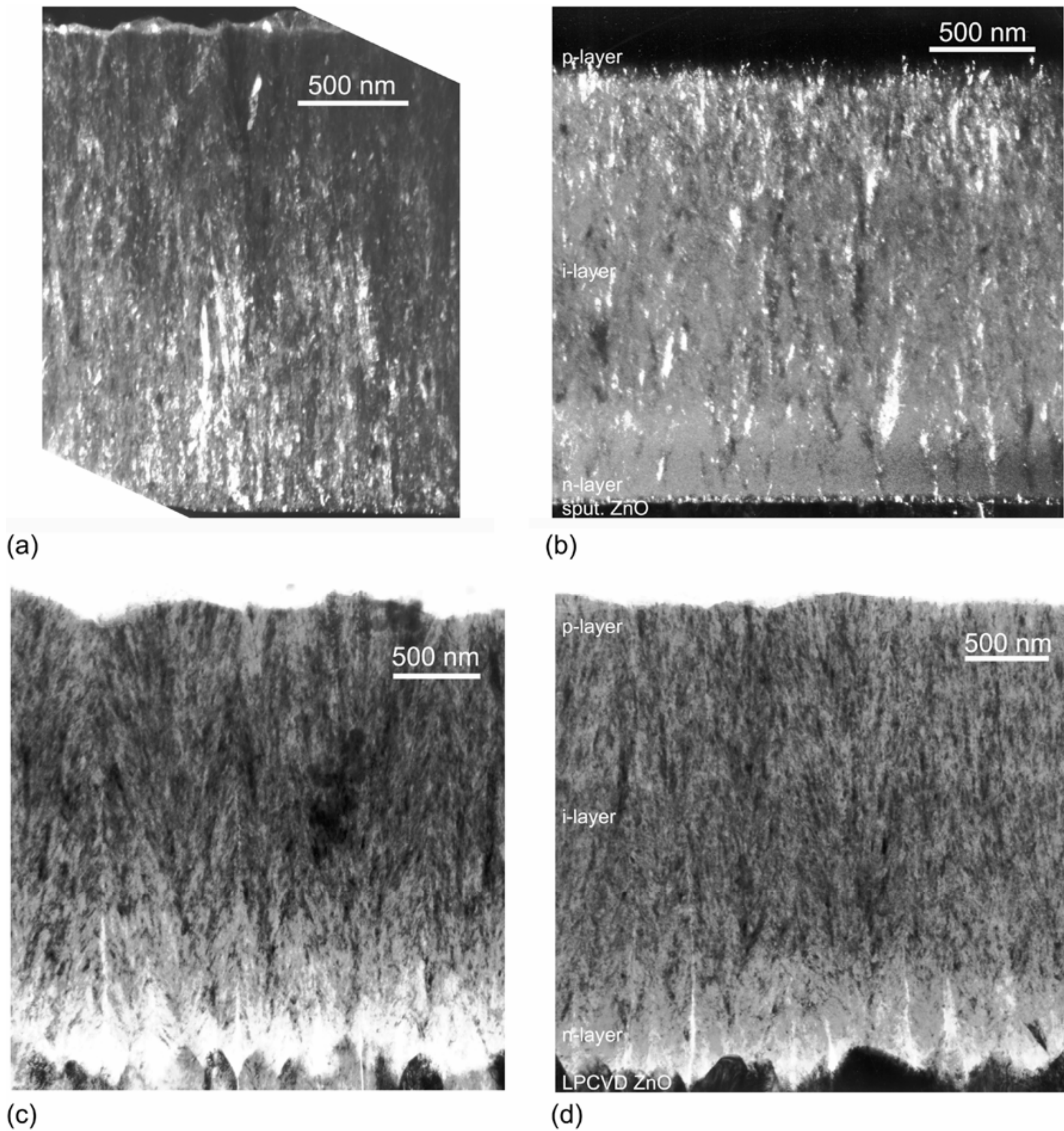

Figure 5.2: a) and b), TEM DF micrographs of cells deposited at SC=5% and 7% on flat sputtered ZnO. The heterophase layer (as defined in 3.4) is barely visible in a) whereas it is much larger in b). In b) the highly microcrystalline n-layer appears as a thin dotty line on top of dark sputtered ZnO. c) and d) TEM BF micrographs of cells deposited at SC=5% and 6.5% on LPCVD ZnO. The amorphous phase in the heterophase layer is visible in d). Note the conical shape of the conglomerates of grains and the enhancement of their lateral size in (c) and (d) compared to (a) and (b), where the nano-crystals remain mostly vertical. AFM scans of the surface of the cells presented in (a) and (c) are shown in Figure 5.1.

The surface topography of cells deposited on top of LPCVD ZnO consists of cauliflower-like grains (see Figure 5.1 (b)). By comparison with the TEM micrograph of the same cell (cf. Figure 5.2 (c)), we conclude that large conglomerates of crystallites emerge at the surface. The lateral size of the conglomerates, as evaluated from the power spectrum of the Fourier transform of the AFM micrograph and in agreement with the micrograph in Figure 5.1 (b), is approximately 1µm, i.e. almost twice as much as that evaluated for microcrystalline material grown on flat sputtered ZnO.
As supported by TEM micrographs (Figure 5.2), the enhanced lateral size of the conglomerates in cells grown on LPCVD ZnO as compared with that of cells grown on flat sputtered ZnO can be explained in terms of competitive growth promoted by the surface roughness of the substrate. The top surface roughness of the series of cells (Figure 5.3) deposited by LPCVD ZnO increases with increasing SC, from values close to those measured for the cells on sputtered ZnO towards the typical value measured for the LPCVD ZnO bare substrate (rms-value of 60nm).

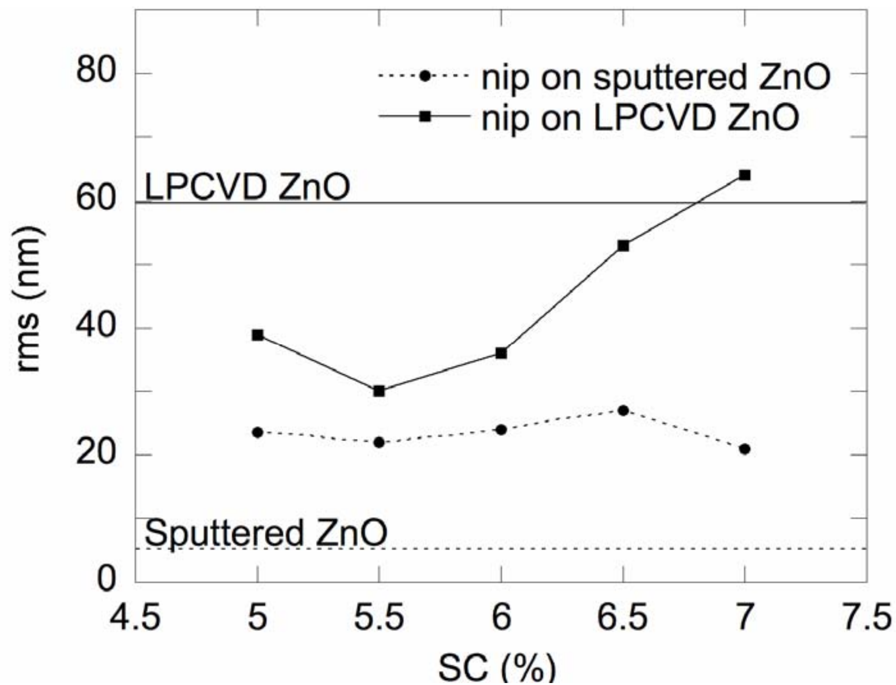

Figure 5.3: Rms roughness measured on the p-layer by AFM on both series of cells. For the cells deposited on sputtered ZnO, the top layer rms roughness is larger than the roughness of the flat substrate (straight line at bottom). On the other hand, the rms roughness of the cells deposited on the rough LPCVD ZnO surface is equal to or smaller than the initial rms roughness of the substrate.

As supported by TEM micrographs (Figure 5.2), the enhanced lateral size of the conglomerates in cells grown on LPCVD ZnO as compared with that of cells grown on flat sputtered ZnO can be explained in terms of competitive growth promoted by the surface roughness of the substrate. The top surface roughness of the series of cells (Figure 5.3) deposited by LPCVD ZnO increases with increasing SC, from values close to those measured for the cells on sputtered ZnO towards the typical value measured for the LPCVD ZnO bare substrate (rms-value of 60nm).

5.3.2. Initial stages of the µc-Si:H growth

A typical TEM micrograph of the initial stages of the i-layer within a nip cell on sputtered ZnO is given in Figure 5.4. At the bottom of the micrograph, the TCO appears dark. It consists of crystallites (average diameter of about 40nm) emerging to the surface with flat and well-defined facets. On top of it, the n-layer appears compact and strongly microcrystalline. Its thickness of about 30nm is constant over the field of observation. On top of the n-layer, the i-layer exhibits a more complicated microstructure. It consists of three phases: the conical conglomerates of nanocrystals (the so-called microcrystalline phase, appearing with the whole black and white contrast on the micrograph), the amorphous phase (appearing uniformly grey on the micrograph) and finally, in some cases, cracks/voids. This mixed phase layer will thereafter be called “heterophase layer”. It is within this layer that the volume fraction of amorphous material is higher than within the rest of the i-layer. Such a heterophase layer has been observed in all the solar cells presented here.

Above the heterophase layer, starting at the coalescence threshold, microcrystalline columns grow up to the top of the solar cell (see Figure 5.2). Note that the medium resolution TEM studies conducted here do not permit quantification of the volume fraction of amorphous material still present above the heterophase layer. We will therefore focus this study on the modifications of the heterophase layer with SC and the substrate type; these are observable modifications of the microstructure of the i-layers in the solar cells presented here.

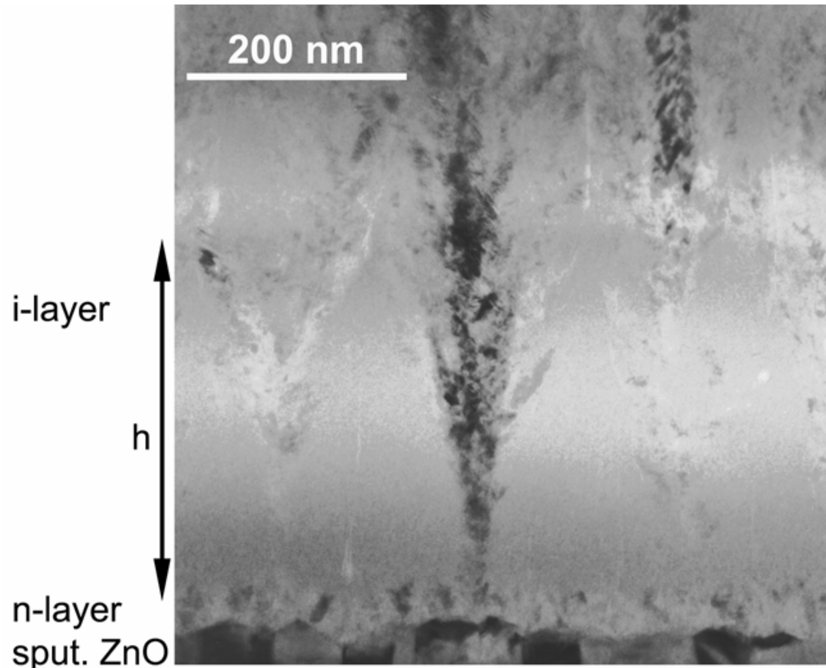

Figure 5.4: TEM bright field micrograph of the first hundreds of nanometers of an nip solar cell. The i-layer was deposited with SC=7% on a highly microcrystalline n-layer on top of sputtered ZnO. The i-layer microcrystalline phase consists of conical conglomerates of nanocrystals, which are embedded in an amorphous matrix. The height at which conglomerates coalesce is defined as the thickness of the heterophase layer h. On this micrograph, the nucleation density n_d is approximately 5µm^{-1}.

With the aim of describing quantitatively the evolution of the microstructure and specifically of the heterophase layer of the material incorporated in the devices, two parameters measured on TEM micrographs will be used in this thesis: the linear nuclei density n_d and the heterophase layer thickness h. The linear nuclei density is the average number of nuclei per micrometer. By definition, the inverse of n_d is the mean distance between two nuclei. The heterophase layer thickness h (nm) is evaluated as the average thickness at which the conglomerates of crystallites coalesce, measured on a vertical line from the top of the n-layer in nip solar cells.

In the series of cells deposited on sputtered ZnO, we can observe that every conglomerate starts growing from the n-layer. Thus, this doped layer plays the role of a nucleation layer. Note that in this series (as in the next series on LPCVD ZnO), no continuous amorphous incubation layer separating the underlying (microcrystalline) doped layer and the microcrystalline i-layer can be observed, as had been previously reported for p-i-n solar cells[5]. High Resolution (HRTEM) observations of the n-i interface indicate that the

i-layer crystallites grow epitaxially on the n-layer grains, in agreement with previous observations[4]. The mean lateral size of the nuclei of the i-layer is of the order of the n-layer thickness (i.e. 30nm) (see Figure 5.4). The gap between the nuclei is filled with amorphous material. As growth proceeds, the conical conglomerates of nanocrystals coalesce and finally result in compact columnar microstructure. The influence of SC on n_d and on h is shown in Figure 5.7 (a) and (b). The decrease of h and increase of n_d are in good agreement with the overall change of crystallinity as observed on XRD spectra (Figure 5.5). What these XRD spectra do not indicate is the location of the amorphous fraction, which is shown by the TEM studies to lie mostly at the bottom of the i-layer. Note that the evaluation of the crystallite size from these XRD indicates that, in both dilution series, the average crystallite size remains within the limited range of 20±4nm.

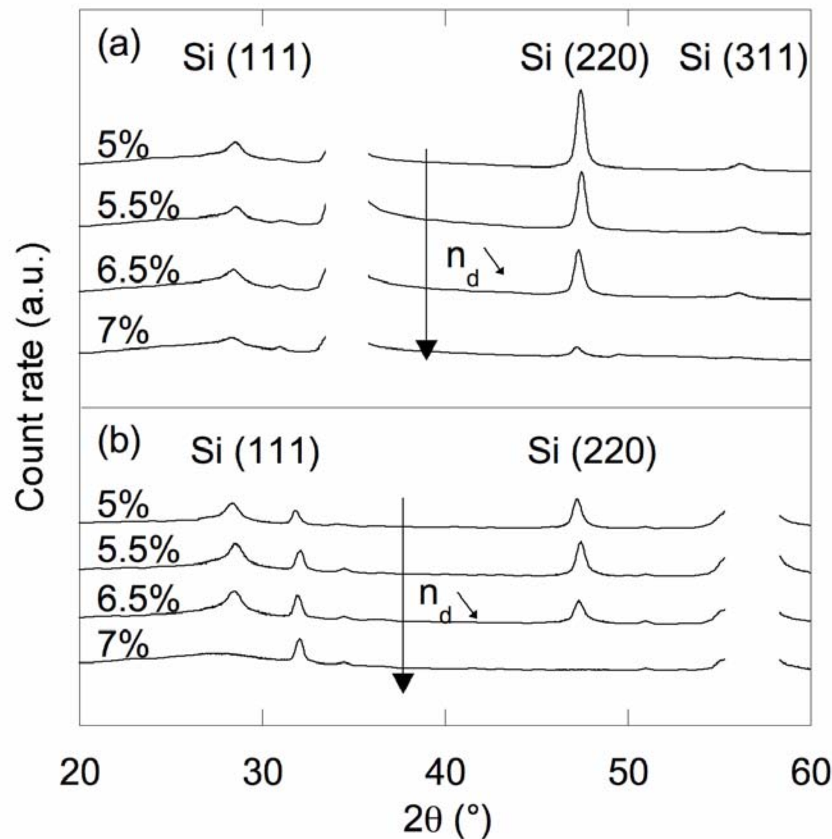

Figure 5.5: (a) Raw XRD spectra of the cells on sputtered ZnO and (b) on LPCVD ZnO. Crystalline volume within the solar cell evolves as the total area under XRD (Si) peaks. The density of nuclei n_d decreases when overall crystallinity decreases.

Turning to the LPCVD ZnO coated glass, this substrate is a rough (rms roughness of about 60nm) substrate whose surface morphology resembles

'Mexican pyramids'. TEM micrographs of the solar cells deposited on this substrate are given in Figure 5.2 (c) and (d). As we could deduce from TEM micrograph of the cell deposited at SC=7% (shown in chapter 3), which is almost completely amorphous (see XRD spectrum in Figure 5.5), the n-layer on LPCVD ZnO is thicker on top of the tetrahedrons than in the valleys in-between and not as compact as on sputtered ZnO. On top of the n-layer, the nucleation of i-layer is not homogenous over the TCO, but occurs preferentially on the upper part of the ZnO tetrahedrons. The lateral dimensions of the crystalline nuclei are of the same size as for cells on sputtered ZnO.
Then the crystallites grow almost perpendicular to the facets of LPCVD ZnO, forming large conglomerates, with lateral dimensions comparable to the lateral sizes of the ZnO tetrahedrons. In the first stage of growth, these conglomerates are surrounded with amorphous material. When the coalescence of the conglomerates occurs, i.e. after 200-350nm of growth (Figure 5.2 (c) and (d)), the heterophase layer ends depending on the height of the ZnO tetrahedrons. This makes the thickness of the heterophase layer h a parameter which is very sensitive to the topography of the TCO. For this reason we prefer to use as a parameter the linear nuclei density n_d, in order to compare the cells grown on TCOs with different topographies. We have plotted in Figure 5.7 the variation of h and n_d versus SC for cells deposited on sputtered ZnO and on LPCVD ZnO.

5.4. Discussion

5.4.1. Microstructure of nip cells

We have sketched the evolution of the microstructure of the i-layer in solar cells deposited on flat sputtered ZnO in Figure 5.6 (a) and (b). These sketches suggest an analogy between the shape of the conglomerates and that of a collection of pencils in a box. Indeed the conglomerates exhibit a cone-shaped end and a cylindrical or columnar body. Within this analogy, the tip of each pencil represents the nucleus of the first grain starting a conglomerate. The other grains then join the first grain and extend it vertically and laterally, forming the cone-shaped end of the conglomerate. The average opening angle of this cone as measured on the whole dilution series is 15±3° (w.r.t. the normal to the substrate). The coalescence threshold corresponds here to the thickness of the heterophase layer h (as there is no incubation layer; see definitions in chapter 3). The analogy of the pencil box holds well for the sample deposited at SC=5% (Figure 5.1 (a)), whereas for the solar cell deposited at SC=7% some competitive growth between the

conglomerates above the heterophase layer can be observed (Figure 5.2 (b)), resulting in non-cylindrical bodies of the pencils.

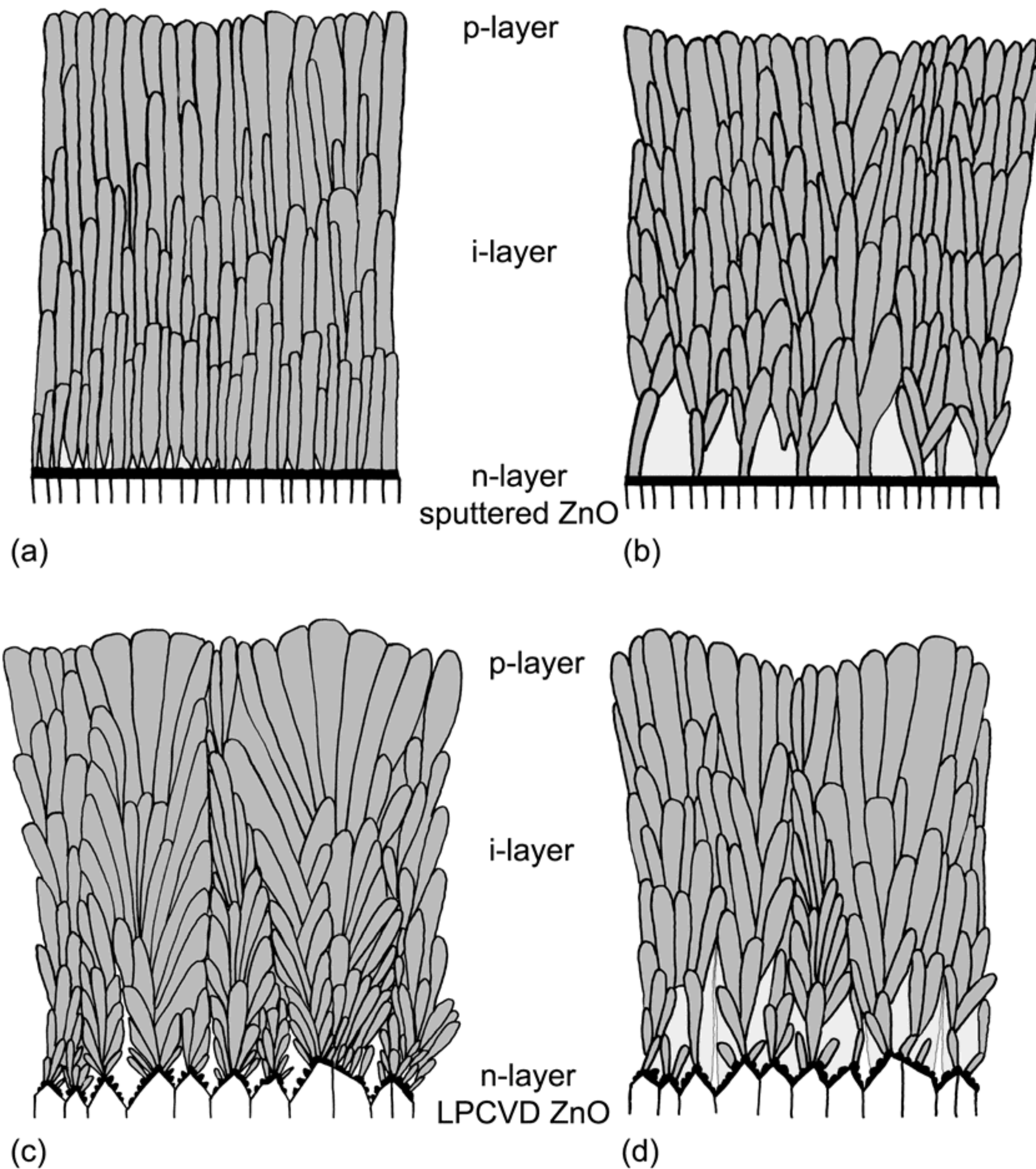

Figure 5.6: Sketches of the microstructure evolution with respect to SC for flat sputtered ZnO and rough LPCVD ZnO. These sketches are drawn from the TEM micrographs given in Figure 5.2. Dark grey regions represent crystalline material whereas light grey regions represent amorphous material. Voids/cracks are represented in white. a) and b), the homogeneously thick n-layer on flat ZnO is represented with a black straight line . c) and d) the n-layer on rough ZnO is no longer homogeneous.

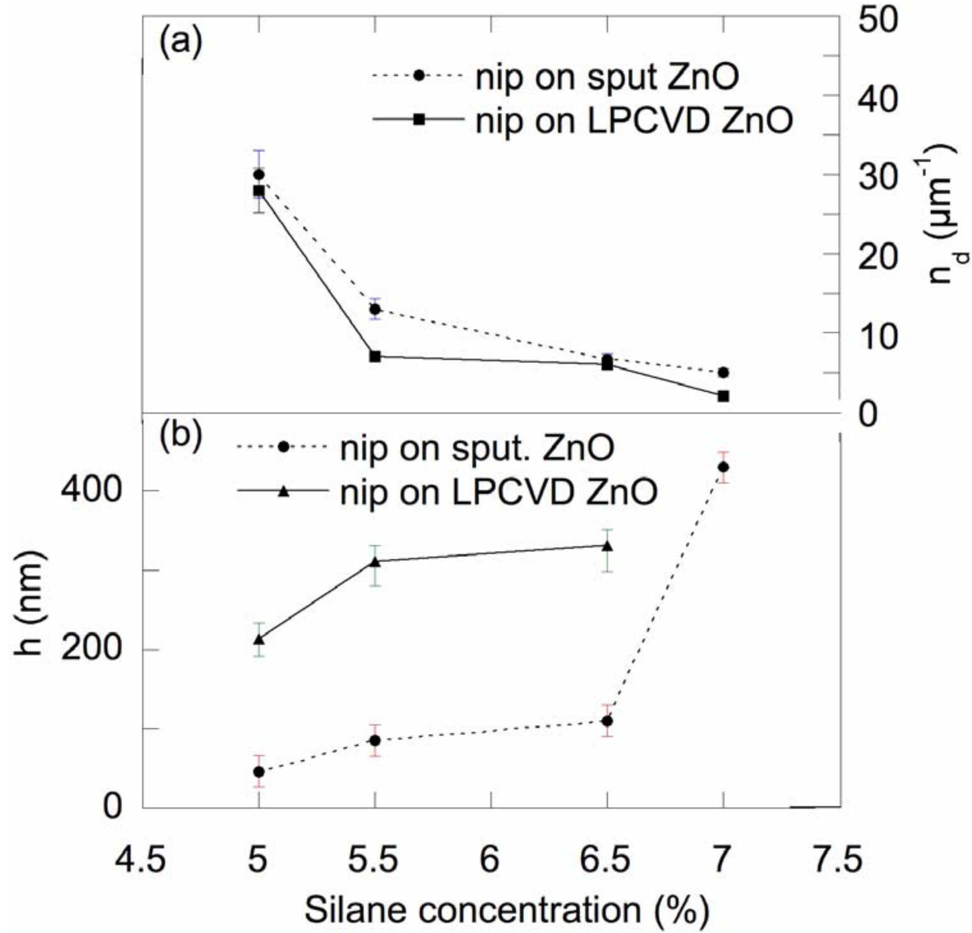

Figure 5.7: : (a) Evolution of the linear nuclei density n_d of the cells on sputtered and LPCVD ZnO as a function of SC. (b) Evolution of the heterophase layer thickness on sputtered ZnO and LPCVD ZnO as a function of SC. Heterophase layer thickness is significantly higher on LPCVD ZnO, as most of the material deposited in the valleys of the TCO is amorphous. Note that both h and nd, on both TCOs, follow the same the trend versus SC.

In Figure 5.7 (a) and (b), the inverse trend between h and n_d can be understood on sputtered ZnO by the observation of an almost constant opening angle α of the cone-shaped beginning of the conglomerates. From basic geometry, one can deduce the following relationship between the heterophase thickness h and the nucleation density n_d:

$$n_d = \frac{1}{2h \cdot tg(\alpha)} \quad (5.1)$$

This simple relationship explains that h and n_d should, indeed, follow an inverse trend. In Figure 5.7, this inverse trend is also observed for cells on LPCVD ZnO.

The linear nuclei density is plotted for both types of substrate. Note that n_d is, within a factor of two, lower on LPCVD ZnO than on sputtered ZnO. In view of the results presented in chapter 4, this difference could be explained by the different crystalline quality of the n-layer.
Another characteristic of the microstructure of devices deposited on rough TCO is the growth direction of the crystallites: they start growing normal to the facet of the LPCVD ZnO tetrahedrons[5, 29]. As growth proceeds, the direction of growth changes towards the normal to the average substrate plane. The ZnO tetrahedrons, thus, promote a starting fan-like growth of the conglomerates (see Figure 5.6 (c) and (d)). This fan-like type of growth is accompanied by competition between the conglomerates, resulting in an increasing lateral size of the conglomerates emerging at the surface during growth. Indeed, as growth proceeds, a conglomerate enhances its lateral size through shadowing other conglomerates by its fan-like growth whereas the lateral sizes of the shadowed conglomerates are reduced progressively to zero. As a consequence, a conglomerate starting on top of a higher-than-average tetrahedron will tend to win the competitive growth over neighboring conglomerates. The result of this process is that the shape of highest tetrahedrons of the substrate are still perceptible on top of the cell, as observed in TEM micrographs in Figure 5.2 (c) and (d). This effect can partly explain the high value of surface roughness for cells deposited on LPCVD ZnO at high SC.

5.4.2. V_{oc} of nip cells

As previously observed, increasing SC towards values close to the transition to amorphous material deposition conditions increases the value of V_{oc}. In this region of the space of deposition parameters, the changes in the microstructure of the i-layer observed in this study, occur mostly in the heterophase layer. It is, thus, of interest to establish a relationship between the microstructural parameter n_d and the value of V_{oc}.
In Figure 5.8, we observe that the behavior of V_{oc} versus n_d exhibit the same trend on both substrates. The V_{oc} established in cells on LPCVD ZnO is lower, however, than the cells on sputtered ZnO; this result could be due to the different nature of the n-doped layer on LPCVD ZnO.

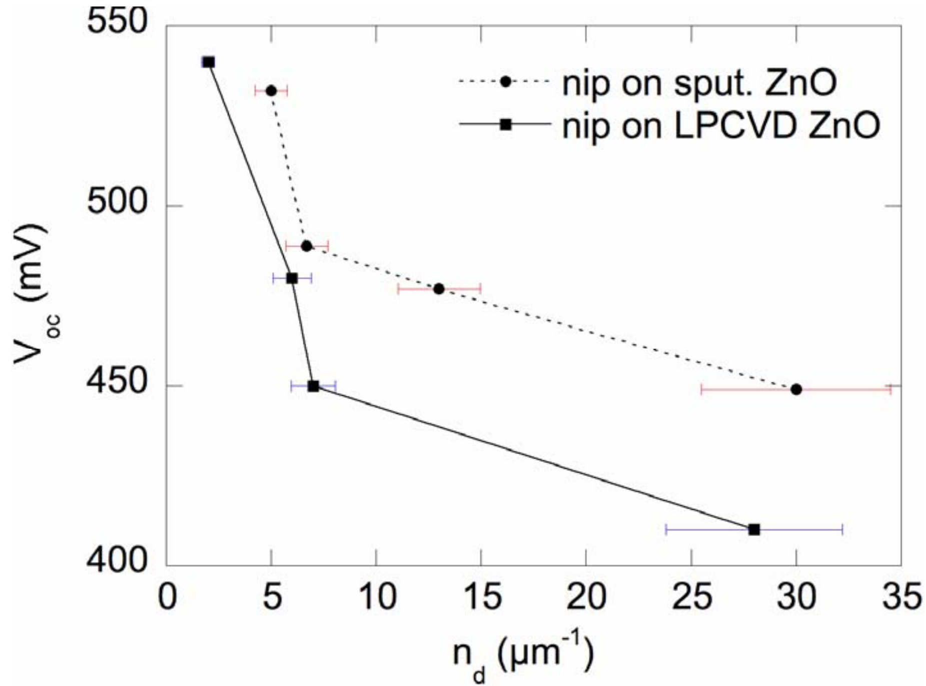

Figure 5.8: : Relationship between the linear density of nuclei n_d and the open-circuit voltage V_{oc} of the cells on sputtered and LPCVD ZnO. Note that n_d is evaluated for the unfolded surface area of the underlying ZnO layer.

It is important to stress that we have not observed here that the amorphous phase simply constitutes a continuous amorphous incubation layer over the n-layer. On the contrary, the amorphous phase is observed to surround the microcrystalline phase, insuring thus the passivation of the crystallite and/or conglomerate boundaries[38].

The lower n_d is, the larger h becomes (see Figure 5.7 (a) and (b)) and, consequently, the larger is the amorphous volume fraction within the device. This effect is more pronounced on the rough substrate, where the valleys are filled with amorphous material and the thickness h of the heterophase layer is therefore increased compared to the case of a flat substrate. Nevertheless we have not been able to quantify here the microstructural changes above the heterophase layer. Before attributing the observed variation of V_{oc} with SC solely to the heterophase layer characteristics (n_d and h) one should also look for any microstructural modifications of the material above the heterophase layer. For this purpose, Raman spectroscopy with green laser was performed[15, 16] on the top layer to observe any change in the microstructure related to SC. The results confirmed that the microstructure changes also in the top of the cell, i.e. the higher is SC, the higher is the amorphous fraction (and so is the V_{oc}). In chapters 8 and 9, the increase of

Voc related to a higher amorphous fraction is explained by the passivation of the conglomerates of crystallites by the amorphous material.

5.5. Conclusions

The detailed investigation of the material microstructure as incorporated in complete working nip devices shows that the SC at which the i-layer is deposited has a major effect on the bottom of the i-layer microstructure, the so-called heterophase layer. Indeed, in these devices, the amorphous volume fraction is higher at the bottom of the i-layer. In particular, the crystalline nuclei density n_d and the heterophase layer thickness h vary notably with SC. Furthermore, the substrate type (here flat sputtered ZnO and rough LPCVD ZnO, both on glass) influences the microstructure of the microcrystalline material: it affects the nature of the n-layer as well as the lateral size of the crystallite conglomerates and the roughness of the last layer of the device (i.e. the p-layer). The latter plays an important role for the light scattering properties of the device.

For both series of nip cells a relationship between the microstructure (specifically the linear nucleation density n_d) and the V_{oc} of the devices has been presented: the lower is the nucleation density, the higher is the resulting value of V_{oc}. As a general consequence, technological control of the first stage of growth of the i-layer (i.e. of the heterophase layer) is of paramount importance to produce cells with a high value of V_{oc}.

It was shown with Raman spectroscopy[15, 16] that the crystallinity of the top layer is also of importance to control the V_{oc}. The overall crystallinity of the i-layer appears thus to be one of the most critical parameters to obtain high-V_{oc} cells. The influence of the amorphous fraction in the i-layer on the properties of the solar cells is studied in chapter 8.

6. Numerical simulation of the growth of µc-Si:H

6.1. Introduction

This chapter is focused on understanding the formation of the different microstructures of µc-Si:H layers observed in the previous chapters. A better understanding of the growth dynamics is necessary for the optimization of the devices based on that material such as solar cells and thin film transistors (TFT).

The growth dynamics is studied in-situ, by real-time spectroscopic ellipsometry (RTSE)[30, 32] or ex-situ by the characterization of the surface topography (by AFM or SEM) of a series of samples of increasing thicknesses[39]. Both techniques permit to study the surface roughness evolution with respect to the accumulated layer thickness.

Discrete numerical simulations were used here to understand what are the fundamental mechanisms leading to the observed growth dynamics of µc-Si:H[40]. The suspected growth mechanisms are therefore translated into a computer language: they are, then, called the selection rules. Their effects on the resulting microstructure can be directly observed on the computer screen through the visual representation of the microstructure.

In the framework of statistical physics at equilibrium, a phase space and a Hamiltonian (energy function) usually give the definition of a model. What is called here “selection rule” is derived from the Hamiltonian and a defined set of possible transitions between pairs of configuration states. Then, the probability of transition from an initial configuration to another is evaluated by taking into account the Boltzmann factor, which is related to the energy difference between the final and initial states. This must be done carefully by satisfying some detailed balance equations; otherwise the equilibrium condition would be violated.

However the experimental systems we are dealing with (growth in PECVD processes) are far from equilibrium. Consequently, the selection rules are directly defined instead of being derived from an energy function. Of course at the end of such a study, it could be of interest to find out which Hamiltonian is compatible with the chosen selection rules.

The discrete dynamical model proposed here is based on simple selection rules and intuitive simulation parameters. Similar models have been successfully applied to the description of a variety of growth phenomena, from those involved in molecular beam epitaxy (MBE) to those occuring in the growth of bacterial colonies[41]. To give a more recent example, in very large scale integration (VLSI), where metallic films are deposited on top of

high aspect ratio structures, a 3D dynamical discrete growth model was introduced by Smy[42], which allows for prediction of the surface evolution and microstructure of metallic films.
The model presented here allows for the prediction of the surface morphology and microstructure of amorphous and microcrystalline silicon. It is able to reproduce the surface evolution of μc-Si:H with respect to layer thickness, the amorphous to microcrystalline phase transition as well as the conically shaped crystalline domains.
The model is focused on capturing the essential growth mechanisms leading to the microstructure experimentally observed. Therefore the aim was to find as few selection rules as possible in order to simulate the microstructure and growth dynamics of μc-Si:H. It uses, thus, two simple selection rules that are applied after deposition and local relaxation of particle:

- First rule: a crystallographic orientation is attributed to the particle in such a way that the incoming particle tends to be in the same crystallographic orientation as its neighbors. This self-organization process is responsible for the growth of conically shaped crystalline domains, similar to those observed in μc-Si:H
- The second selection rule allows for the removal of deposited particle (desorption). It is implemented in such a way as to preferentially remove the particles belonging to the amorphous phase.

Two of the three model parameters are related to the material properties: the number of states *n* used to describe the different crystallographic orientations of the incorporated particles and the minimum amount of same-state neighbors *t* needed to 'convince' the newly deposited particle to take their state. The *t* parameter can be viewed as a critical size of the nuclei expressed as a minimum number of particles.
A phase diagram of the model, i.e. the crystalline fraction of the simulated layer as a function of the *n* and *t* parameters was produced in order to reveal the model behavior. It is shown that the *n* and *t* parameters can induce phase transition. However, both of these parameters are related to the material properties and not to deposition conditions. A third parameter, *d*, is therefore introduced in order to vary the probability of desorption of an incoming particle. It is shown here that the presence of preferential etching of the amorphous material is sufficient to explain the sudden surface roughness increase at nucleation, the layer roughness evolution with respect to the accumulated thickness and the surface morphology of the layers.

6.2. *Simulation and experimental*

The Monte-Carlo discrete simulations can be carried out in a 3D cubic lattice of dimensions up to 512x512x512 lattice sites on substrates that are either flat or rough. In the largest cubic lattice (512^3 lattice sites), it takes up to 20 minutes to complete simulations on a Mac G4 computer (1cpu at 466Mhz) with 768MB of RAM. The simulation software was programmed in Objective-C with standard libraries freely available for MacOSX. The images of the simulated layers were rendered with the standard OpenGL libraries (open domain library), an industry standard for computer graphics.

6.2.1. Model description

Random deposition and relaxation

A particle is released from a position randomly chosen above the surface. The particle follows a vertical trajectory in a cubic lattice until it reaches the growing surface whereupon it stops. The particle then moves to the lowest site within the first and second nearest neighbors where it sticks.

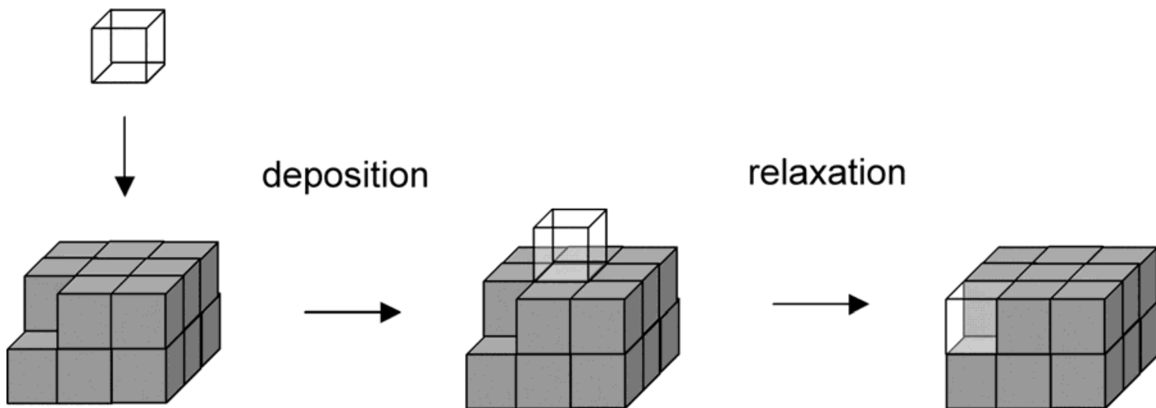

Figure 6.1: Vertical random deposition followed by local relaxation of the incoming particle (transparent particle).

Incorporation into the material

The deposited particle is given a state among *n* possible states with the following selection rule:

- The most represented state among the neighbors called thereafter the dominant state is evaluated. The neighborhood taken into account for this calculation extends over the 25 nearest neighbors, i.e. the 9 neighbors below, the 8 neighbors around and the 8 neighbors above the selected site.
- If the number of particles in the dominant state is strictly higher than the critical size of the nuclei *t*, the particle's state is given the

value of the dominant state, otherwise its state is randomly set to one of the n possible states. The critical size of nuclei *t* is a model parameter comprised between 0 and 25 (25 being the maximum number of neighbors in this case).

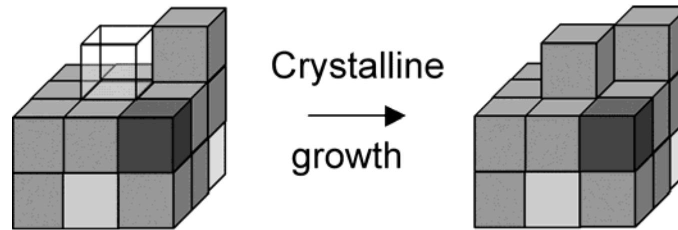

Figure 6.2: Case of crystalline growth for, e.g. t=6. The dominant state in the neighborhood is represented by the mid-grey color (9 neighbors are of that color). As 9 is higher than the threshold t=6, the newly deposited particle (the transparent particle) takes the mid-grey color.

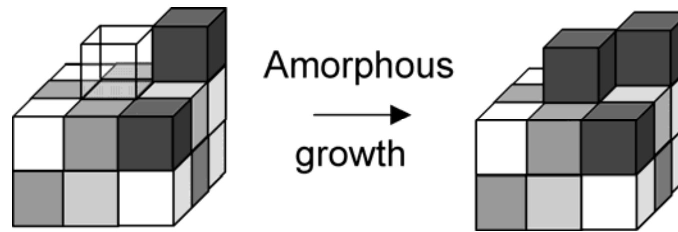

Figure 6.3: Case of amorphous growth for, e.g. t=6. The dominant state in the neighborhood is represented by the mid-grey color (4 neighbors are of that color). As 4 is smaller than the threshold t=6, the newly deposited particle (the transparent particle) takes a randomly chosen color.

Desorption

This process is entered with a probability *d*. It is implemented according to the following rule: the particle is immediately removed after deposition, with a probability given by the number of neighbors in a different state than the particle's attributed state divided by the total number of neighbors. Thus, if all the neighbors are in a different state (amorphous phase), the newly deposited particle will be removed, whereas the removal of a particle surrounded by same color neighbors only (crystalline phase) never occurs.

After the selection rules have been applied, a new particle is deposited, until the set layer thickness is reached.

Substrate
The particles impinging on the substrate cannot take the value of the state representing the substrate. Note that the substrate sites are not counted as neighbors when the selection rules are applied to the incoming particle; this fact promotes the growth of amorphous material at the initial stage of growth.
Boundary conditions
A lattice site situated at the edge of the substrate has not the same number of neighbors as a site situated e.g. in the middle of the substrate. To avoid growth artefacts due to that issue, periodic boundary conditions have been chosen, i.e. the neighbors of the sites at an edge of the substrate are the sites at the opposite edge. The same conditions apply to the sites situated at the corner of the substrate.

6.2.2. Model Interpretation

Crystallographic orientations
In this computer simulation, a state (or a crystallographic orientation) is represented by a color. A microcrystalline region is thus defined as a domain of the cubic lattice filled with particles of the same color. On the other hand, an amorphous region is a domain filled with randomly varying colors.
The particle state represents its crystallographic orientation, meaningful only if one considers its position relative to its neighbors.
In a real material, a grain boundary is defined as a region over which the crystallographic misorientation α between two grains exceeds several degrees. Depending on this value, polycrystalline material will be reproduced by a finite number of possible crystalline orientations. The latter can be calculated as follows: considering the ratio between the solid angle of the cone Ω with an aperture $\alpha/2$ and the unit sphere surface A, one obtains:

$$n = \frac{1}{8} \cdot \frac{A}{\Omega} = \frac{1}{4 \cdot \left(1 - \cos\frac{\alpha}{2}\right)} \quad (6.1)$$

where the factor 1/8 takes into account the symmetries of the cubic lattice. For $\alpha \leq 24°$, one obtains approximately $n \geq 11$ states, which corresponds to values of n used for the simulations presented here (see the figure captions for the exact parameters of each simulation).
Particle
The particle incorporated into the material represents the average behavior of many atoms (typically, several hundreds). It is important to notice that although a particle as incorporated in the material represents an average

behavior of a large number of atoms, the simulation does not simulate the deposition of clusters of atoms[42].

6.2.3. Growth experiments and Measurements

In this study a microcrystalline layer was deposited by PECVD on a rough substrate for comparison of the microstructure with the one generated by computer simulation. The approximately 400 nm thick i-layer was deposited at a silane gas phase concentration close to the a-Si:H/μc-Si:H transition. The underlying substrate material is a sodium-free AF-45 glass substrate coated with ZnO deposited by LPCVD.

An AFM height scan (scan range of 1 μm, 512 x 512 measurement points) of the substrate (LPCVD ZnO layer) has been used to create a discrete height map to simulate the substrate.

TEM observations allowed us to observe directly the microstructure of the layers, the morphology of the growing surface as well as the distribution of the amorphous material within the layer.

6.3. Results and discussion

6.3.1. Microstructure

The simulated microstructure and TEM micrograph of a real layer on rough and flat substrates are presented in Figure 6.4 and Figure 6.5, respectively. The simulated microstructure qualitatively shows the most important features of the comparison layer. Indeed, it exhibits an amorphous incubation layer followed by a mixed-phase layer, the so-called "heterophase" layer, where μc-Si:H grains extend laterally to the detriment of the amorphous phase; then the conical grains coalesce above the heterophase layer and, afterwards, the microstructure consists of microcrystalline columns that compete for lateral growth. The behavior of rms-roughness with respect to thickness evolution of the layer[32, 39] is also well reproduced by the model (Figure 6.5): once the nucleation occurs within the amorphous material, roughness increases as long as the coalescence threshold is not reached; thereafter, coalescence roughness decreases and finally stabilizes.

When the desorption process probability d is varied, one observes in Figure 6.7 that the material structure changes from fully amorphous (d=0) to crystalline (d=1). If a higher value of d is assumed in the simulation, nucleation occurs at a lower height within the layer, as one indeed observes in real material[6, 39].

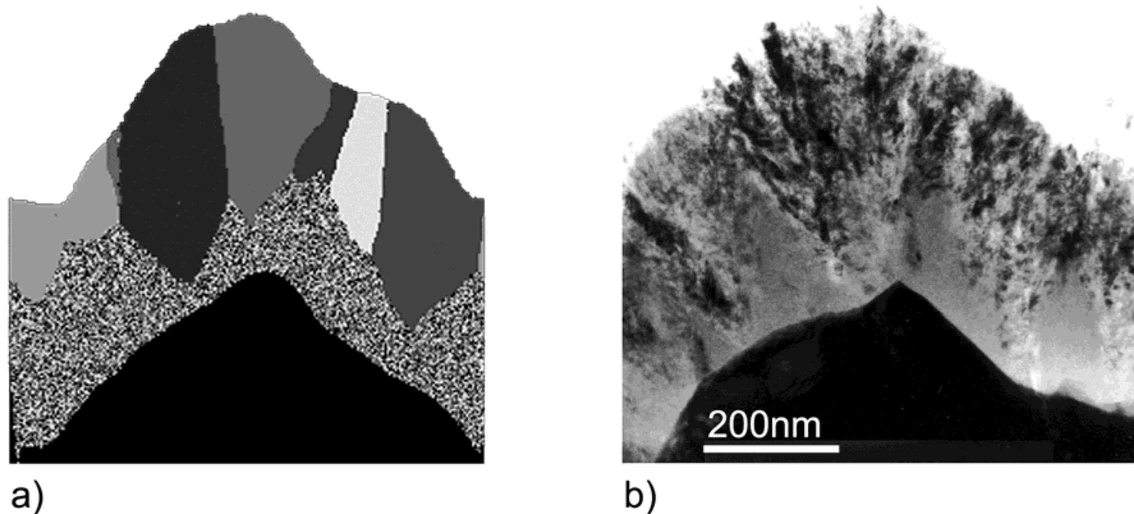

Figure 6.4: a) Simulation with n=22, t=5 and d=0.4 on a rough substrate. b) Bright field TEM micrograph of a μc-Si:H layer deposited on rough LPCVD ZnO. The main features of the microstructure of μc-Si:H can be observed on the simulation: amorphous incubation layer, heterophase layer and conically shaped microcrystalline domains.

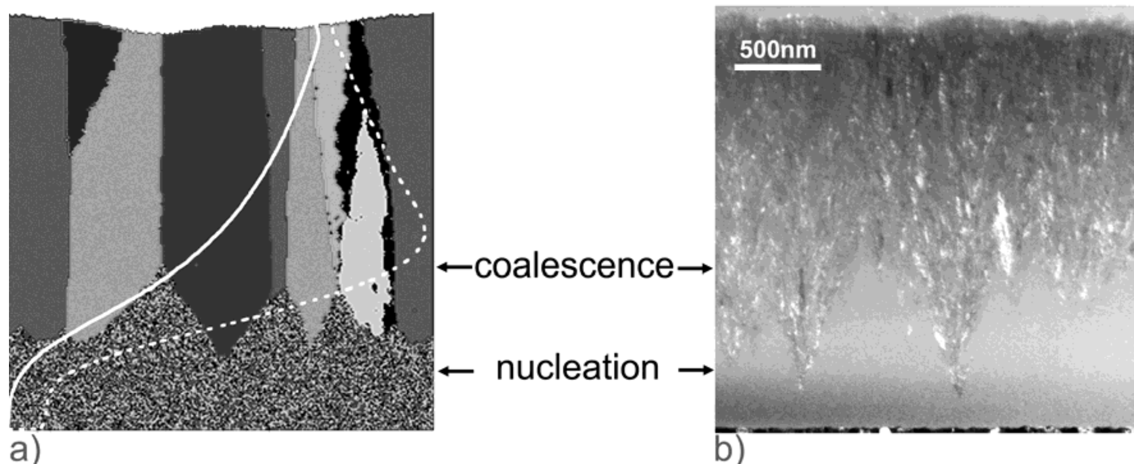

Figure 6.5: a) Simulated layer (n=22, t=5, d=0.4) and b) bright field TEM micrograph of a microcrystalline layer. On the simulated layer cross-section, the crystalline fraction and the rms-roughness (x-axis) versus the layer thickness (y-axis) are superimposed in plain and dotted line, respectively. The full scale is given by the picture width, i.e. a scalar from 0 to 1 for the crystalline fraction and a number of lattice sites from 0 to 6 for the rms-roughness. The simulation was carried out in a 256x256x256 lattice.

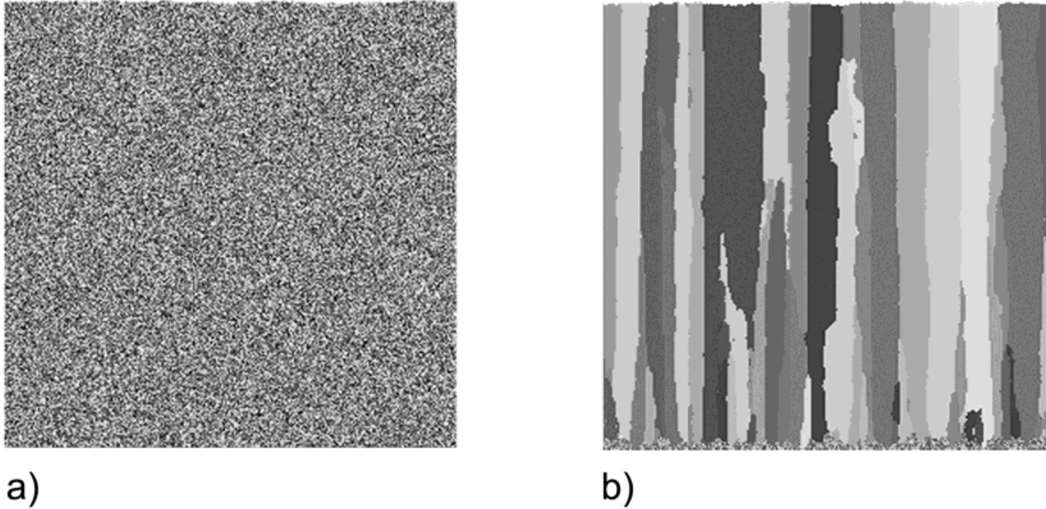

Figure 6.6: a) Fully amorphous layer (n=30, t=12, d=0) and b) fully microcrystalline layer (n=30, t=3, d=0). Note that a small amorphous fraction still exists at the bottom of the layer (2% of amorphous fraction). In the absence of desorption (d=0), the surface roughness is almost flat for both simulated layers.

6.3.2. Phase diagram of the model

In order to understand the influence of the two fundamental parameters n and t of the model on the simulated microstructure, the crystalline fraction as a function of n and t was computed without desorption (d=0), see Figure 6.7. A particle incorporated in the material is considered as part of the crystalline phase, if 5 or more neighbors are in the same state as its own state. Consequently, the microstructure simulated with $n<5$ are generally crystalline for any values of t and this region of the phase diagram is not relevant for the understanding of growth. In Figure 6.7, it is observed that for $t<4$ and for any values of n, the layer grows crystalline as well. This regime, i.e. small critical size of the nuclei, could thus be used for the simulation of metallic layers, which are generally crystalline.

On the other hand silicon grown by PECVD is amorphous, microcrystalline or both, depending on the deposition conditions. As the simulation parameters n and t introduced so far are related to the material properties, i.e. to the description of the crystallographic orientations and to the critical size of nuclei, respectively, they cannot be changed when simulating the growth of one single material such as silicon.

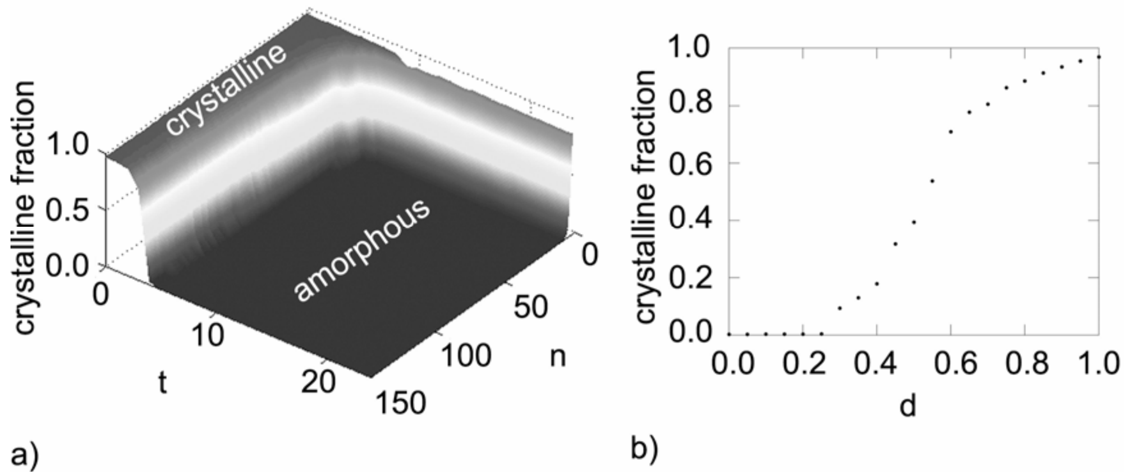

Figure 6.7: a) Phase diagram of the model. The transition between the amorphous and crystalline phase is highlighted. The simulations were carried out in a lattice of 128x128x128 sites. b) Phase transition from amorphous to crystalline as a function of the desorption process probability d, for layers simulated with n=12 and t=6 in a lattice of 256x256x256 sites.

Thus, a third parameter, related this time to the deposition conditions must be included. The desorption process probability d is introduced to vary the probability that a particle desorbs from the growing surface. This desorption process is implemented in such a way that it etches away the amorphous phase preferentially. This mechanism corresponds to the growth model proposed by Tsai et al [43] for a-Si:H and μc-Si:H deposited by PECVD where the preferential etching of the amorphous material by atomic hydrogen promotes the growth of μc-Si:H (Note that there does not exist full agreement among experimentalist on this concept[44]). The simulation parameter d is therefore related to the deposition conditions and specifically to the ratio of hydrogen to silane in the gas phase mixture used for the layer deposition. When etching is seldom (low hydrogen to silane ratio), the material grows amorphous whereas when the etching is high (high hydrogen to silane ratio), the material grows microcrystalline. In order to accurately render the growth of silicon by PECVD, one must use pairs of n and t parameters ensuring that the following two conditions are fulfilled:
1) Without any etching ($d=0$), the material should be fully amorphous.
2) With a high preferential etching probability ($d=1$), the material should be close to fully microcrystalline.
The first condition is fulfilled with all points of the phase diagram except the two regions defined by $n<5$ and $t<4$ for which the crystalline fraction is high

even without any etching. Note that (as mentioned above) the number of states used for representing the different crystallographic orientations must be greater than or equal to 11.

The second condition is more difficult to fulfill: the etching process, as implemented in the model, is not efficient enough to force the nucleation when both n and t are high, e.g. $n>100$ and $t>12$. Thus, for reasonable model parameter values ($n<100$ and $t<8$), the etching procedure is able to reproduce the amorphous to crystalline transition when d is varied from 0 to 1.

The model is not critically dependent on the value of the n and t parameters, i.e. there are many pairs of values that could be used to describe accurately the observed growth dynamics and microstructure of the mixed phase amorphous and microcrystalline silicon.

6.3.3. Phase transition versus desorption probability

When the desorption process probability d is raised, one observes in Fig. 1.b) that for a given n and t pair of parameters the material structure changes from fully amorphous ($d=0$) to crystalline ($d=1$). The higher the value of d in the simulation, the thinner is the thickness of the amorphous incubation layer; note that, for real layers, a similar behavior of the thickness of the amorphous incubation layer with respect to the hydrogen to silane gas flux ratio was experimentally observed[6, 39].

6.3.4. Growth dynamics

The behavior of rms-roughness with respect to thickness evolution of the layer[32, 39] is also well reproduced by the model and specifically, the roughness increase that coincides with the nucleation (Figure 6.5). For this specific growth feature to occur the preferential etching of the amorphous phase is required. After nucleation, the roughness increases as long as the coalescence threshold is not reached; after the coalescence roughness decreases and, finally, stabilizes.

It is important to stress that in this model, the surface roughness evolution versus the accumulated film thickness (which is in very good agreement with the observations by RTSE on microcrystalline layers[32]) is only due to the preferential etching of the amorphous material.

6.3.5. Further work

The model, as proposed, describes qualitatively the main features of the growth dynamics and microstructure. However, further improvements of the

model will lead to a tool that could predict the layer microstructure and surface morphology in a more quantitative way.
In order to reproduce cracks and voids experimentally observed with TEM, oblique trajectory and lateral sticking of the particles on the growing surface should be implemented.
Since we have studied a model where only local relaxation was permitted, it is interesting to wonder whether the basic morphological features are sensitive to some equilibration processes. A preliminary study shows that introducing diffusion on the growing surface would destroy the conical shapes of crystalline domains. This observation is relevant for the actual study of μc-Si:H thin films. Indeed the relevance of surface diffusion is still a debated topic in the literature.
In order to develop a more realistic model reproducing microcrystalline domains composed of several sub-grains, the microscopic order parameter (the discrete state representing the n possible crystallographic orientations) was replaced by the unit sphere. In this case, the crystallographic orientations are represented by a unit vector and the selection rules are re-adapted to that case (see caption of Figure 6.8). An example of the resulting simulated microstructure is shown in Figure 6.8. We have, thus, favored the growth of domains, not only with the same orientation as the one of the neighborhood but also with orientations slightly different (represented by slightly different grey levels).

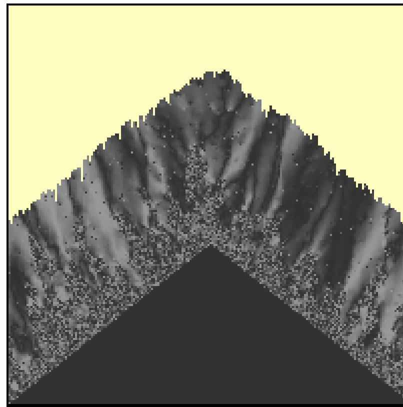

Figure 6.8: Microstructure resulting from a model defined on a 3D cubic lattice where the microscopic order parameter is the unit sphere. Here, the vector (representing the crystallographic orientation) attributed to the incident particle is determined by the average of the unit vectors of the neighborhood. When this average vector has a norm greater than 0.3 (threshold value), its crystallographic orientation is set to the normalized average vector. Otherwise it is chosen randomly.

6.4. Conclusions

A 3D dynamical model of the growth of μc-Si:H and amorphous silicon is presented. It is based on simple selection rules and intuitive simulation parameters.

Despite its apparent simplicity, the model is able to reproduce the main growth and microstructure features of μc-Si:H:

- Conical shape of conglomerates;
- Amorphous to crystalline transition (w.r.t film thickness and desorption);
- Surface roughness evolution.

For a chosen set of (n, t) parameters an increase of the desorption probability from 0 to 1 leads to a transition from amorphous to microcrystalline with all the microstructure features observed in series of samples obtained by increasing the hydrogen to silane flux ratio.

The preferential etching of the disordered material, as implemented in the simulation, is observed to be responsible for the surface roughness evolution.

7. Evaluation of i-layer quality by FTPS

7.1. Introduction

7.1.1. i-layer quality versus deposition conditions

In chapters 3 and 4, the effect of the substrate on the nucleation and growth of microcrystalline silicon was demonstrated. It was concluded that extreme care should be taken when one makes assumptions on the microstructure of an i-layer incorporated in the solar cell, from observations made on an i-layer grown under the same conditions on another substrate (e.g. glass). Indeed, two layers, deposited simultaneously, on different substrates are likely to exhibit different microstructures and different electro-optical characteristics. It is, thus, important to utilize characterization techniques that allow precise monitoring of the properties of the layers as incorporated within the working device. In this chapter the quality of the active layer of complete pin and nip microcrystalline silicon solar cells is investigated with the help of sub band-gap absorption spectroscopy.

In many research groups, SC used for the deposition of the i-layer is a parameter used to optimize the electrical performance of the solar cell[7, 11, 37]. Besides affecting the performance, SC influences in a major way the i-layer microstructure, as observed with TEM and Raman spectroscopy[4, 6, 36]. In the present chapter, the changes of the optical properties of the active layer with respect to SC are investigated.

7.1.2. Sub-gap absorption spectroscopy applied to complete cell

Sub band-gap absorption spectra are commonly measured with very sensitive techniques like PDS and CPM. In addition to the measurement of the optical band-gap, the absorption spectrum yields two important parameters related to the disorder and the defect density of the probed material.

In the region just below the gap (1.12eV for µc-Si:H and 1.75eV for a-Si:H), the absorption coefficient (and the FTPS spectrum) stems from optical transitions involving band tail states. The spectrum in that region increases exponentially with the photon energy, forming the so-called Urbach tail. It is characterized with the exponential slope E_0 of the absorption spectrum. It is determined by fitting the absorption curve using the following formula:

$$\alpha = \alpha_0 \cdot e^{E/E_0} \quad (7.1)$$

where α_0 is the exponential pre-factor.

In amorphous silicon the Urbach tail roughly extends from 1.5 to 1.7eV and its slope is characterized by an Urbach parameter E_0 having a value between 40 and 60meV. E_0 can be related to the material disorder[24]. It depends generally on the temperature, however, in the case of amorphous material, the disorder is mostly static and relates to strained bounds. Note that the Urbach tail also exists in monocrystalline silicon (a typical value of 9.6meV was reported[45] for room temperature measurements).
The defect density is estimated from the value of the absorption coefficient at a photon energy of 0.8eV for µc-Si:H silicon ($\alpha_{0.8eV}$) and 1.2eV for amorphous silicon ($\alpha_{1.2eV}$).

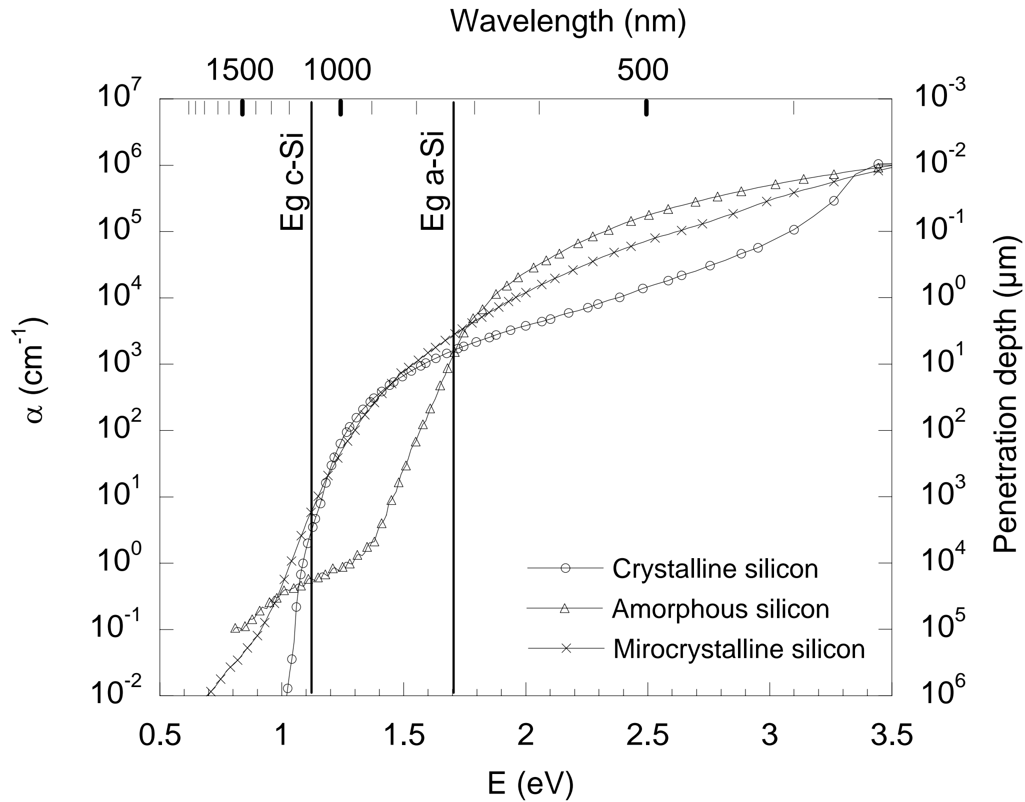

Figure 7.1: Absorption spectra of microcrystalline, amorphous and crystalline silicon measured by CPM reproduced from ref. [13]. The penetration depth, i.e. the inverse of the absorption coefficient α, is plotted on the right axis.

PDS and CPM are time consuming techniques. Besides this common disadvantage, the PDS method cannot be used for the evaluation of the sub band-gap absorption in complete solar cells. Indeed, from a photon energy of 1.6eV and below, PDS measures the free carrier absorption of the TCO, which is several orders of magnitude larger than the absorption of silicon in that spectral region. The Urbach parameter E_0 and the defect related

absorption thus can not be measured (Figure 7.1) by PDS in a complete solar cell configuration.
On the other hand, CPM allows the measurement in complete cells, as it is based only on the number of photons required for each photon energy to keep the photocurrent constant. Because the photocurrent is generated in the i-layer only, CPM can be used to monitor the electronic properties of the i-layer within a complete solar cell. The sensitivity of this technique in the spectral region of very low absorption (around or below 0.8eV) is technically limited, however, and the regulation step at each photon energy value is time consuming.

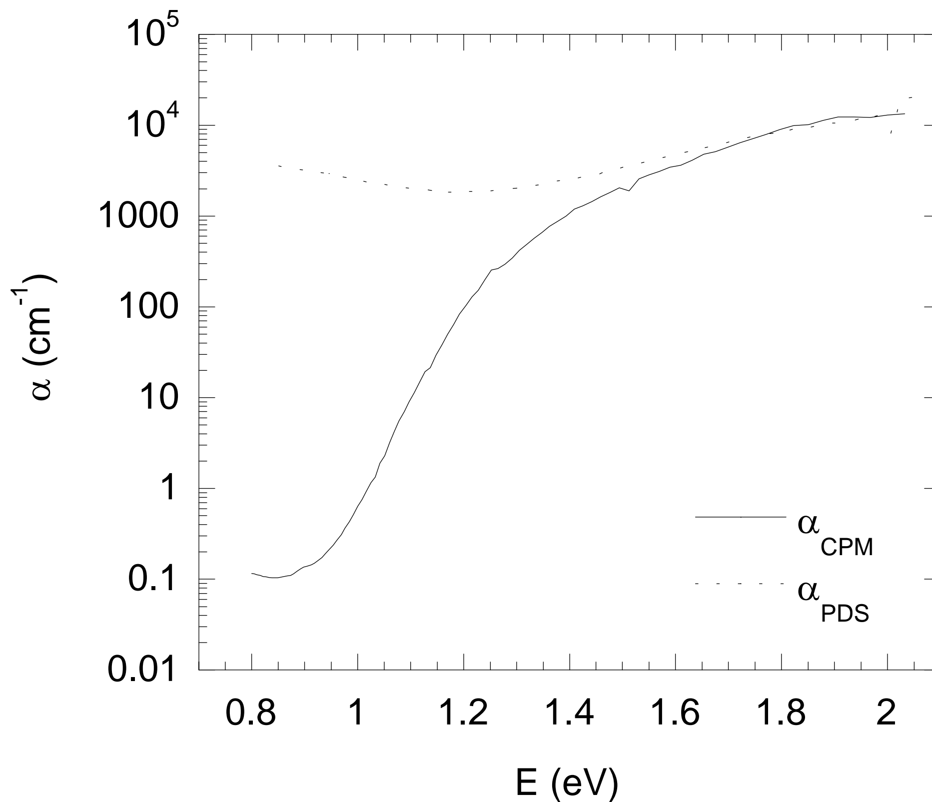

Figure 7.2: Comparison of absorption coefficient α of a pin μc-Si:H solar cell measured by PDS and CPM. Below 1.6eV, the PDS curve is dominated by the absorption of the free carriers in the TCO. This is the reason why CPM can only be used in a complete solar cell.

In order to use the absorption spectroscopy routinely to monitor the quality of the i-layer in working devices, M. Vanecek et al. developed a fast and sensitive technique based on Fourier-transform infrared (FTIR) spectroscopy[17, 18]. This new technique, named Fourier-transform

photocurrent spectroscopy (FTPS) is introduced in the following section. FTPS provides measurements of the absorbance spectrum of silicon-based thin-films over 6 orders of magnitude, in the sub band-gap region as well as above it.

7.1.3. Main results

To demonstrate that the FTPS allows the measurement of defect related absorption, artificial defects were created by proton irradiation of the solar cells at centre d'analyse par faisceau ionique (CAFI) in le Locle (CH). The electrical characteristics of the cells were notably altered by that treatment. Successive thermal annealing and FTPS measurements, measured in the group of M. Vanecek, evidenced that the defect related absorption decreases after each annealing step. This shows the ability of FTPS to provide valuable data on the electronic quality of the i-layer incorporated within a solar cell.
The effect of SC on the defect related absorption was also a matter of interest. Two SC series of μc-Si:H solar cells in pin and nip configurations were fabricated. The FTPS spectra were measured on several individual solar cells for each SC of the two series of samples, thus, permitting to monitoring of the spatial homogeneity of the electronic quality of the cells. The evolution of the defect related absorption and the Urbach tail slope of the active layers with respect to SC are presented here. The defect related absorption decreases significantly when SC is raised whereas the E_0 parameter only slightly decreases (as long as the microcrystalline to amorphous transition is not reached).
It is also reported here that the FTPS spectra can be used to qualitatively infer the crystalline volume fraction within the active layer of the cells.

7.2. Experimental

7.2.1. Principles of FTPS

Set-up description

Figure 7.3 represents the set-up of the FTPS measurement. For a description of the FTIR spectroscopy principles consult for example ref. [46]. Inside the FTIR spectrometer (not shown here), the beam from a light source (either halogen lamp or glow-bar) is directed through a variable aperture. Then, it enters a Michelson interferometer equipped with one fixed and one movable mirror that constantly moves back and forth along a rail at speed v. The position of the movable mirror is recorded by counting the number of interference fringes from of a helium-neon laser beam that follows the same path as the main beam in the interferometer. The main beam is re-composed

with a beam splitter and externally focused on the sample. The sample works here as a detector, either in a coplanar contact configuration (photoconductive mode) or transverse configuration (photovoltaic mode). A voltage bias is applied between the contacts, in order to extract the photocurrent or to bias the solar cell. The photocurrent is then pre-amplified and sent back to the spectrometer through an A/D converter.

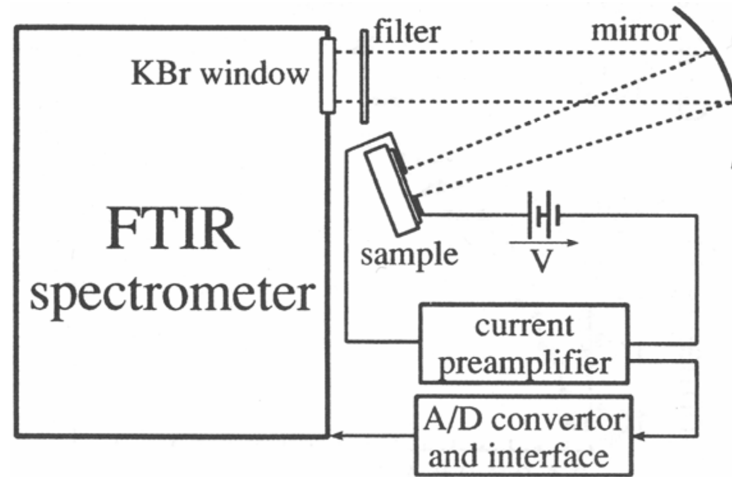

Figure 7.3: Set-up of the FTPS measurement, reproduced from [18].

Working principle

The spectrometer records the sample photocurrent I(x) as a function of the position of the movable mirror x. At each mirror position x, there are harmonics composing the main beam spectrum for which constructive or destructive interferences occur; these harmonics contribute thus more or less to the I(x) signal, respectively. I(x) is therefore referred to as an interferogram. The fast Fourier-transform (FFT) of the interferogram is computed to obtain its different harmonics of spatial frequencies υ (cm^{-1}) and respective amplitudes A(υ). The absorbance of the sample for the corresponding wavelength $\lambda=1/\upsilon$ is proportional to A(υ). In order to obtain the FTPS spectrum, A(υ) must be normalized, i.e. it must be divided by the baseline. The latter requirement involves the measurement of the main beam intensity spectrum with the help of a spectrally independent reference detector (the internal detector of the spectrometer).

Corrections to FTPS signal

The FTPS spectrum then must be corrected for the different frequency responses of the two different detectors, i.e. the internal detector and the sample itself. Indeed, for a single harmonic of wavenumber υ, the sample and the internal detector receive a light beam intensity modulated by a

frequency f, that results from the back and forth movements of the mirror at speed v. The signal modulation frequency f for the harmonic υ is, thus, given by:

$$f = 2v\nu \quad (7.2)$$

Therefore, both detectors output an electrical signal of frequency f, the amplitude of which depends on their respective frequency response. As detector signals are amplified, the frequency response of the amplifiers are also to be taken into account. In order to measure a correct absorbance spectrum, the frequency response of the whole system (detectors+amplifiers) is measured by varying the speed of the movable mirror. It is found that in case of a slow enough motion of the movable mirror, the modulation frequency is sufficiently low not to influence the measurement.

To ensure that a higher FTPS point at a given wavenumber reflects a higher absorbance, one must verify that the tested sample produces a proportionally higher signal for a higher light intensity, i.e. that the current output of the sample has a linear behavior with respect to incoming light intensity. This requirement has been checked and is fulfilled for all the solar cells studied here.

When the internal detector of the spectrometer is a pyrodetector (such as the one used here), its signal must be divided by the photon energy E.

Measurement conditions

The absorbance spectrum of interest (roughly from 0.7eV to 2eV) extends over six orders of magnitude or even higher. The dynamic range of the pre-amplifier should thus be as large to detect the FTPS signal. However, current amplifiers have a dynamic range of approximately 3 orders of magnitude for a given sensitivity. The technical solution is to decompose the light spectrum into different spectral bands. Practically, two optical filters were placed on the beam path: a red (so-called KC14) filter used to measure the spectrum between 2 and 1.2eV and a 5mm-thick Si wafer coated with antireflection layer between 1.2 and 0.7eV or below. The gain of the pre-amplifier is set appropriately to amplify the FTPS signal correctly for one given band. The two FTPS spectra obtained with different gains are then put together to form the whole FTPS spectrum from 0.7eV or below, up to 2eV.

The spectra of the source measured through the different optical filters with the internal detector of the spectrometer are represented in Figure 7.4.

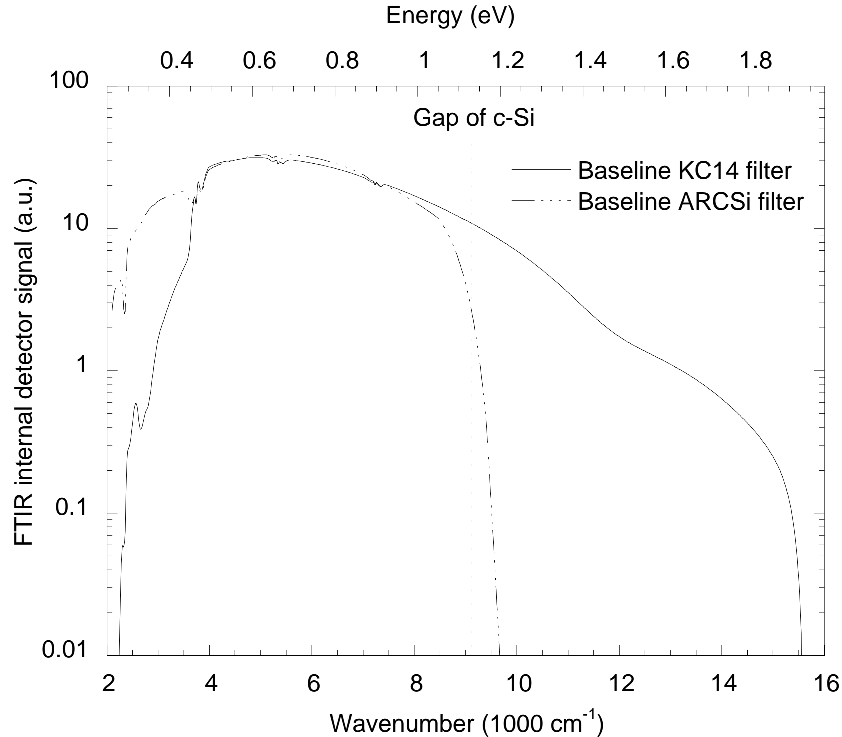

Figure 7.4: Baselines as measured on the internal detector of the FTIR spectrometer for two different filters. The filter used for the low energy region absorbance measurement is a 5mm-thick crystalline silicon wafer with an antireflection coating (ARCSi filter). The filter transmitting red and infrared light is a so-called KC14 (red) filter.

The forward bias applied to the pin and nip solar cell was just below the V_{oc}, as measured under the output beam of the spectrometer through the optical filters. Under these light conditions, the V_{oc} is much lower than that measured with the sun simulator at AM1.5 (the output beam is spectrally different and less intense than AM1.5). This forward bias allows the characterization of the cell close to its working conditions. For KC14 (red) filter, the bias was between 0.25 to 0.35V (positive voltage with respect to the n-layer). For the low energy filter (5mm thick silicon wafer coated within anti-reflection layer), the applied forward bias was in the range of 0.1 to 0.15V.

The slowest scan velocity of the spectrometer was systematically used (i.e. 0.15cm/s) in order to minimize the undesired effects related to the frequency response of the system (detector+amplifier), as discussed above.

Interpretation of FTPS spectrum

The FTPS spectrum finally obtained is proportional to the absorbance A of the sample. In Figure 7.5, the absorbance $A \sim (1-e^{-\alpha d})$ as a function of the αd

product is presented. The region of the graph corresponding to $\alpha d < 0.1$, is the region where the absorbance is well approximated by the first order term of its Taylor series, i.e. $A \sim \alpha d$. In this region, the FTPS spectrum is directly proportional to the absorption α coefficient. The region where $\alpha d \geq 1$ is called the saturation region of the FTPS signal. Indeed, in this region, the absorbance varies from 0.64 to reach asymptotically the value of 1. This is seen as a very small variation when plotted on a logarithmic scale that extends, on the other side of the plot, over several orders of magnitude towards zero. The saturation region can be used to calibrate the spectra, provided that the samples are thick enough (to ensure that the FTPS spectrum reaches the saturation region).
The calibration procedure used here is very simple: the FTPS spectra were all set to the same value at 1.8eV. This calibration is acceptable because all samples compared here have the same TCO (i.e. same surface roughness) and layer thicknesses. The value of 1.8eV was used because it is the energy at which amorphous and microcrystalline silicon have the same absorption coefficient (see Fig. 7.1).

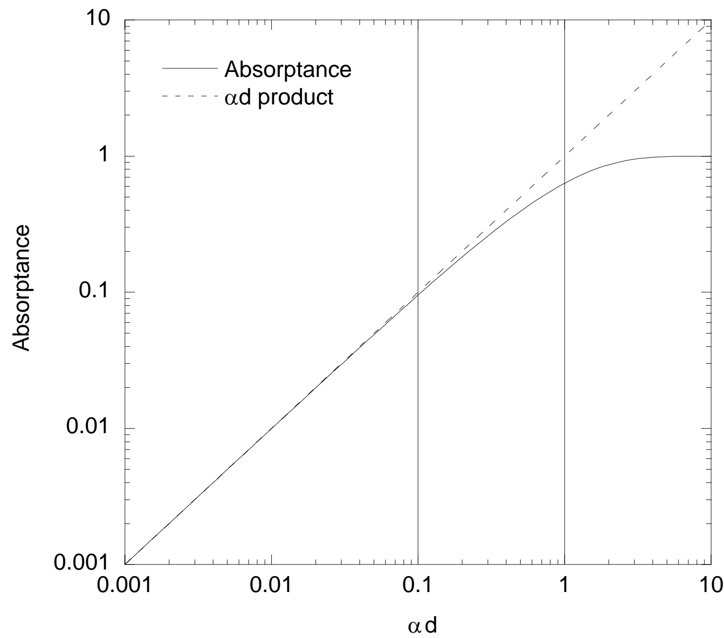

.

Figure 7.5: Absorbance $A \sim (1-e^{-\alpha d})$ as a function of αd. For values of $\alpha d < 0.1$, the absorbance is practically identical to the αd product. Above $\alpha d = 1$, the absorbance reaches the saturation regime.

7.2.2. Samples

Two series of cells were measured by the FTPS technique. The solar cells were deposited by VHF-PECVD in both nip and pin configurations on LPCVD ZnO coated AF-45 glass substrates. The deposition parameters of the doped layers within a given series were kept constant and optimized to produce conductive microcrystalline material on their respective substrate. The only parameter varied within a series was SC of the i-layer; SC ranges from values leading to fully µc-Si:H layers to values slightly above the µc-Si:H to amorphous transition.

nip cell series:

A series of five nip solar cells were deposited with i-layers at different SC ranging from 4.8% to 6.25%. The TCO on both sides is 2.4 µm thick LPCVD ZnO rough layers. The individual cells on a substrate were structured with the help of liquid plastic applied manually on the front TCO with a brush. Heating of the sample solidifies the plastic and then a dry plasma etch process is applied to remove the uncovered parts of the sample. The plastic is then removed in an acetone bath. The cell area ($<0.5cm^2$) obtained with this method is not well defined.

pin cell series:

A series of 10 pin solar cells were deposited with i-layers at different SC ranging from 5.0 to 8.0%. The front and back contacts consist in 2.4 µm thick layers of rough LPCVD ZnO. The cells were structured by laser scribing and measure $0.25cm^2$.

7.3. Results

By creating artificial defects with a proton beam, then successively annealing the cells and measuring their FTPS spectra, it is demonstrated here that FTPS is sensitive to i-layer defects.

The influence of SC on i-layer defects is also observed. For that purpose, the FTPS spectra of the series of nip and pin cells are given, accompanied by the value of the two characteristic parameters, i.e. the Urbach slope E_0 and the defect related absorption evaluated by the FTPS signal at 0.8eV.

Finally, the crystalline fraction is inferred from the FTPS spectra and compared to the crystalline volume fraction obtained from Raman measurements[15, 16].

7.3.1. FTPS spectra and proton irradiation

To assess the ability of FTPS to measure the defect related absorption, defects were artificially created by proton irradiation in one solar cell from the SC series described above. An in depth study of defect creation by proton irradiation and a degradation study of µc-Si:H solar cells is presented in reference [47].

nip µc-Si:H cells deposited at SC=4.8% were sent to CAFI for proton irradiation produced by a Van de Graaff accelerator. The proton energy at the output of the accelerator was 1MeV. An aluminum foil of 12µm was placed on the beam path to decrease the proton energy in order to obtain protons that stop after the LPCVD ZnO layer, within the i-layer of the solar cell. The estimated fluence of the proton beam was $2.38 \times 10^{13} p^+/cm^2$.

The electrical characteristics of the solar cell were measured before and after irradiation (Table 7.1). It is shown that the cell was strongly degraded by the proton beam.

Electrical characteristics (AM1.5)	Before irradiation	After irradiation	Relative variation (%)
V_{oc} (mV)	484	299	-38
FF (%)	67.1	45.9	-32
I_{sc} (mA/cm^2)	16.8	6.1	-64
FTPS at 0.8eV (a.u.)	0.01	0.14	+1300
E_0 (meV)	36.3	58.1	+60

Table 7.1: Relative variation of the electrical characteristics of a nip µc-Si:H solar cell before and after irradiation. It appears that an increase of the defect related absorption results from the irradiation. The electrical characteristics of the cell measured under AM1.5 degrade abruptly after irradiation.

The cell was then sent to Prague for FTPS measurements and stepwise thermal annealing. The results are plotted in Figure 7.6. The defect related absorption (FTPS (0.8eV)) decreases monotonously as the thermal annealing is performed and finally reaches a value close to the one measured prior to degradation. This experiment reveals that FTPS allows evaluation of the defect related absorption within complete solar cells.

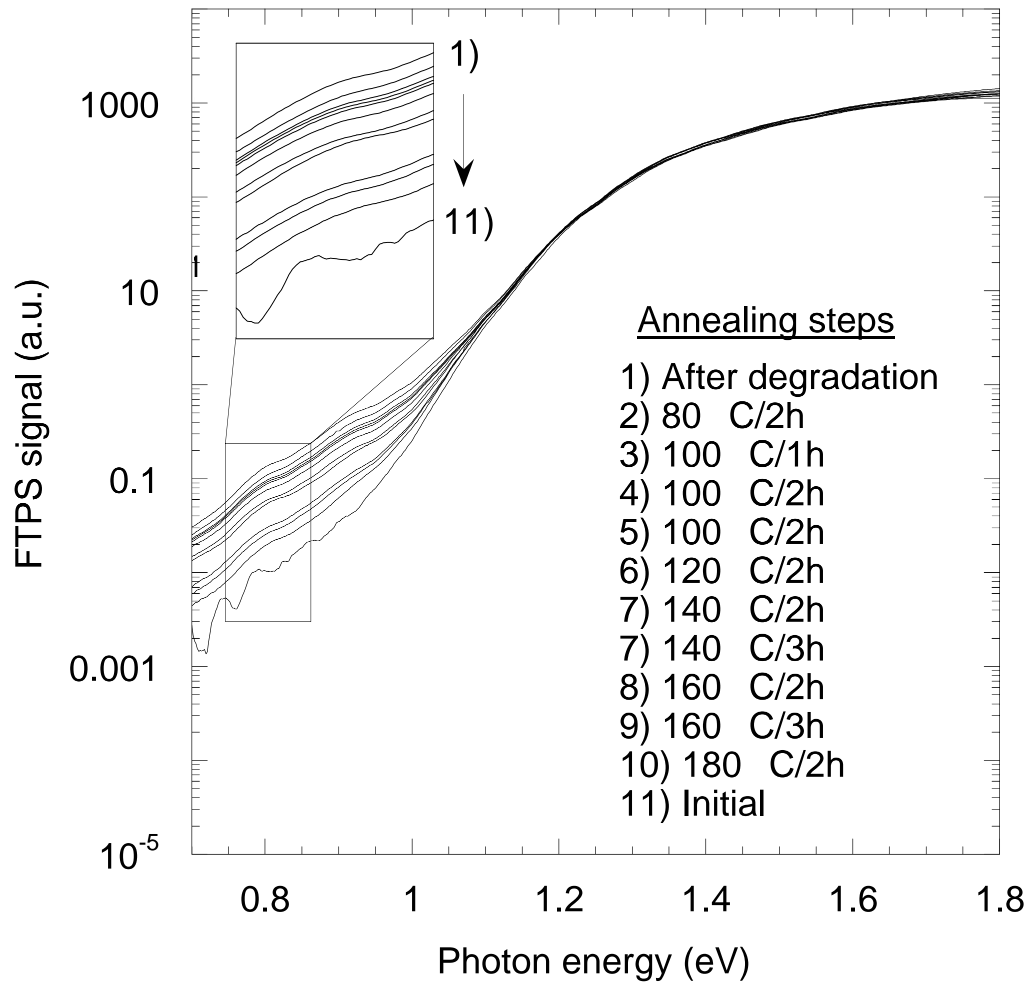

Figure 7.6: FTPS spectra of nip cell (SC=4.8%) degraded by proton irradiation and successively thermally annealed. The annealing sequence is given in the legend. These spectra reveal the decreasing defect related absorption (FTPS at 0.8eV) after each annealing step. Note the remarkable reproducibility of the FTPS measurements that allows one to distinguish the effect of each annealing step. (Thanks to A. Poruba and L. Mullerova for the FTPS measurements and the annealing steps).

In Figure 7.7 one observes that E_0 and FTPS(0.8eV) vary in a similar way when defects are created by proton irradiation. In the next section it is shown that when defects are created by varying SC, E_0 and FTPS(0.8eV) no longer vary in the same way. Defects generated in i-layers by proton irradiation may be of a different nature than defects present in i-layers deposited with different SC. The former kind of defects is mainly due to silicon atoms within the crystallites that moved from one lattice site to an interstitial site.

The latter kind of defects is thought to lie at the grain boundaries, between the crystallites. However, further studies should be done to understand the relationships between E_0 and defects as evaluated with FTPS(0.8eV).

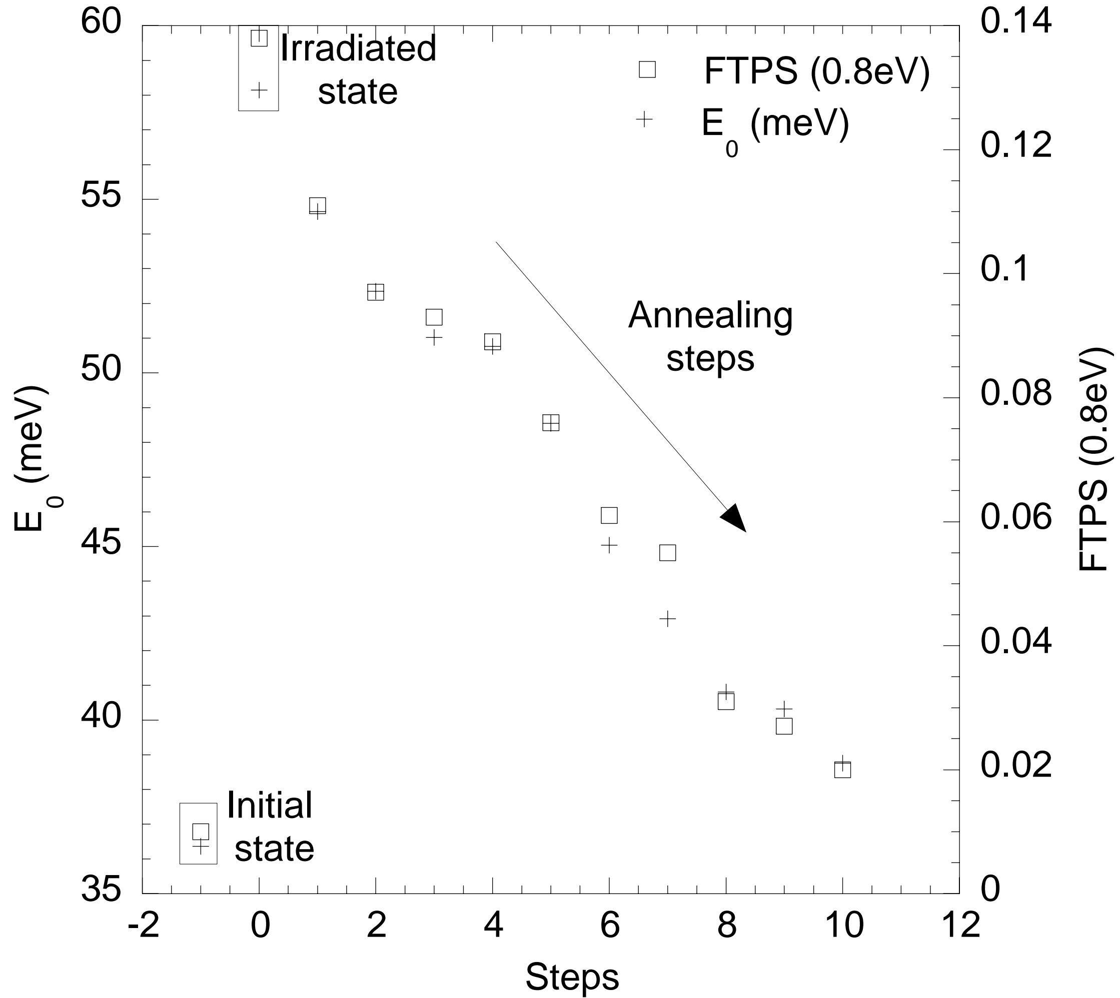

Figure 7.7: Evolution of the E_0 parameter and the defect related absorption FTPS(0.8eV) (for sake of clarity, error bars are not represented: $\Delta E_0=\pm 1meV$ and $\Delta FTPS(0.8)=\pm 5\%$). It is evident that both parameters follow the same trend in a remarkable way.

7.3.2. FTPS spectra and silane concentration

Several individual cells were measured by the FTPS technique, for each SC of nip and pin cell series. For sake of clarity, however, only a selection of the FTPS spectra is displayed in Figure 7.8 (nip cells) and Figure 7.9 (pin cells). The FTPS spectra of both series were normalized at 1.8eV (at an arbitrarily chosen value of 5000a.u.), for the reasons explained in section 7.2.1.

For both series of cells, the FTPS spectra below 1.8eV shift downwards as SC is increased. This behavior must be analyzed by decomposing the FTPS spectrum into different regions:

The region of <u>defect related absorption</u> (around 0.8eV): The absorption at 0.8eV is used to estimate the defect density of μc-Si:H[48]. Indeed, in this region, the absorption is given by transitions between the valence band and the deep defects in the gap of the material (or from deep defects to the conduction band). In the text thereafter, the term defect related absorption is used to designate the FTPS signal at 0.8eV. It appears that as SC increases, the defect related absorption reaches a minimum value.

The region of the <u>band tail state absorption</u> (0.95-1.12eV): In this region, the absorption coefficient (and the FTPS spectrum) of μc-Si:H stems from optical transitions involving band tail states. The exponential behavior of the absorption coefficient is characterized by the Urbach parameter E_0.

For both series of cells, one observes that the exponential slope gets only slightly steeper (E_0 decreases) as SC increases towards the microcrystalline to amorphous transition. The evaluation of E_0 must be done carefully as it might be influenced by the defect related absorption[24]. For that purpose, deconvolution of the FTPS spectrum should be done, assuming a model for the density of states of μc-Si:H, as it was done for the amorphous silicon[24].

The region of <u>transparency of the amorphous phase</u> (between 1.2 and 1.5eV): In this spectral region, the amorphous phase of the cell barely contributes to the FTPS signal, as long as its volume fraction is not too high (less than 90%). Indeed, in this range, amorphous silicon absorption coefficient is between 50 to 200 times lower than the absorption coefficient of the microcrystalline silicon (see Figure 7.1). For a constant cell thickness (as in both of the series presented here), the higher the amorphous fraction, the lower the FTPS signal. The decrease of the FTPS signal can be seen as a decrease of the effective microcrystalline thickness (i.e. it is not a blue shift related to an increased optical band-gap).

The three spectral regions presented above are used in the next section to infer the quality of the material that forms the active layer of the microcrystalline nip and pin solar cells.

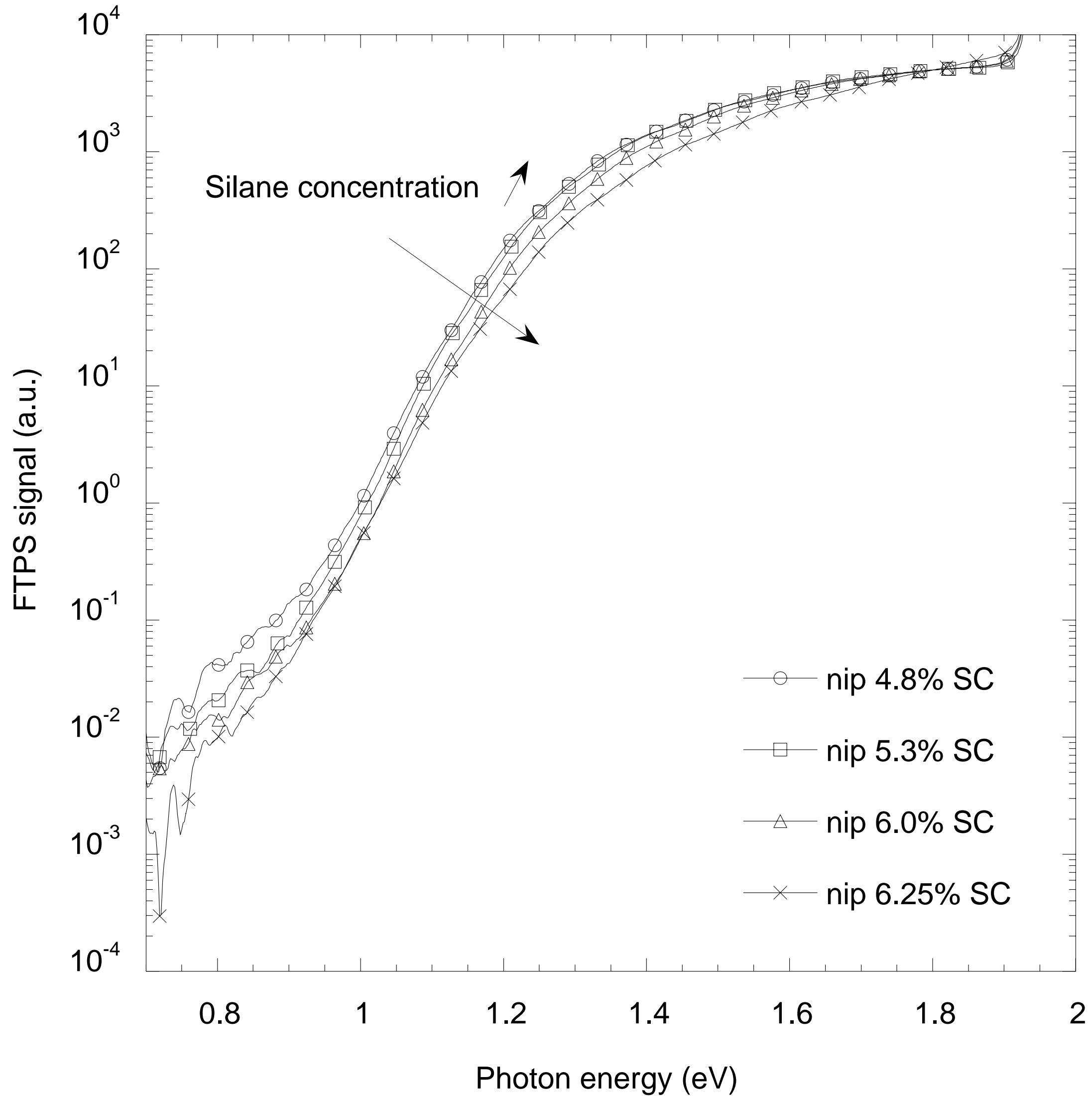

Figure 7.8: FTPS spectra of the SC series of nip solar cells. When SC increases towards the microcrystalline to amorphous transition, the FTPS spectra are shifted downwards.

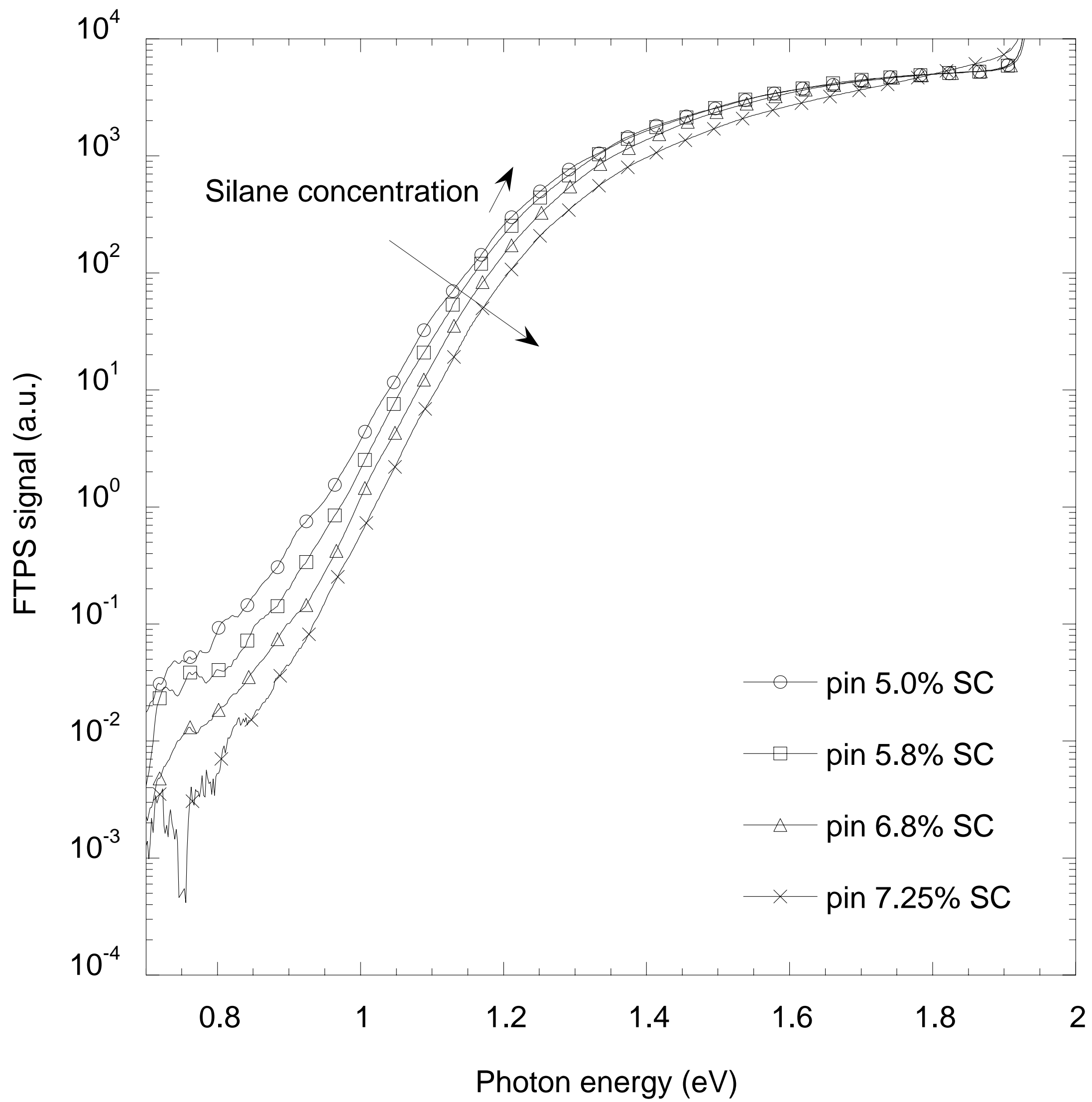

Figure 7.9: FTPS spectra of the SC series of pin solar cells. When SC increases towards the microcrystalline to amorphous transition, the FTPS spectra are shifted downwards as for the nip series.

7.3.3. Defect related absorption and SC

It is found for both nip and pin series that when SC is increased towards values close to the microcrystalline to amorphous transition the defect related absorption decreases monotonously. The defect related absorption of the nip cells decreases by a factor 2 to 3 when changing SC from 4.8 to 6.25% (Figure 7.10). The pin cells show a larger decrease of the defect related absorption, as the SC range is broader than that for the nip series (one has to mention here that nip and pin cells were deposited in different reactors). Indeed, the defect related absorption decreases by one order of magnitude when SC is increased from 5.0 to 8.0% (Figure 7.11).

In both nip and pin configurations, the i-layer material deposited close to the microcrystalline to amorphous transition exhibits lower defect related absorption than the i-layer of cells deposited at lower SC.

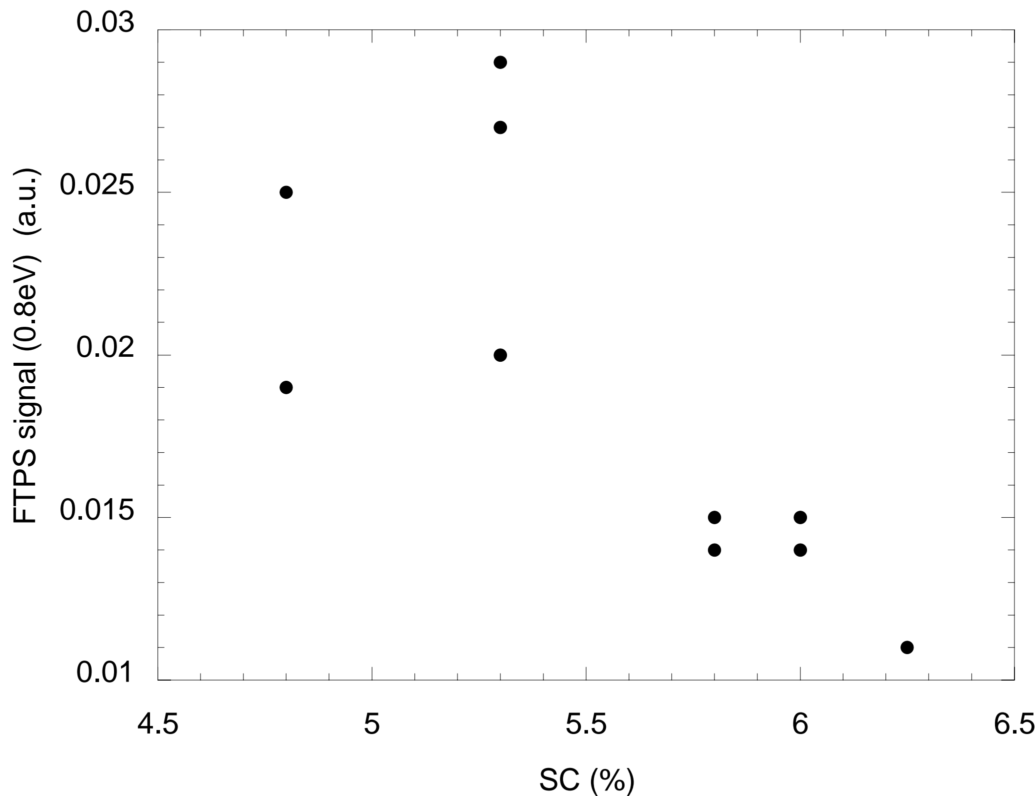

Figure 7.10: FTPS signal at 0.8eV (defect related absorption) as a function of SC for nip cells (error on FTPS(0.8eV)=±10%).

Figure 7.11: FTPS signal at 0.8eV (defect related absorption) as a function of SC for the pin cells (error on FTPS(0.8eV)=±10%).

A similar trend was observed by the electron spin resonance (ESR) technique[49] on a series of SC layers. However, ESR does not allow the measurement of the defect density directly into the cells. Indeed, the samples for ESR were obtained from single microcrystalline layers deposited on an aluminum foil, which were then dissolved to produce a microcrystalline silicon powder to perform the analysis.

7.3.4. Urbach tail slope

The Urbach parameter E_0 of the spectra was evaluated in the region below the gap, from 0.95-1.00eV to 1.10eV. The lower limit of this range was chosen to avoid as much as possible the influence of defect related absorption on the Urbach tail slope.

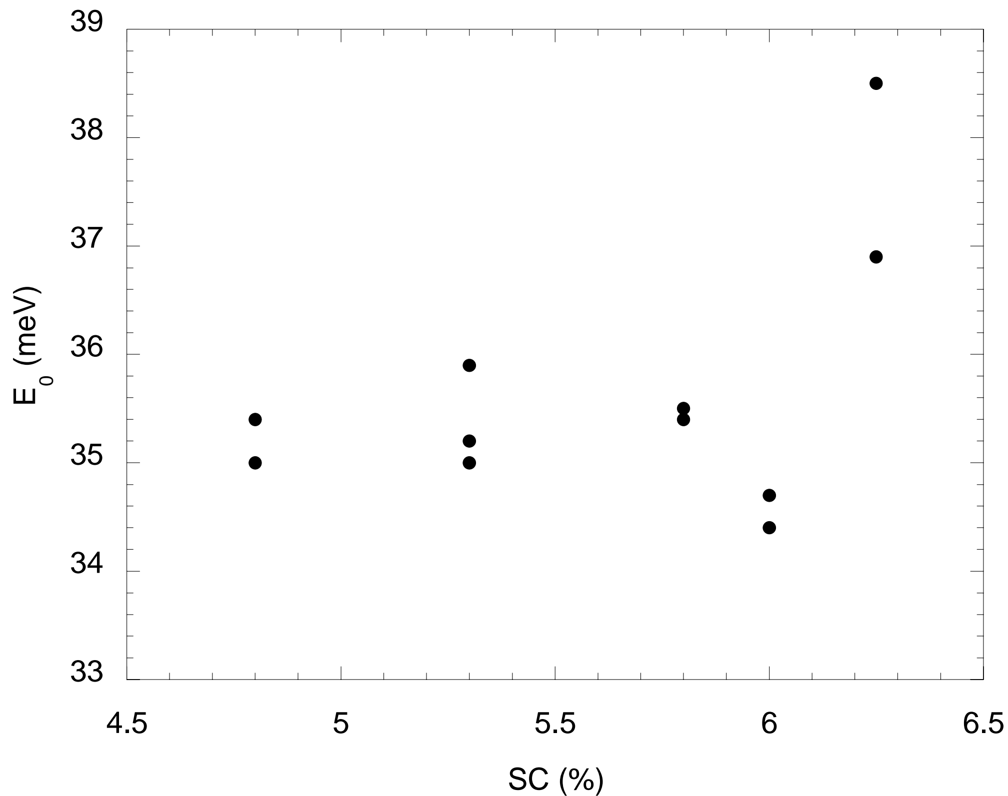

Figure 7.12: The Urbach parameter E_0 as a function of SC of the intrinsic layer in the nip cell series (error on E_0 is ±1meV). The relatively narrow SC range used for the nip cell series shows rather constant E_0 ~ 35meV (except for SC at 6.25%, for which a value of 37meV is reached).

For SC from 4.8% up to 6%, E_0 is almost constant for the nip cells. At 6.25%, the slope increases slightly. For the pin cell series one observes a constant decrease of E_0 as SC is increased. The curve minimum is reached for a relatively broad range of SC, i.e. from 6.5 to 7.2%. E_0 increases then sharply for SC=8.0%. Basically the same behavior is observed for both series, although the narrow range of SC for the nip cells does not allow for the observation of the decrease of E_0 as SC is increased (as in the case of the pin cells). For both series, the lowest E_0 is between 34-36meV.

In both series, the data corresponding to the cells deposited at highest SC (corresponding to cells slightly above the microcrystalline to amorphous transition) show higher E_0. This increase is addressed in the discussion section below.

Thus, the SC appears to influence only slightly E_0 of the bulk material. One observes that the steepest Urbach tail slopes, or smallest disorder or E_0, are

obtained for a relatively broad range of SC, in a region close to the microcrystalline to amorphous transition.

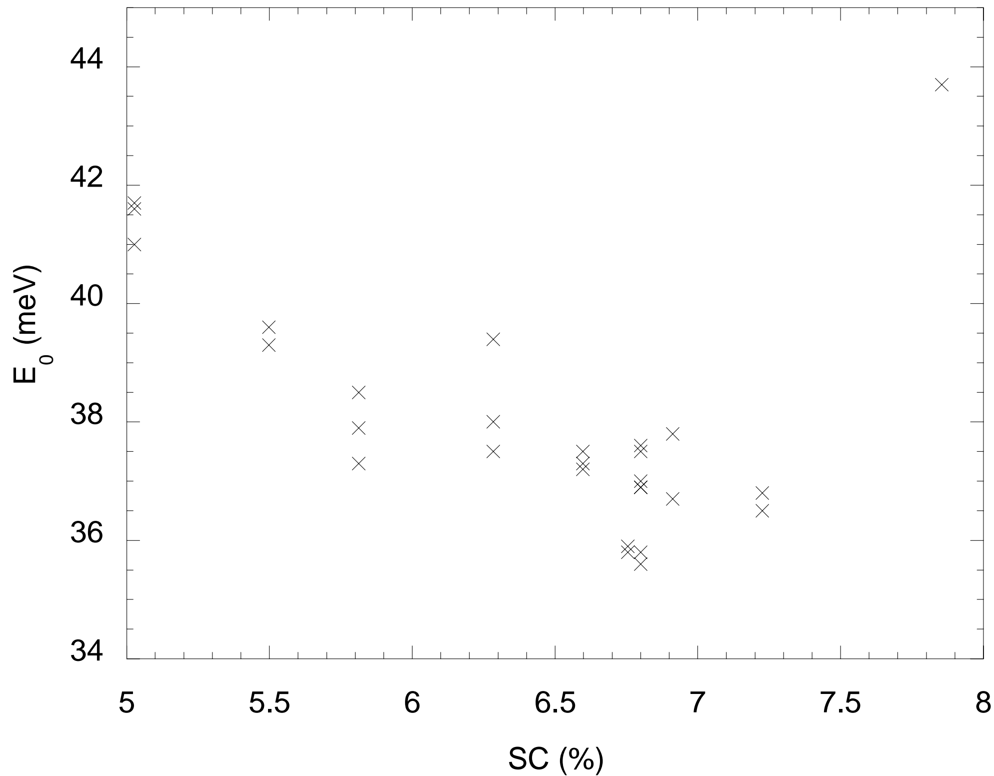

Figure 7.13: Urbach parameter E_0 as a function of SC for the pin cell series (error on E_0 is ±1meV). SC range is broader than for the nip cells. E_0 exhibits a broad minimum at approximately 37meV for values of SC comprised between 6.5 and 7.2%, whereas a sharp increase is observed for SC value of 8.0%. This is a similar behavior as observed in Figure 7.12 for the nip cell series.

7.3.5. Crystalline volume fraction evaluated by FTPS spectra

The crystalline volume fraction can be estimated, at least qualitatively, using the region of the FTPS spectrum between 1.2 and 1.5eV. In this spectral region, the amorphous phase is transparent compared to the microcrystalline phase, as can be seen in Figure 7.1. To evaluate the crystalline fraction with the highest accuracy, the value of the FTPS signal at 1.35eV is used, as it is the energy for which there is the largest difference between the absorption coefficient of amorphous and microcrystalline silicon. Indeed, for a photon energy of 1.35eV, $\alpha_{\mu c\text{-}Si:H}/\alpha_{a\text{-}Si:H} \cong 200$. The contribution to the absorbance of the amorphous phase can therefore be neglected, provided its volume fraction is not too high, i.e. less than 90%. The value of the FTPS(1.35eV)

is, thus, dominated by the microcrystalline phase composing the active layer. Therefore, for constant active layer thickness, a decrease of the FTPS(1.35eV) is related to a decrease of the crystalline fraction.

As for the evaluation of the crystalline volume fraction from Raman spectra, the evaluation of the crystalline fraction on an absolute scale with FTPS spectra is a difficult task. One could simply suppose that the lowest SC used in the series produced a microcrystalline volume fraction of 80% for instance and normalize the other points obtained for the rest of the cell series. As the plot would look exactly the same, we preferred not to introduce any speculative argument to set the absolute crystalline volume fraction and we kept the original FTPS signal at 1.35eV, which is proportional to the crystalline volume fraction.

The evolution of FTPS(1.35eV) is plotted in Figure 7.14 for the pin cells whereas a comparison of the crystalline fraction obtained by FTPS and Raman is plotted in Figure 7.15 for the nip cells.

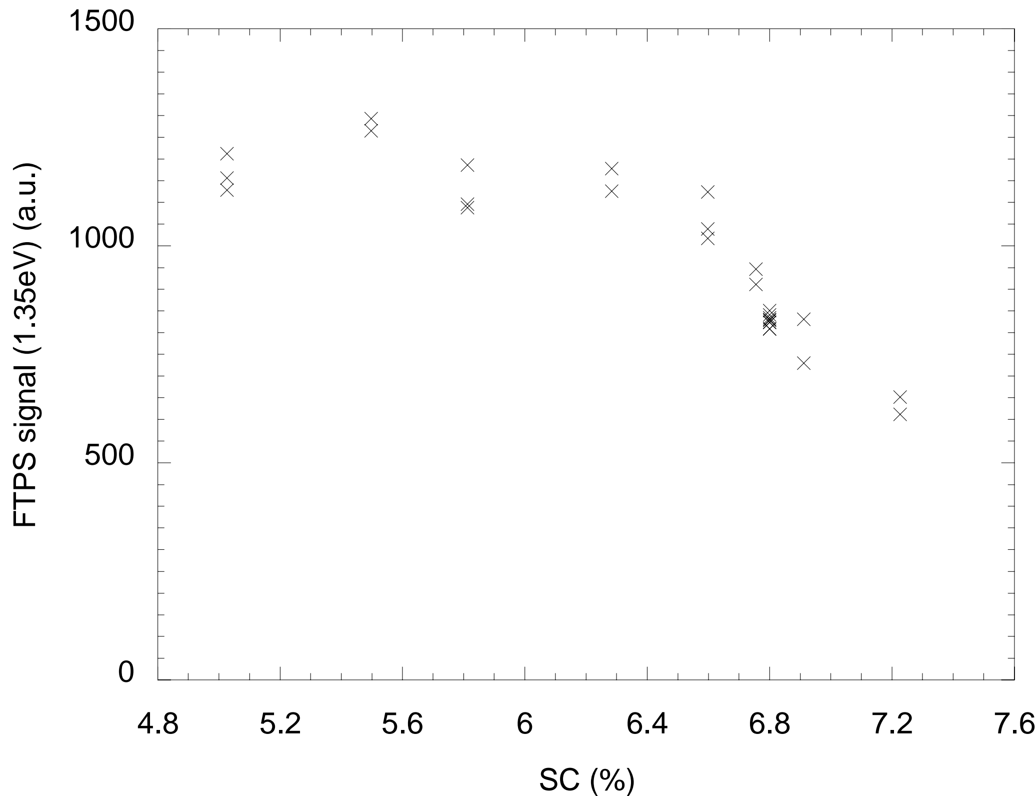

Figure 7.14: FTPS signal at 1.35eV as a function of SC for pin cells (error is ±5%). The signal qualitatively indicates the evolution of the crystalline volume fraction within the active material.

7.4. *Discussion*

7.4.1. Crystalline volume fraction obtained by Raman and FTPS

The comparison between the crystalline fraction obtained by Raman spectroscopy and FTPS technique is plotted in Figure 7.15.

Here, ϕ_c is defined as:

$$\phi_c = \frac{\phi_{ctop} + \phi_{cbottom}}{2} \quad (7.3)$$

The subscripts top and bottom refer to the side of the cell where the excitation beam entered the device.

ϕ_c obtained with an excitation line of 514nm ($\phi_{c\ 514nm}$) slightly over-weights the n-i and p-i interfaces of the cell, as the collection depth (one half of the penetration depth) is about 40nm in μc-Si:H. The microcrystalline doped layers (approximately 20nm thick) contribute strongly to the Raman crystalline peak with the 514nm excitation and, thus, to $\phi_{c\ 514nm}$.

On the other hand ϕ_c measured with the 633nm excitation line ($\phi_{c\ 633nm}$) is less influenced by the microcrystalline doped layers as the collection depth (500nm) is much larger than the doped layers' thickness (20nm). $\phi_{c\ 633nm}$ is therefore closely related to the bulk crystalline fraction of the μc-Si:H solar cells.

With the FTPS technique, the light at 1.35eV is absorbed homogeneously by the i-layer; its penetration depth is about 30μm in microcrystalline silicon, which is much larger than the i-layer thickness of μc-Si:H solar cells (approximately 1-5μm thick). Note that the i-layer properties only are evaluated, i.e. there is no contribution of the doped layers to the FTPS signal.

It is also to be mentioned that the use of FTPS technique for assessing the crystalline volume fraction is sensitive to the microcrystalline phase only. The presence of voids or amorphous material decreases the FTPS signal at 1.35eV, resulting in a decreasing FTPS crystalline fraction. On the other hand, the Raman technique is sensitive to the amorphous and the crystalline material and is not affected by voids. For these reasons, the two methods are complementary for estimating the crystalline volume fraction of the i-layer.

The crystalline fractions, estimated by FTPS at 1.35eV, were set arbitrarily to the value of $\phi_{c\ 633nm}$ at SC=4.8%. The comparison between the Raman and FTPS crystalline fractions shows that the same trend is observed for the three techniques (Figure 7.15).

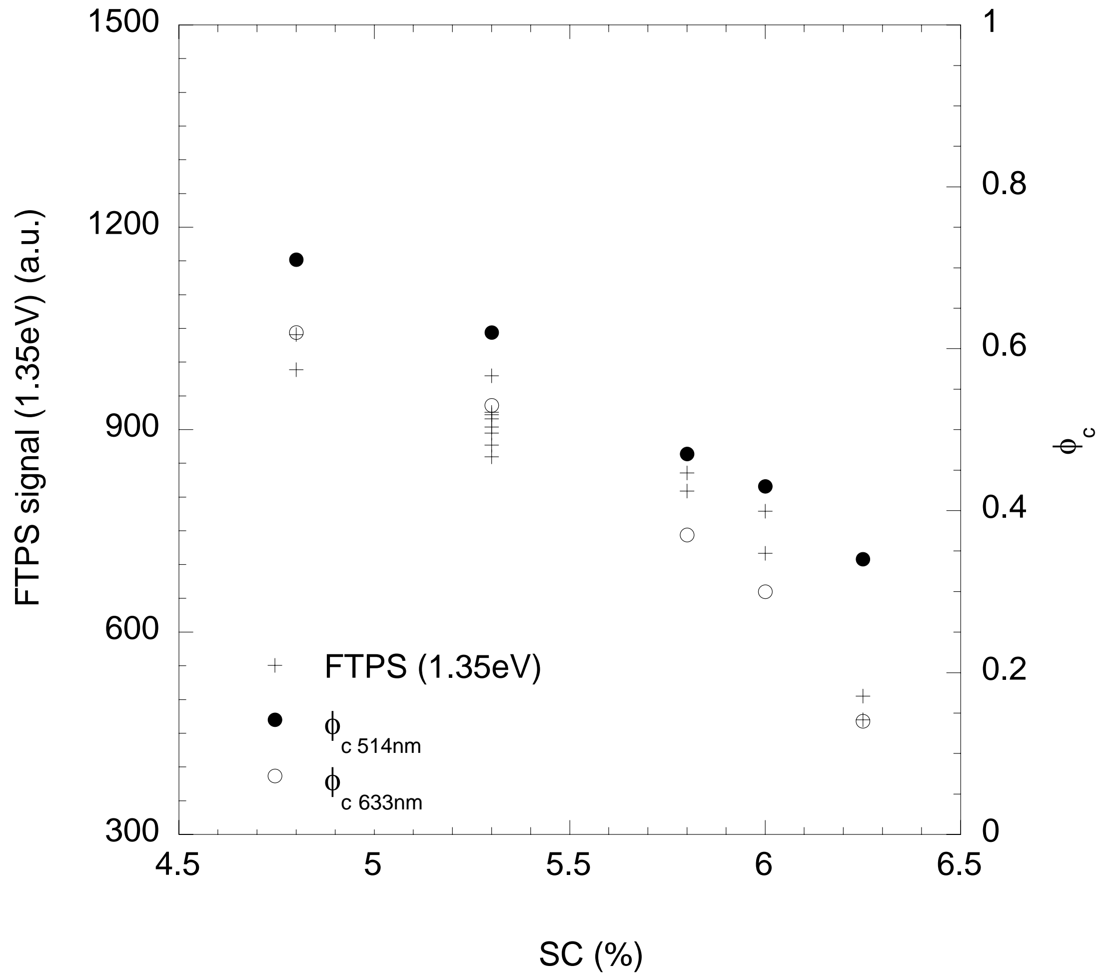

Figure 7.15: Comparison of the crystalline fractions as obtained by the FTPS signal at 1.35eV (918nm) and by Raman spectroscopy with 514 and 633nm excitation lines; see the text for experimental details (error is approx. ±5% for each technique). $\phi_{c\ 633nm}$ is in good agreement with the crystalline fraction obtained with FTPS at 1.35eV as they are both probing the whole i-layer. $\phi_{c\ 514nm}$ is slightly higher than the other two crystalline fractions as most of the excitation beam is collected from the fully microcrystalline n and p-doped layers.

7.4.2. Material quality of the i-layer

FTPS measurements on μc-Si:H solar cells irradiated by proton evidenced that FTPS(0.8eV) monitors the defect density of the i-layer. The latter is known to be very important in order to make good solar cells[47], as is also shown here by the study of an irradiated and annealed cell. As the defect related absorption is increased by a factor of ten, it is observed that the V_{oc} decreases by 38%, FF by 32% and I_{sc} by 64% (Table 7.1). E_0 varies in a remarkably similar way as FTPS(0.8eV) in the case of defects created by proton irradiation.

It has been observed here that when SC is increased towards the microcrystalline to amorphous transition, the amorphous volume fraction increases and at the same time, the electronic properties improve (the defect related absorption decreases). This behavior is at first sight counter-intuitive: when the amorphous fraction is higher, the microcrystalline solar cell is better. However, the amorphous material was observed to have an excellent surface passivation effect when deposited on a crystalline silicon wafer[38]. It is thus tempting to relate the increase of amorphous volume fraction with an improved passivation, that leads to the observed reduction of the defect related absorption.

Values of E_0 presented here range from 35eV to 42eV. The higher E_0 value of the microcrystalline silicon as compared to monocrystalline silicon (9.6meV) could be due to disorder at the surface of the nano-crystals caused by the bulk to surface discontinuity. The effect of the incorporation of the amorphous phase may possibly result in a relaxation of such distorted network by removing the discontinuity. This could explain why the increase of SC towards the transition decreases slightly the E_0 parameter.

The increase of E_0 for the cells prepared at the highest SC in nip and pin configurations is more difficult to understand. It could be due to too high amorphous volume fraction that contributes significantly to the absorption spectrum. This could hinder the interpretation of E_0 as a parameter related to the disorder of the material.

7.5. Conclusions

Stepwise annealing of a solar cell degraded with a proton beam demonstrated that FTPS(0.8eV) yields valuable and reproducible information on the defect density of the i-layer within the complete solar cell.

From the FTPS spectra of two series of microcrystalline solar cells in both nip and pin configurations, the following characteristics were measured: defect related absorption, Urbach tail slope and the crystalline fraction.
It is observed that the cells deposited under conditions close to the microcrystalline to amorphous transition have a higher amorphous volume fraction as well as better electronic properties than the cells deposited at lower SC. The passivation of the nano-crystal surface by the surrounding amorphous material could explain that behavior. This passivation effect was already observed for amorphous silicon on silicon wafer based solar cells.
In the case of too high amorphous fraction (>90%), the interpretation of the FTPS spectrum in the low energy range is yet to be understood.

8. Relationship between i-layer quality and V_{oc}

8.1. Introduction

In the previous chapters the variations of microstructure and electronic properties within the active layer, resulting from the variation of SC, were investigated. They revealed that the main varying features of the microstructure are the nuclei density and the thickness of the heterophase layer (chapter 5). In chapter 7, in agreement with previous studies [28], it is reported that the amorphous fraction within the i-layer increases when SC is raised. In the same chapter, it is found that, simultaneously the defect related absorption decreases. The present chapter is focused on improving the understanding of the V_{oc} and its variations with respect to the structural and electronic quality of the intrinsic layer. The density of states within the band-gap of the i-layer appears to have an important impact on the V_{oc} of the solar cells.

8.2. Experimental

The results presented here are based on the two series of nip and pin solar cells used in chapter 7. The FTPS technique used to characterize the cells is described in chapter 7.

Illuminated current-voltage (IV) characteristics of the cells under the AM1.5 spectrum were performed on all samples of the series to obtain the V_{oc} and the FF. The current was deduced from quantum efficiency measurements, to avoid the problem of ill-defined area of the cells structured manually.

8.3. Results

8.3.1. V_{oc} versus SC

In this section, the V_{oc}, FF and I_{sc} of the nip and pin series as a function of SC are presented. The discussion is focused on the V_{oc}, however, which is not affected by light trapping properties of the substrate and i-layer thickness (in contrast to I_{sc} and FF). For comparison, the electrical characteristics of nip and pin cell series are plotted on the same graphs. However, as the series were deposited under different conditions and in different reactors, the microcrystalline to amorphous transition does not take place at the same SC in both cases. The trends observed for the nip and pin series are similar except for a horizontal (SC) shift.

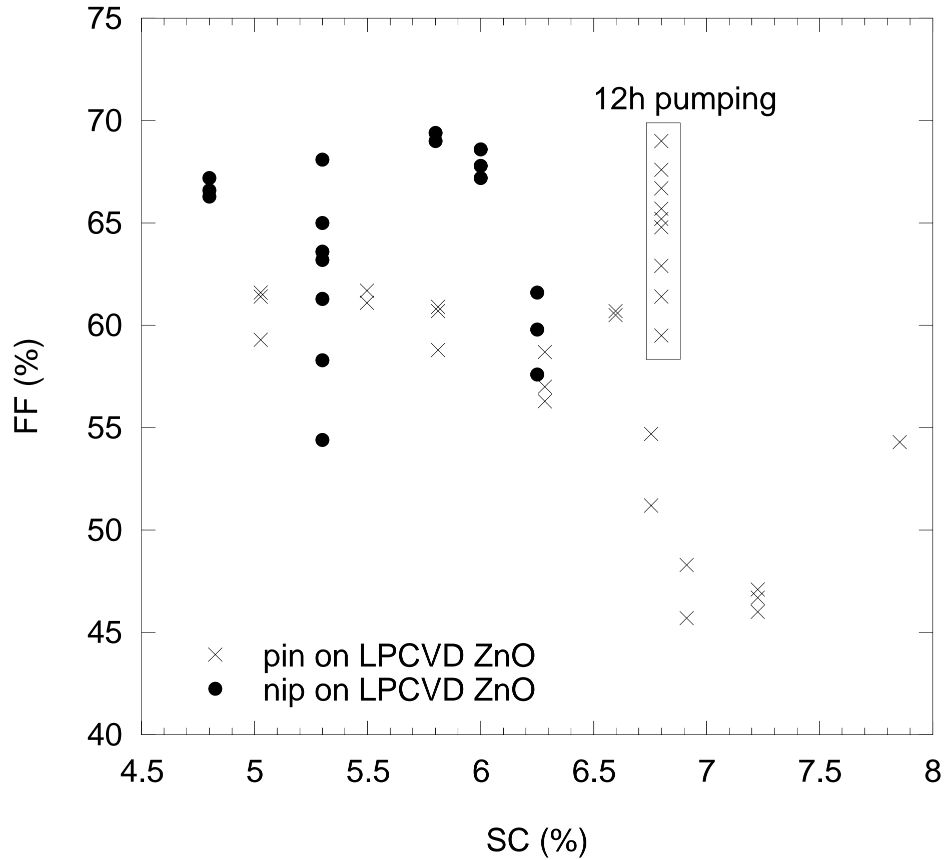

Figure 8.1: Evolution of FF as a function of SC for nip and pin series of cells on LPCVD ZnO. Note that a longer pumping time improved FF of pin cells deposited at 6.8%.

FF and SC

In Figure 8.1, FF of all cells measured in the previous chapter are presented. FF are not homogenous over the whole substrate area for a given SC (e.g. nip cells at 5.3% SC). In spite of the scattering of FF, one can observe in both sample series an abrupt decrease of FF for the cells deposited at high SC, i.e. close to or beyond the microcrystalline to amorphous transition. This transition is reached above 6.0% and 6.8% SC for the nip and pin, respectively. For these samples, the first stages of the growth are likely amorphous and the transition to crystalline growth regime is reached further up, after a few hundreds of nanometers as also observed previously[9, 50]. The possibly thick and fully amorphous incubation layer followed by a gradual transition from amorphous to crystalline with respect to the film thickness likely acts as a barrier that decreases the collection of the carriers. Further studies, though, are required to be affirmative on that issue.

The series of nip cells exhibits also a generally higher FF than the pin series. This behavior is probably due to the fact that the pin cells were deposited in a single chamber, whereas the nip cells were deposited in a double chamber system (one chamber for doped layers and the other one for the i-layer). The latter system avoids residual dopants from the chamber to be incorporated in the i-layer during its deposition. This hypothesis is supported by the fact that a significantly longer pumping time before the deposition of the i-layer (approximately 12 hours) strongly enhances FF (pin cells deposited with 6.8% SC had such a longer pumping time, see Figure 8.1 and Figure 8.2).

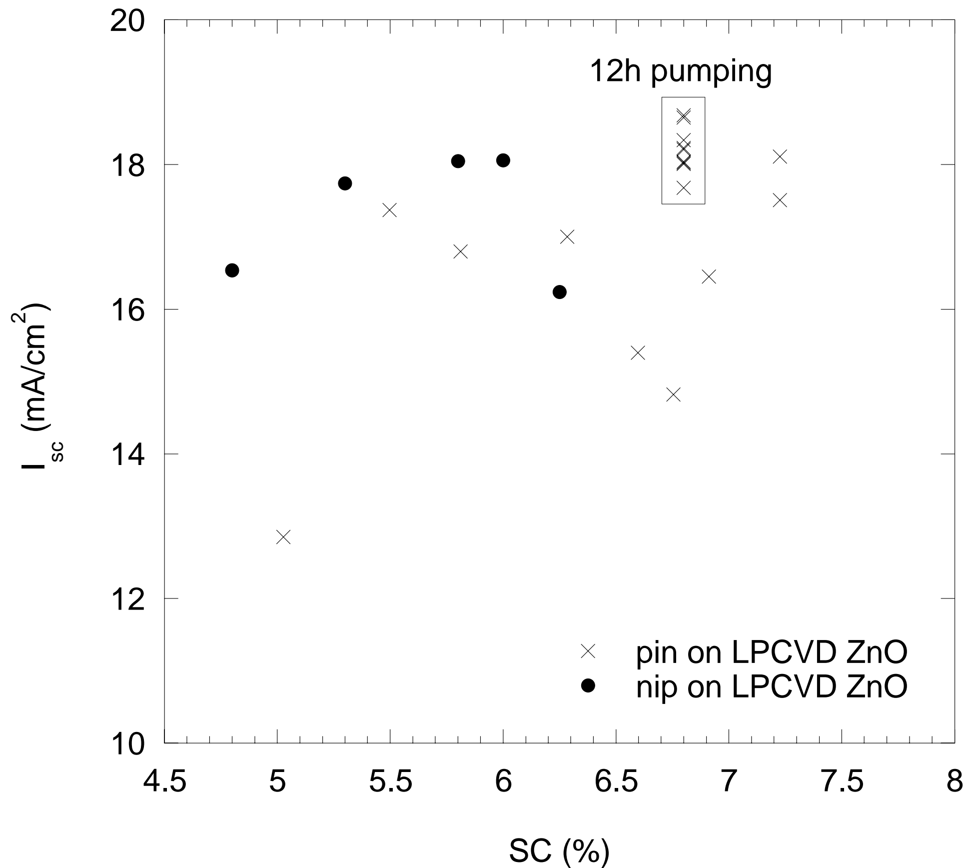

Figure 8.2: I_{sc} of the cells as a function of SC used for the deposition of the i-layer in nip and pin cells.

Isc and SC

The scattering of I_{sc} vs SC is partly related to the difficulty of maintaining the i-layer thickness constant for such SC series of samples. I_{sc} is also very sensitive to TCO inhomogeneity. For these reasons I_{sc} was not thoroughly investigated within this study.

Voc and SC

In Figure 8.3, the increase of the V_{oc} as a function of SC is verified for both SC series[7]. V_{oc} appears to be much less scattered than FF or I_{sc} of the same cells. This parameter does not depend in a major way on the i-layer thickness and is completely independent of the cell area.

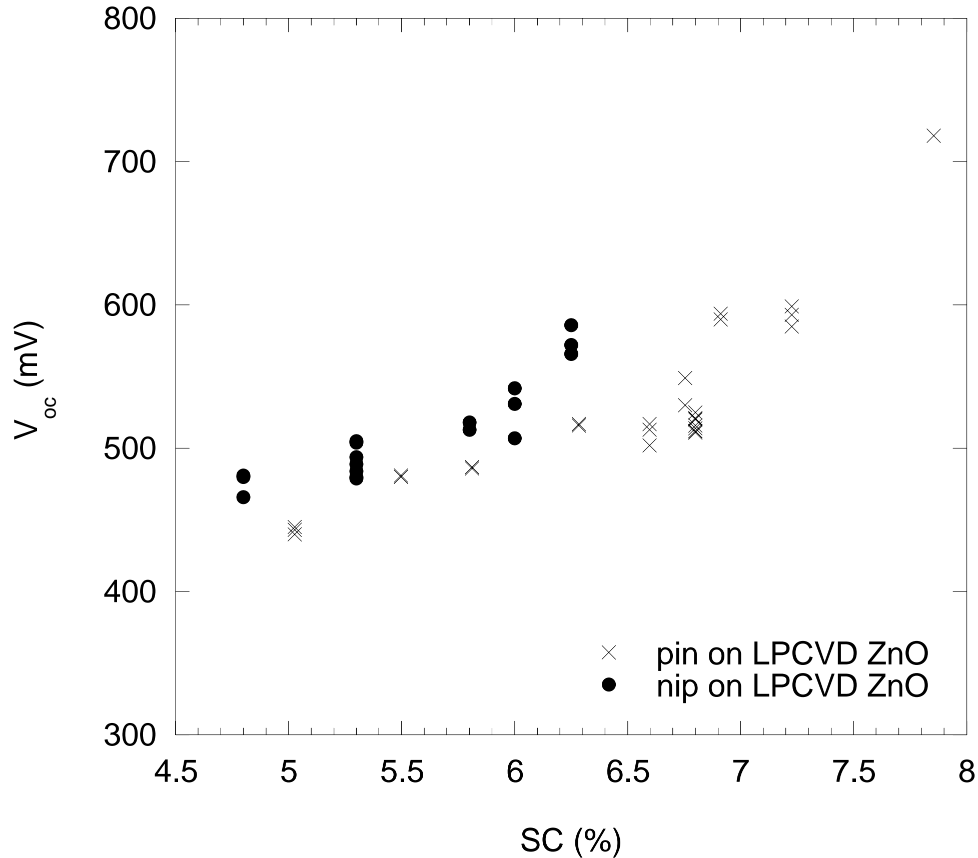

Figure 8.3: V_{oc} as a function of SC used for the deposition of the i-layer in nip and pin solar cells.

8.3.2. V_{oc} and amorphous volume fraction

As reported previously[15, 16], the increase of the V_{oc} is related to the amorphous volume fraction increase within the active layer for both nip and pin cell configurations. The crystalline fraction of the active layer, in the present chapter is measured by the FTPS signal at 1.35eV. More details are given on this technique in chapter 7. The increase of the amorphous fraction corresponding to the increase of V_{oc} is shown in Figure 8.4 for the nip solar cells (similar behavior is observed for the pin solar cells). In this figure, the crystalline volume fraction obtained by Raman spectroscopy with a 633nm

excitation beam ($\phi_{c\ 633nm}$, as defined in equation 7.3) is superimposed. Although this relationship between the amorphous fraction and the V_{oc} has been observed in several research groups, the fundamental mechanism behind the increase of V_{oc} remains unclear. It should be noticed that, in view of the results presented in the previous chapter on defects created by proton irradiation, the V_{oc} was changed from an initial value of 484 down to 299mV (see Table 7.1) without variation of the amorphous fraction. The presence of amorphous fraction is therefore not the only reason for a good V_{oc}. The electronic quality of the i-layer has certainly an important role to play.

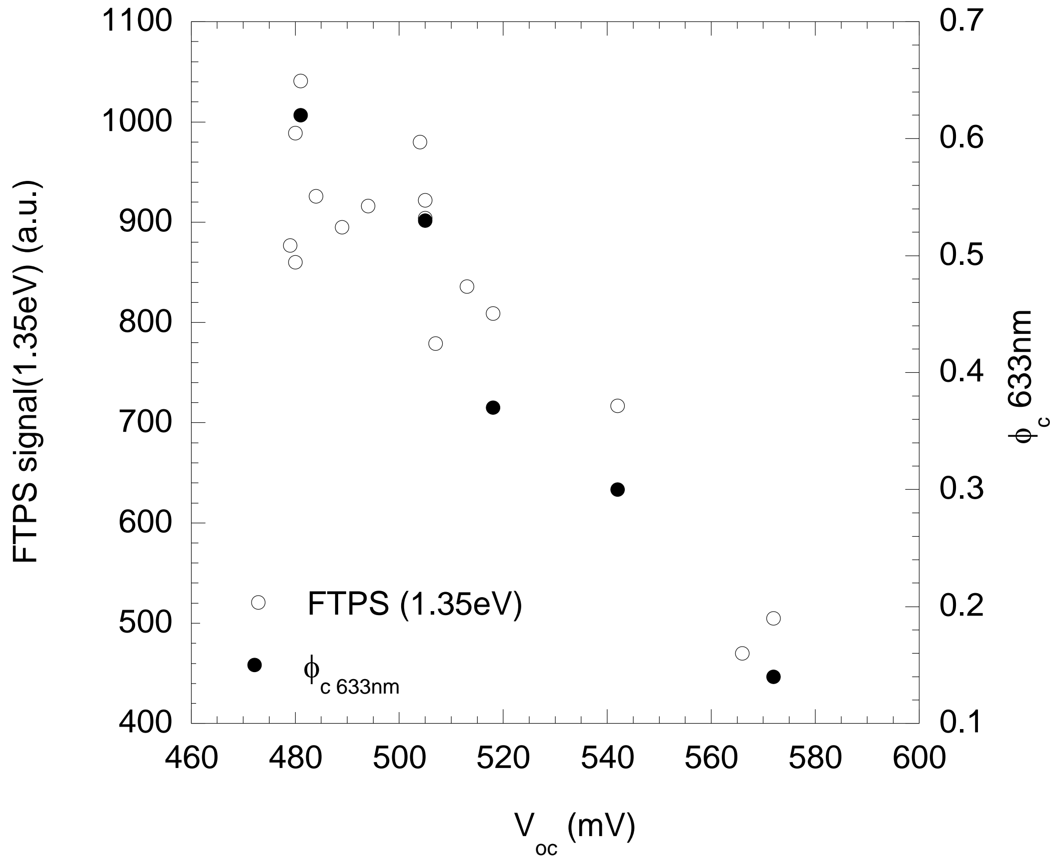

Figure 8.4: Comparison of the relationship between V_{oc} and crystalline volume fraction estimated by Raman spectroscopy ($\phi_{c\ 633nm}$) and FTPS evaluated at 1.35eV for the nip cells (error is approx. ±5% for each technique). Although the collection depth is not the same, similar trends are observed with both techniques.

8.3.3. V_{oc} and sub-gap states

The sub-gap absorption as measured by the FTPS technique gives valuable information on the defect density of the i-layer in the complete solar cell. It was therefore used to monitor the evolution of the V_{oc} with respect to the defect related absorption.

The µc-Si:H solar cell that was stepwise annealed after proton irradiation was used to observe the evolution of the V_{oc} with respect to the defect related absorption in Figure 8.5. The V_{oc} was measured 'in situ', i.e. under the output beam of the spectrometer with a red filter (KC14) for practical reasons. Under these illumination conditions the V_{oc} is significantly lower than its value under the standard spectrum AM1.5. It is observed that the V_{oc} increases when the defect density, as monitored by FTPS(0.8eV), decreases.

In Figure 8.6, the evolution of the V_{oc} as a function of the FTPS(0.8eV) is plotted for both nip and pin solar cells. It is shown that the lower is the defect related absorption the higher is the V_{oc}. This relationship is verified for both nip and pin cell configurations.

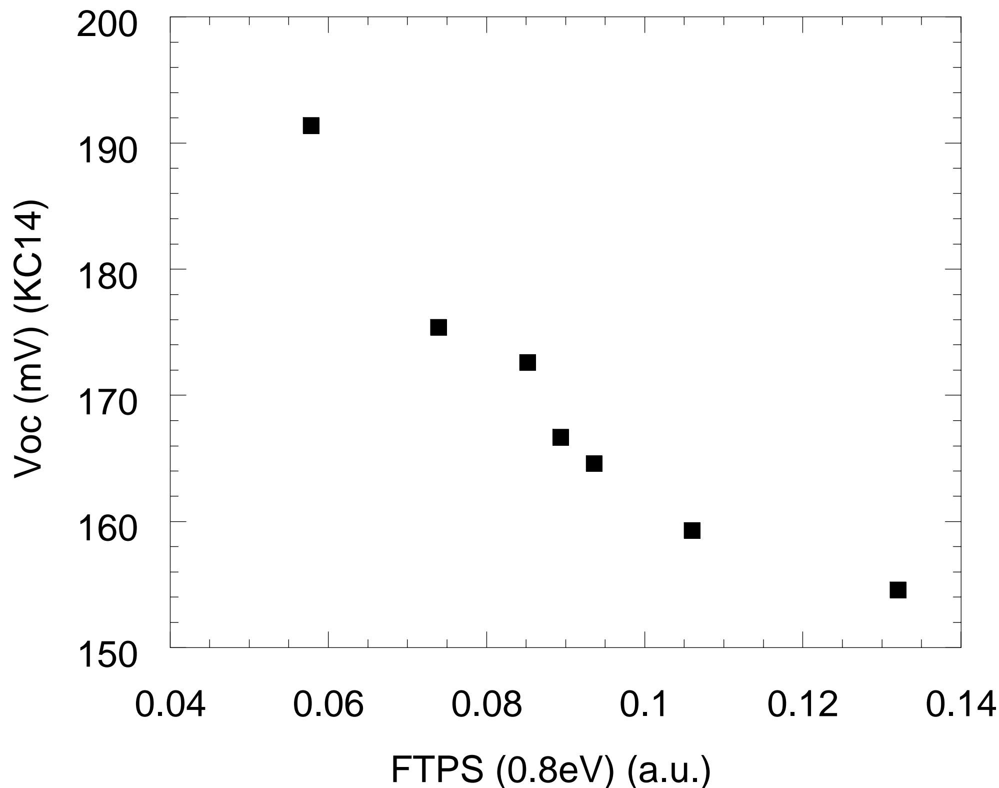

Figure 8.5: V_{oc} as a function of the defect related absorption in a nip solar cell deposited at SC=4.8% (error on FTPS(0.8eV) is approx. ±10%). Defects were created within the i-layer by proton irradiation and then stepwise annealed.

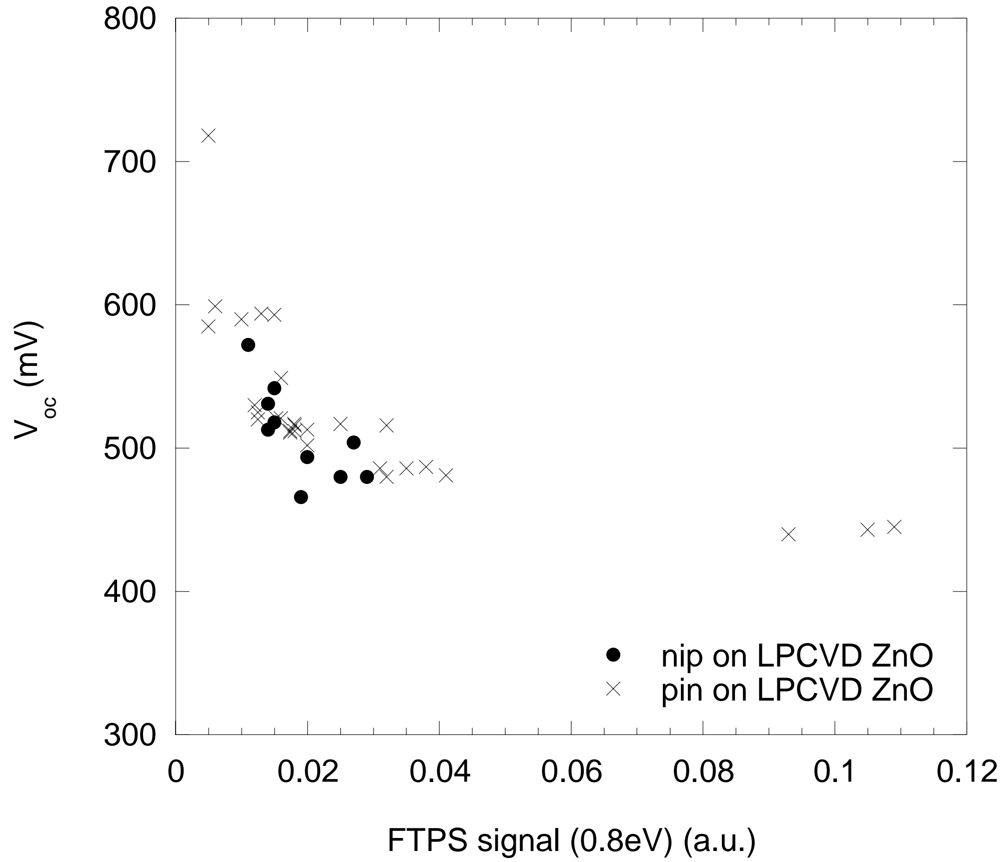

Figure 8.6: V_{oc} evolution as a function of the defect related absorption, for both nip and pin cell series (error on FTPS(0.8eV) is approx. ±10%).

8.4. Discussion

8.4.1. V_{oc} basics

When a solar cell connected to a load is illuminated, a voltage is formed at its contacts, in the forward bias polarity (+ to p and - to n-layer) as represented in Figure 8.7. This forward bias results in a forward dark-current I_{dark} opposite to the photocurrent I_{ph}. When the superposition principle can be applied, the cell current output I_{out} is given by equation (8.1).

$$I_{out} = I_{ph} - I_{dark} \quad (8.1)$$

Note that for nip and pin amorphous thin film solar cells, the superposition principle does not fully apply.

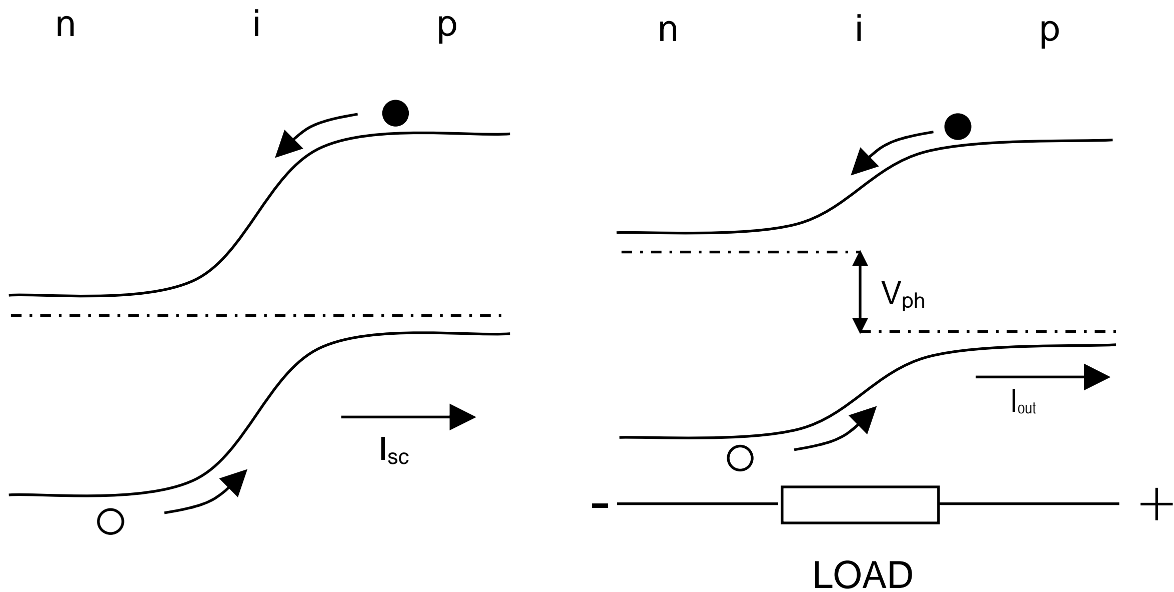

Figure 8.7: Schematic band diagram of nip solar cell under illumination. On the left, the cell is under short-circuit conditions whereas on the right, the cell is connected to a load. In the latter case, the voltage generated at the output of the device stems from the difference between the quasi–fermi levels.

The dark current in the forward direction is consequently as significant as the photo-generated current in order to understand the cell behavior. Several mechanisms add-up to form the dark-current as shown in Figure 8.8. All these mechanisms depend on the doping level of the doped layers:

- The injection current I_{inj}: electrons injected from the n-layer diffuse to the p-layer. (The same mechanism applies for holes from the p-layer to the n-layer.) This mechanism depends on the possible potential barriers or potential spikes that may exist in the band diagram of the junctions. An amorphous layer or a change of nuclei density at n-i or p-i interfaces (in nip or pin configurations, respectively) could affect I_{inj} in μc-Si:H solar cells (see 8.4.3).
- The recombination-generation current I_{rg}: carriers injected in the depletion region recombine through gap states such as deep defects. This is likely to be the most important mechanism in pin and nip μc-Si:H solar cells (see 8.4.2).
- The tunneling current I_{tun}: carriers injected in the depletion region tunnel from valence or conduction band into states within the band-gap. Then the carriers either recombine or tunnel again into band-gap states towards the other band.

The sum of these contributions results in the total dark current:

$$I_{dark} = I_{inj} + I_{rg} + I_{tun} \quad (8.2)$$

In pn mono-crystalline silicon solar cells the first contribution I_{inj} is the most significant, for pin and nip, the second (I_{rg}) plays an important role and the latter (I_{tun}) appears mostly important in hetero-junction[51]. The latter term I_{tun} is not taken into account in the following discussion.
In the case of an ideal diode, the dark current I_{dark} is given (8.3) by

$$I_{dark} = I_0(e^{qV/nkT} - 1) \quad (8.3)$$

where the exponential pre-factor I_0 (diode saturation current) and the diode ideality factor n are used to approximate the sum of I_{inj} and I_{rg}. V is the applied voltage, k the Boltzmann constant and q the charge of the electron. Under open-circuit conditions, I_{out} (in Equation 8.1) is obviously zero and I_{dark} equals I_{ph}. The following formula can be derived for the V_{oc}:

$$V_{oc} = \frac{nkT}{q}\ln(\frac{I_{ph}}{I_0} + 1) \quad (8.4)$$

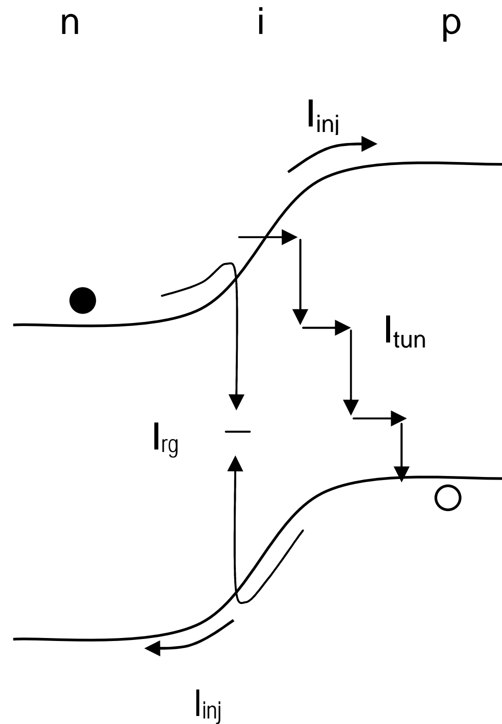

Figure 8.8: Components of the dark-current in an nip junction: injection current I_{inj}, multi-step tunneling current I_{tun} and generation-recombination current I_{rg} (see the body of the text).

8.4.2. Amorphous fraction, defect density and V_{oc}

It has been reported earlier[15, 16] that an increase of amorphous volume fraction enhances the open-circuit voltage. It was observed in the previous chapter that when the amorphous fraction increases, changes occur simultaneously in the density of band-gap states, i.e. a decrease of both the defect density and the band tail states. It is reasonable to postulate that the amorphous fraction could be responsible for the passivation of the nano-crystals. This reduces the defect related absorption observed by FTPS and therefore yields an enhancement of V_{oc}.

The effect of passivation of a crystalline surface by amorphous silicon was observed for a special kind of solar cells, the so-called both sides amorphous passivated solar cell (BAP)[38]. These cells are made of a doped crystalline wafer sandwiched between two amorphous intrinsic layers (thinner than 10nm) plus, on the front side, the microcrystalline emitter and the TCO and, on the back-side, the back surface field layer and TCO. In this paper, the thickness of the amorphous layer was varied from 0 to 7.5nm resulting in a variation of the open-circuit voltage from 570 to 610mV, respectively. Thus, the passivation of the wafer surface by the amorphous layer resulted in an increase of the open-circuit voltage. In the pin and nip devices studied here, the same effect is observed in the bulk of the microcrystalline layer: the interstitial amorphous material incorporated between and within the conglomerates of nano-crystals passivates their surfaces. This passivation possibly reduces the component I_{rg} of the dark-current in the formula (8.2). It corresponds to a reduction of I_0 and n, which leads to an enhancement of the I_{ph} to I_0 ratio. It is to be mentioned that although one may think that, from formula (8.4), a large n yields a high V_{oc}, a small n is actually required. Indeed, I_0 depends exponentially on n and dominates the expression for the V_{oc}. The plot of V_{oc} as a function of the defect related absorption (Figure 8.6) shows that the former depends strongly on the latter as one would indeed expect assuming correct the model suggested above.

8.4.3. Nuclei density and V_{oc}

In chapter 5, it was observed with a TEM study of µc-Si:H solar cells from a SC series that the V_{oc} increases as the nuclei density decreases. The observed nuclei grow on top of the doped microcrystalline layer by local epitaxy.

This observation is in agreement with the above model, which explains the increase of the V_{oc} by the increase of the amorphous fraction within the i-layer. Indeed, the smaller the nuclei density, the larger is the amorphous

fraction and the better is the passivation of the microcrystalline conglomerates.
One could speculate, however, that another effect could be responsible for the observed increase of the V_{oc} with respect to SC, in addition to the bulk quality of the active layer. This effect could be related to the nuclei density itself at the p/i or n/i interface (in pin or nip cells, respectively), where the growth of the active layer starts. The forward current I_{inj} injected over the barrier potential (Figure 8.7) could indeed be lower when the material at the junction is partially amorphous. The higher gap of the amorphous silicon, compared to the crystalline silicon, would give rise to a higher potential barrier at the p/i or n/i junction and would, thus, reduce that component of the total dark current. On the other hand a fully amorphous potential barrier of several tens of nanometer at that interface would strongly reduce the FF of the cell (but would still increase the V_{oc}).
Further investigations and tailoring of the quality and structure of both p/i and n/i interface could possibly lead to a higher V_{oc} in microcrystalline silicon solar cells without the drawback of reducing FF, as it did with the BAP structure for mono-crystalline silicon solar cells.

8.5. Conclusions

We have related here the defect related absorption to the open-circuit voltage. It is observed that **the open-circuit voltage decreases in a major way when the defect density increases**.
A mechanism for the make-up of the V_{oc} is proposed, where the amorphous tissue is responsible for the passivation of the nano-crystals surface and therefore reduces the dark-current component, which stems from deep defect states. Thus, it improves the photo to saturation current ratio on which the V_{oc} depends (see formula 8.3).
The possible influence of the nuclei density of the active layer on the V_{oc} was also pointed out. An optimization of the nuclei density and of the amorphous fraction (possibly with a different structure than the standard pin or nip configuration) could lead to a further increase of the V_{oc} of μc-Si:H solar cells without decreasing FF.

9. Conclusions

Microstructure, growth and electronic quality of the i-layer of μc-Si:H solar cells were studied with the aim of improving the understanding of their behavior with respect to SC. Of particular interest was the relationship between the microstructure and the electronic quality of the intrinsic layer and the open-circuit voltage. The work was divided into two different parts: microstructure and growth (chapters 3 to 6) and electronic quality of intrinsic layer (chapters 7 and 8).

Microstructure of μc-Si:H

After introducing the terminology for describing the microstructure of μc-Si:H, a study of the influence of the substrate surface chemistry and topography on the growth of intrinsic layers was carried out. It was shown that the **substrate surface chemistry influences the nucleation of the i-layer in a major way**. On the other hand, a comparison between layers grown on flat and rough substrate having the same surface chemistry demonstrated that **substrate surface morphology has negligible effect on nucleation**. However, the **substrate surface morphology controls the crystalline/amorphous phase distribution within the i-layer**.

A TEM study of a series of solar cells versus SC demonstrated that most of the **microstructure changes occur in the first stages of the growth of the i-layer**. The nuclei density decreases and the thickness of the mixed phase (amorphous/microcrystalline) layer increases when SC is raised. Raman spectroscopy on the same samples revealed that changes also occur at the final stages of the growth of the i-layer, but they are not visible on the TEM micrographs. It is observed that **the higher is SC, the smaller is the nuclei density** and the larger is the amorphous fraction within the i-layer. **The increase of the nuclei density coincides with an increase of the V_{oc}.**

To improve the understanding of the formation of the microstructure, an innovative growth model based on two simple selection rules and three intuitive simulation parameters (i.e. critical size of nuclei, number of crystallographic orientations and desorption probability) was introduced. The selection rules are the following: a newly deposited particle tends to be in the same state as its neighbors and a particle incorporated in disordered material is preferentially removed. **The model is able to reproduce the main characteristics of the growth dynamics and microstructure of μc-Si:H:**

- **Conical shape of the grains**
- **Thickness transition from amorphous to crystalline material**

- **Amorphous to crystalline transition with respect to desorption probability**
- **Surface roughness evolution with respect to layer thickness**

This simple model gives the keys to understanding the growth dynamics and microstructure of µc-Si:H layers.

Electronic quality of i-layer and V_{oc}

The electronic quality of the i-layer within the active solar cells was investigated with the help of FTPS. This technique allows for the measurement of the absorption spectrum of the i-layer within the active device over several orders of magnitude.

To ensure that the FTPS signal for photon energies below the band-gap is truly related to the absorption by defects in the i-layer, defects were artificially created by proton irradiation. The samples were then thermally annealed with successive steps and measured by FTPS. It is shown that the **defect related absorption of the i-layer decreases as the annealing steps are performed**. FTPS therefore provides valuable information on the quality of the intrinsic layer within working solar cells.

In order to observe the influence of SC on the defect density, two series of cells deposited with different SC were deposited. The FTPS measurements demonstrate that **the defect related absorption of the i-layer decreases as SC is raised**.

Finally, **variation of the defect density either by stepwise annealing of a sample irradiated by a proton beam or by variation of SC of i-layer was shown to influence the V_{oc} significantly.**

From the above observations and conclusions one speculates that further tailoring of the structure of the solar cells could lead to a better open-circuit voltage for µc-Si:H solar cells.

References

1. S. Veprek and V. Marecek, *Solid State Communications* **11**, 683 (1968).
2. J. Meier, R. Fluckiger, H. Keppner, and A. Shah, *Applied Physics Letters* **65**, 860 (1994).
3. E. Vallat-Sauvain, U. Kroll, J. Meier, N. Wyrsch, and A. Shah, *Journal of Non-Crystalline Solids* **266-269**, 125 (2000).
4. M. Luysberg, C. Scholten, L. Houben, R. Carius, F. Finger, and O. Vetterl, *Material Research Society Symposium Proceedings* **664**, A15.2.1 (2001).
5. J. Dubail, E. Vallat-Sauvain, J. Meier, S. Dubail, and A. Shah, *Material Research Society Symposium Proceedings* **609**, A13.6.1 (2001).
6. J. Bailat, E. Vallat-Sauvain, L. Feitknecht, C. Droz, and A. Shah, *Journal of Applied Physics* **93**, 5727 (2003).
7. J. Meier, E. Vallat-Sauvain, S. Dubail, U. Kroll, J. Dubail, S. Golay, L. Feitknecht, P. Torres, S. Fay, D. Fischer, and A. Shah, *Solar Energy Materials and Solar Cells* **66**, 73 (2001).
8. P. Roca i Cabarrocas, N. Layadi, T. Heitz, B. Drévillon, and I. Solomon, *Applied Physics Letters* **66**, 3609 (1995).
9. S. Guha, J. Yang, D. L. Williamson, Y. Lubianiker, J. D. Cohen, and A. H. Mahan, *Applied Physics Letters* **74**, 1860 (1999).
10. Y. Nasuno, M. Kondo, and A. Matsuda, *Solar Energy Materials and Solar Cells* **74**, 497 (2002).
11. S. Klein, F. Finger, R. Carius, B. Rech, L. Houben, M. Luysberg, and M. Stutzmann, *Material Research Society Symposium Proceedings* **715**, A26.2.1 (2002).
12. L. Feitknecht, C. Droz, J. Bailat, X. Niquille, J. Guillet, and A. Shah, *Material Research Society Symposium Proceedings* **762**, 503 (2003).
13. A. Shah, H. Schaade, M. Vanecek, J. Meier, E. Vallat-Sauvain, N. Wyrsch, U. Kroll, C. Droz, and J. Bailat, *Progress in photovoltaics: Research and applications* **12**, 1 (2004).
14. A. Shah, J. Meier, E. Vallat-Sauvain, C. Droz, U. Kroll, N. Wyrsch, J. Guillet, and U. Graf, *Thin Solid Films* **403-404**, 179 (2002).
15. C. Droz, E. Vallat-Sauvain, J. Bailat, L. Feitknecht, J. Meier, and A. Shah, *Solar Energy Materials and Solar Cells* **81**, 61 (2004).

16. C. Droz, E. Vallat-Sauvain, J. Bailat, L. Feitknecht, J. Meier, X. Niquille, and A. Shah, *3rd World Conference on Photovoltaic Energy Conversion* (2003).
17. A. Poruba, M. Vanecek, J. Meier, and A. Shah, *Journal of Non-Crystalline Solids* **299-302**, 536 (2002).
18. M. Vanecek and A. Poruba, *Applied Physics Letters* **80**, 719 (2002).
19. S. Fay, Editor^Editors. 2003, EPFL: Lausanne.
20. S. Fay, S. Dubail, U. Kroll, J. Meier, Y. Ziegler, and A. Shah, *16th EU Photovoltaic solar energy conference* 361 (2000).
21. H. Curtins, N. Wyrsch, and A. Shah, *Electronic Letters* **23**, 228 (1987).
22. J. Meier, U. Kroll, E. Vallat-Sauvain, J. Spitznagel, U. Graf, and A. Shah, (2004).
23. A. C. Boccara, D. Fournier, and J. Bardoz, *Applied Physics Letters* **36**, 130 (1980).
24. N. Wyrsch, *Thesis* (1992).
25. M. Vanecek, J. Kocka, J. Stuchlik, and A. Triska, *Solid State Communications* **39**, 1199 (1981).
26. J. Benedict, R. Anderson, and S. J. Klepeis, *Material Research Society Symposium Proceedings* **254**, 121 (1992).
27. D. B. Williams and C. Barry Carter, *Transmission electron microscopy*. 1996, New-York: Plenum Press.
28. C. Droz, *Thesis, Université de Neuchâtel* (2004).
29. Y. Nasuno, M. Kondo, and A. Matsuda, *Material Research Society Symposium Proceedings* **664**, A15.5.7 (2001).
30. Joohyun Koh, A. S. Ferlauto, P. I. Rovira, C. R. Wronski, and R. W. Collins, *Applied Physics Letters* **75**, 2286 (1999).
31. A. Fejfar, T. Mates, C. Koch, B. Rezek, V. Svrcek, P. Fojtik, H. Stuchlikova, J. Stuchlik, and J. Kocka, *Material Research Society Symposium Proceedings* **664**, A16.1.1 (2001).
32. R. W. Collins, A. S. Ferlauto, G. M. Ferreira, C. Chen, Joohyun Koh, R. J. Koval, Yeeheng Lee, J. M. Pearce, and C. R. Wronski, *Solar Energy Materials and Solar Cells* **78**, 143 (2003).
33. Y. Z. Hu, C. Y. Zhao, C. Basa, W. X. Gao, and E. A. Irene, *Applied Physics Letters* **69**, 485 (1996).
34. S. Hasegawa, N. Uchida, S. Takenaka, T. Inokuma, and Y. Kurata, *Japanese Journal of Applied Physics* **37**, 4711
35. K. Mori, T. Yasuda, M. Nishizawa, S. Yamasaki, and K. Tanaka, *Japanese Journal of Applied Physics* **39**, 6647 (2000).

36. E. Vallat-Sauvain, U. Kroll, J. Meier, A. Shah, and J. Pohl, *Journal of Applied Physics* **87**, 3137 (2000).
37. O. Vetterl, F. Finger, R. Carius, P. Hapke, L. Houben, O. Kluth, A. Lambertz, A. Muck, B. Rech, and H. Wagner, *Solar Energy Materials and Solar Cells* **62**, 97 (2000).
38. H. Keppner, P. Torres, R. Fluckiger, J. Meier, A. Shah, C. Fortmann, P. Fath, G. Willeke, K. Happle, and H. Kiess, *Solar Energy Materials and Solar Cells* **34**, 201 (1994).
39. T. Mates, A. Fejfar, I. Drbohlav, B. Rezek, P. Fojtik, K. Luterova, J. Kocka, C. Koch, M. B. Schubert, and M. Ito, *Journal of Non-Crystalline Solids* **299-302**, 767 (2002).
40. J. Bailat, E. Vallat-Sauvain, A. Vallat, and A. Shah, *Journal of Non-Crystalline Solids* (2004).
41. A.-L. Barabasi and H. E. Stanley, *Fractal Concepts in Surface Growth*. 1995, Cambridge: Cambridge University Press.
42. T. Smy, S. K. Dew, and R. V. Joshi, *Thin Solid Films* **415**, 32 (2002).
43. C. C. Tsai, *Amorphous silicon and related materials*, W. Scientific, Editor. 1988.
44. A. Matsuda, *Thin Solid Films* **337**, 1 (1999).
45. J. D. Cody, *Journal of Non-Crystalline Solids* **141**, 3 (1992).
46. P. R. Griffiths and J. A. deHaseth, *Fourier Transform Infrared Spectroscopy*. 1986, New-York: Wiley.
47. J. Kündig, *Thesis, Université de Neuchâtel* (2003).
48. M. Vanecek, A. Poruba, Z. Remes, J. Rosa, S. Kamba, V. Vorlicek, J. Meier, and A. Shah, *Journal of Non-Crystalline Solids* **266-269**, 519 (2000).
49. A. L. Baia Neto, A. Lambertz, R. Carius, and F. Finger, *Journal of Non-Crystalline Solids* **299-302**, 274 (2002).
50. J. Bailat, E. Vallat-Sauvain, L. Feitknecht, C. Droz, and A. Shah, *Journal of Non-Crystalline Solids* **299-302**, 1219 (2002).
51. H. J. Hovel, *Solar Cells*. Semiconductors and Semimetals, ed. R.K. Williardson and A.C. Beer. Vol. 11. 1975, New York: Academic Press.

Acknowledgements

I would like to thank Prof. A. Shah for giving me the opportunity to work in his high-level and enthusiastic research group in thin film silicon and for allowing me to realize this thesis work in the field of photovoltaics.

I appreciated greatly the acceptance of the referees to join the examination board and to devote time to critically reading and correcting this thesis.

A special thanks goes to my project leader Dr. E. Vallat for her availability, open-mindedness and wise advices throughout the years spent in the thin film silicon group. I also owe much to her husband Dr. A. Vallat, my mentor for numerical growth simulations.

A warm thanks goes to Dr. M. Vanecek who welcomed me for three months in his research group at the Czech Academy of Science and to whom I owe all I know on absorption measurements. A very friendly 'díky' goes to A. Poruba who introduced me to FTPS technique and to all the colleagues and friends from Cukrovarnicka. Together, further absorption experiments were done 'ex-situ', downtown Prague, the results of which could not, for obvious reasons, be published here.

I would like to acknowledge Dr. M. Dadras for helping me with the TEM observations and M. Leboeuf who patiently thought me the delicate art of sample preparation for TEM.

Science is fun, however, the years spent in the silicon group would have been much less fun without all the colleagues and friends from the IMT in Neuchâtel. I would like to thank all of them for the fruitful collaboration and discussions, which contributed much to the present work. In particular I wish to thank X. Niquille who always accepted to deposit 'sur mesure' μc-Si:H layers and solar cells. I also acknowledge L. Feitknecht, J. Meier, U. Kroll N. Wyrsch, and M. Dubey for further sample preparation and stimulating discussions on technology and characterization. I also wish to thank F. Meillaud and C. Droz who did much of the Raman spectroscopy presented here.

Finally, I would like to thank my family for its enthusiasm and constant support.